ABSTRACT

PROPERTIES AND DEVICE APPLICATIONS OF SILICON AND SILICON-GERMANIUM NANOSTRUCTURES WITH DIFFERENT DIMENSIONS

by
Han-Yun Chang

Defect-free crystalline Si/SiGe(Ge) nanostructures are demonstrated despite the 4% lattice mismatch between Si and Ge. The lattice mismatch-induced strain is sufficiently relaxed through the designed, cluster morphology, or nanowire (NW) structures. Future device applications of these nanostructures require complete understanding of their structural, optical, electrical and thermal properties. This study explores these properties in two-dimensional (2D) Si/Si:B delta-doped multilayers, 2D $Si/Si_{1-x}Ge_x$ planar multilayers, three-dimensional (3D) $Si/Si_{1-x}Ge_x$ cluster multilayers, one-dimensional (1D) Si NWs and 1D Si/Ge NW heterojunctions (HJs).

Raman scattering and photoluminescence measurements show that by alternating heavily boron-doped layers with layers of undoped Si in Si/Si:B multilayers, dopant segregation and strain can be avoided. Current-voltage and capacitance-voltage measurements show Schottky-barrier-like characteristics in these nanostructures. The studied samples exhibit significant dependence of optical reflection on temperature and applied electric field, and hence have a potential to be used as electrically controllable mirrors.

High Ge content 2D (planar) and 3D (cluster) Si/SiGe multilayers are studied thoroughly using Raman spectroscopy. Low frequency Raman measurements show formation of strong folded longitudinal acoustic (FLA) phonons in the 2D sample,

indicating abrupt interfaces and good superlattice structure. By utilizing the multi-modal feature of Raman scattering, local temperatures are found by comparing the intensities of Stokes and anti-Stokes signals at specific wavenumbers, and the thermal conductivity of each sample is estimated. A strong correlation between FLA and thermal conductivity is found: in samples with high intensity FLA, thermal conductivity is almost twice increases, when compare to samples without FLA.

Fabrications of Si NWs and Si/Ge NW HJs are explored, including interference-lithography-based photoresist patterning for Au catalysts. Raman spectroscopy shows significant strain in Si NWs and Si/Ge NW HJs. In the HJs, the temperature dependence in PL peak positions suggested a preferential composition at the hetero-junction. Raman-spectroscopy-based temperature measurements show significant decrease in the thermal conductivity of NW HJs: more than one order of magnitude less than that in Si NWs and two orders of magnitude less than that in c-Si. The high mobility and good carrier transport, combined with the substantially decreased thermal conductivity gives these Si/Ge and Si/SiGe nanostructures great potential in CMOS compatible, integrated thermoelectric device applications.

PROPERTIES AND DEVICE APPLICATIONS OF SILICON AND SILICON-GERMANIUM NANOSTRUCTURES WITH DIFFERENT DIMENSIONS

Han-Yun Chang

A Dissertation
Submitted to the Faculty of
New Jersey Institute of Technology
in Partial Fulfillment of the Requirements for the Degree of
Doctor of Philosophy in Electrical Engineering

Department of Electrical and Computer Engineering

May 2010

APPROVAL PAGE

PROPERTIES AND DEVICE APPLICATIONS OF SILICON AND SILICON-GERMANIUM NANOSTRUCTURES WITH DIFFERENT DIMENSIONS

Han-Yun Chang

Dr. Leonid Tsybeskov, Dissertation Advisor Professor of Electrical and Computer Engineering, NJIT	Date
Dr. Haim Grebel, Committee Member Professor of Electrical and Computer Engineering, NJIT	Date
Dr. Lev N. Krasnoperov, Committee Member Professor of Chemistry and Environmental Science, NJIT	Date
Dr. Andrei Sirenko, Committee Member Associate Professor of Physics, NJIT	Date
Dr. Marek Sosnowski, Committee Member Professor of Electrical and Computer Engineering, NJIT	Date

BIOGRAPHICAL SKETCH

Author: Han-Yun Chang

Degree: Doctor of Philosophy

Date: May 2010

Undergraduate and Graduate Education:

- Doctor of Philosophy in Electrical Engineering,
  New Jersey Institute of Technology, Newark, NJ, 2010
- Master of Science in Electrical Engineering,
  Columbia University, New York, NY, 2004
- Bachelor of Science in Electrical Engineering,
  New Jersey Institute of Technology, Newark, NJ, 2002

Major: Electrical Engineering

Presentations and Publications:

- Book Chapter

H.-Y. Chang and L. Tsybeskov, "Thermal Properties and Heat Transport in Silicon Based Nanostructures" in "*Silicon Nanocrystals – Fundamentals, Synthesis and Applications*." L. Pavesi and R. Turan, Eds. Weinheim: Wiley-VCH Verlag GmbH & Co. KGaA, pp. 105-154, 2010.

- Journal Publications

H.-Y. Chang, L. Tsybeskov, S. Sharma, T. I. Kamins, X. Wu, and D. J. Lockwood, "Photoluminescence and Raman Scattering in Axial Si/Ge Nanowire Heterojunctions," Applied Physics Letters, vol. 95, art. no.: 133120, 2009.

L. Tsybeskov, E.-K. Lee, H.-Y. Chang, D. J. Lockwood, J.-M. Baribeau, X. Wu, and T. I. Kamins, "Silicon-Germanium Nanostructures for on-Chip Optical Interconnects," Applied Physics A, vol. 95, pp. 1015-1027, 2009.

L. Tsybeskov, E.-K. Lee, H.-Y. Chang, B. V. Kamenev, D. J. Lockwood, J.-M. Baribeau, and T. I. Kamins, "Three-Dimensional Silicon-Germanium Nanostructures for CMOS Compatible Light Emitters and Optical Interconnects," Advances in Optical Technologies, vol. 2008, art. no. 218032, 2008.

B. V. Kamenev, E.-K. Lee, H.-Y. Chang, H. Han, H. Grebel, L. Tsybeskov, and T. I. Kamins, "Excitation-Dependent Photoluminescence in GeSi Stranski-Krastanov Nanostructures," Applied Physics Letters, vol. 89, 153106, 2006.

- Conference Proceedings Publications

H.-Y. Chang, L. Tsybeskov, A. Sirenko, D. J. Lockwood, J.-M. Baribeau, X. Wu and M. W. C. Dharma-Wardana, "Thermal Conductivity of Three-dimensional Si/SiGe Nanostructures," Material Research Society Symposium Proceedings, vol. 1145, 1145-MM12-01, 2009.

H.-Y. Chang, E.-K. Lee, B. V. Kamenev, J.-M. Baribeau, D. J. Lockwood and L. Tsybeskov, "Optical Properties of Multiple, Delta-doped Si:B/Si Layers", Material Research Society Symposium Proceedings, vol. 958, p. 0958-L10-23, 2007.

- Conference Oral Presentations

H.-Y. Chang, L. Tsybeskov, A. Sirenko, D. J. Lockwood, J.-M. Baribeau, X. Wu, M. W. C. Dharma-Wardana, T. I. Kamins and A. M. Bratkovsky, "Thermal Conductivity of Silicon/Germanium Nanostructures," American Physical Society March Meeting, Pittsburgh, PA, March 2009.

H.-Y. Chang, L. Tsybeskov, A. Sirenko, D. J. Lockwood, J.-M. Baribeau, X. Wu and M. W. C. Dharma-Wardana, "Thermal Conductivity of Three-dimensional Si/SiGe Nanostructures," Material Research Society Meeting, Boston, MA, December 2008.

- Conference Poster Presentations

H.-Y. Chang, L. Tsybeskov, A. Sirenko, D. J. Lockwood, J.-M. Baribeau, X. Wu, and M.W. C. Dharma-Wardana, "Raman Scattering and Thermal Conductivity in Si/SiGe Nanostructures", The Dana Knox Student Research Showcase, New Jersey Institute of Technology, Newark, NJ, April 2010.

H.-Y. Chang, E.-K. Lee, B. V. Kamenev, J.-M. Baribeau, D. J. Lockwood and L. Tsybeskov, "Optical Properties of Multiple, Delta-doped Si:B/Si Layers", NJIT Provost's Student Research Showcase, Newark, NJ, February 2007.

H.-Y. Chang, E.-K. Lee, B. V. Kamenev, J.-M. Baribeau, D. J. Lockwood and L. Tsybeskov, "Optical Properties of Multiple, Delta-doped Si:B/Si Layers", Material Research Society Meeting, Boston, MA, December 2006.

- Papers in Progress

H.-Y. Chang, L. Tsybeskov, J.-M. Baribeau and D. J. Lockwood, "Optical Properties of Multiple, Delta-doped Si:B/Si Nano-layers" (prepared for submission to Journal of Applied Physics).

H.-Y. Chang, L. Tsybeskov, J.-M. Baribeau and D. J. Lockwood, "Thermal Conductance in Si/SiGe Multi-layered Clusters" (prepared for submission to Nanotechnology).

To my family

ACKNOWLEDGEMENT

First and foremost, I would like to express my deepest gratitude for my thesis advisor, Dr. Leonid Tsybeskov, for the guidance, inspiration, and support throughout this research project and thesis.

I would also like to thank Dr. Haim Grebel, Dr. Marek Sosnowski, Dr. Andrei Sirenko and Dr. Lev Krasnoperov for serving as members of my committee.

My thanks also go to Dr. Ted Kamins and Dr. David Lockwood for providing the samples and many valuable feedbacks throughout this research.

TABLE OF CONTENTS

TABLE OF CONTENTS
(Continued)

LIST OF TABLES

LIST OF FIGURES

LIST OF FIGURES
(Continued)

LIST OF FIGURES
(Continued)

LIST OF FIGURES
(Continued)

Figure **Page**

LIST OF FIGURES
(Continued)

Figure **Page**

LIST OF FIGURES
(Continued)

Figure **Page**

LIST OF FIGURES
(Continued)

Figure **Page**

CHAPTER 1

INTRODUCTION

For the last forty years, crystalline Si (c-Si) continues to be the major material for microelectronics, and modern silicon technology is superior compared to other semiconductors (e.g., II-VI and III-V compounds). In addition to the complementary metal-oxide-semiconductor (CMOS) technology, SiGe heterojunction bipolar transistors (HBTs), have become vital in Bi-CMOS and RF applications [1, 2]. Other promising applications for SiGe devices include CMOS-compatible light sources for optical communication and various system-on-a-chip components [1]. Beyond these applications, SiGe heterostructure also has potential for developing thermoelectric (TE) devices. The thermal conductivity of $Si_{1-x}Ge_x$ alloys and Si/SiGe nanostructures could be reduced by several orders of magnitude compared to that in c-Si. With the added benefit of controllable electrical conductivity, Si and Si/SiGe nanostructures are ideal for thermoelectric device applications.

The fabrication of Si/Ge heterojunction (HJ) has always been a challenging task. Abrupt Si/Ge HJs can not be constructed by conventional thin film technology because of the 4.2% larger lattice constant of c-Ge over c-Si. The critical thickness of c-Ge films grown on Si substrates is less than 2 nm, and films exceeding the critical thickness will have dislocations for strain relaxation [1, 2]. Common solutions to the strain relaxation problem are pseudomorphic heterostructures formed with with Si and SiGe alloy, such as graded Ge composition, $Si_{1-x}Ge_x$ alloy structures or symmetrically strained Si/Ge superlattices (SLs) [3-5]. This dissertation will introduce several novel approaches

to Si and Si/SiGe nanostructures beyond the aforementioned methods. These novel approaches to Si and Si/SiGe nanostructures, that are dislocation-free crystalline structure with sufficient strain relaxation, include Si:B delta-doped multilayer SLs, three-dimensional (3D) cluster morphology Si/SiGe multilayer SLs, two-dimensional (2D) planar $Si/Si_{1-x}Ge_x$ multilayer SLs, and one-dimensional (1D) Si/Ge nanowire (NW) HJs. Specifically, this study will focus on the structural, optical, thermal and electrical properties of these Si and Si/SiGe nanostructures with different dimensionalities and their possible device applications. The 3D cluster multilayers and the 2D planar multilayers are fabricated by using molecular beam epitaxy (MBE) with Stranski-Krastanov (S-K) and Frank-van der Merwe growth modes, respectively, while the 1D NW HJs are fabricated using chemical vapor deposition (CVD) and vapor-liquid-solid (VLS) growth. Chapter 2 presents a detaiedl review of the growth processes and description of the samples studies in this dissertation followed by physical properties of the nanostructures. Chapter 3 describes the characterization techniques, experimental set up and measurement procedures used, including a novel Raman-based nano-thermometry using specific vibration modes. The last part of Chapter 3 consists of characterization methods used at collaborating research facilities.

Detailed experimental results and extensive discussion will be given in Chapter 4. For the Si:B delta-doped samples, photoluminescence (PL) and Raman spectroscopy (RS) found no strain and B segregation from the high doping concentration; while the optical reflection measurement and current-voltage (I-V) measurements illustrate the nanostructures' possible application as electrically-controlled mirrors. In 3D (cluster morphology) and 2D (planar morphology) Si/SiGe multilayer SL samples, low-frequency

RS detects the formation of folded longitudinal acoustic (FLA) phonons in certain SLs, and the Raman-based thermometry reveal a correlation of higher thermal conductivity and the intensity of FLA phonons. As for the Si/Ge NW HJ sample, multi-peak, temperature and excitation dependent PL reveals preferential $Si_{1-x}Ge_x$ composition in the HJ, which is confirmed by energy-dispersive x-ray spectroscopy (EDX). The performed PL measurements also find additional strain, consisting with thermal expansion mismatch between Si and Ge. RS shows evidence of strain and Raman-based thermometry gives an accurate estimation of thermal conductivity. The found thermal properties with the addition of preliminary data on thermo-voltage support the possibility of Si/Ge NW applications as TE generators.

In Chapter 5, this dissertation ends with summary of the presented work and concluding remarks.

CHAPTER 2

BACKGROUND

2.1 Si/SiGe Nanostructure Fabrication

The most common deposition methods used to grow epitaxial Si and Si/SiGe nanostructures are molecular beam epitaxy (MBE) and chemical vapor deposition (CVD). All the samples studies in this dissertation are fabricated using one of these methods. Following is an overview of MBE and CVD, and detailed descriptions of specific sample fabrications are given in the subsections.

Solid source MBE usually takes place in ultra high vacuum, and fluxes or beams of atoms or molecules is generated from high purity depositing material by heating the element in effusion cells (Knudsen cells) or by electron beam. The growth rate is based on the fluxes of the source, which is controlled by shutters of the cells. This gives MBE its main advantage in Si/SiGe nanostructures: precise control over the layer thickness and Ge content of the nanostructure, that is subject only to source fluxes and is unaffected by the substrate temperature. The major drawback of using MBE in SiGe growth is the high melting points of Si and Ge produce the dilemma of a tradeoff between the lower deposition rate (using effusion cells) or an unwanted radiation and a higher risk of background contamination (using electron beam evaporators). Other MBE limitations include difficulty in introducing dopants and inhomogeneous beam fluxes causing a non-uniform deposition [1].

The CVD process is based on thermal decomposition of reactants such as silane (SiH_4) and germane (GeH_4). It can be done at atmospheric pressure and high temperature (900-1000 °C) for depositing Si on Si substrate. However, to prevent surface roughness and diffusion of Ge, Si/SiGe nanostructure growth is usually performed at a reduced pressure (10 Pa for ultra-high vacuum CVD and 10-100 Pa for low pressure CVD) and lower growth temperature (~550-650 °C). CVD has been an industry standard in commercial production for its great advantages of fast and uniformed deposition with easy incorporation of dopants as well as the ability for batch process. Major shortcoming of CVD is in the complexity of controlling the layer thickness and the Ge content, which depends on multiple growth conditions, such as substrate temperature, precursor gas flow rate and chamber pressure. Careful adjustments and calibrations are needed when developing new SiGe nanostructure fabrication procedures [1].

2.1.1 Si:B Delta-doped Multilayer Superlattices

Delta-doping provides a high concentration of dopants spatially distributed as two-dimensional (2D) layers with sharp and narrow doping profiles [6]. These structures can be used as prototypes and modeling systems for future nano-devices and devices for quantum computing [7]. In most cases, delta-doping is achieved by using MBE, which provides a well-defined doping profile in both the doping concentration and delta-doped layer thickness [8, 9]. Fabrication of Si delta-doped structures requires particular care in preventing problems such as dopant segregation on epitaxial Si surfaces and structural defects due to high embedded strain [10]. In this dissertation, comprehensive studies of structural and optical properties of MBE-grown Si/delta-doped Si:B multilayer nanostructures is presented in an attempt to engineer a system where high carrier

concentration is provided via multi-layers of heavily delta-doped Si:B, while nominally undoped Si spacers play the role of buffer layers. These Si buffer layers reduce the strain, prevent dopant segregation and improve the overall thermal conductivity of these nanostructures. Another motivation for this work is a previous report on luminescence intensity enhancement and weaker luminescence intensity temperature dependence in heavily B-doped Si samples and possible defect engineering leading to highly luminescent Si-based materials [11]. Possible application of these nanostructures in electrically controlled mirrors is explored.

2.1.2. Two- and Three-dimensional Si/SiGe Nanostructures

There are three major modes of semiconductor epitaxial growth, which are illustrated in Figure 2.1. When there is low strain and enough kinetic energy for the deposition material to diffuse, the adatoms first start to diffuse at the atomic steps and gradually fill the area in between, forming a 2D layer. This growth mode is know as Frank-van der Merwe mode and is the mechanism for growth Si thin films or low Ge content $Si_{1-x}Ge_x$ thin films on Si substrate. On the contrary, when growing Si on Ge substrate, the system is under tensile strain and can minimize its free energy by trading increased surface area for decreased interfacial area, a three-dimensional (3D) growth known as Volmer-Weber mode occur. Similar formation occurs when adatoms are more strongly bound to each other than to the substrate material, such as Au on c-Si. The last growth mode, Stranski-Krastanov (S-K) mode is a combination of 2D and 3D growth. The S-K growth mode occurs when there is significant compression strain (e.g., lattice-mismatch-induced strain from Ge or higher Ge content $Si_{1-x}Ge_x$ alloy on Si substrate), high kinetic energy adatoms and high substrate temperature. The growth, in general, starts with a spontaneous 2D $Si_{1-x}Ge_x$, < 1 nm thick

wetting layer where x varies, mainly due to uncontrollable SiGe interdiffusion. The strain build up in the wetting layer distorts the lattice in the deposited layer as will as the surface of the substrate, attempting to achieve local relaxation. With further influx of Ge and Si, the growth mode switches from 2D (layers) to 3D (clusters), and it release some of the lattice-mismatch-induced strain. The S-K mode preferentially relaxes the strain elastically as interfacial misfit dislocations (forming of clusters), rather than inelastically as formation and glide of lateral misfit dislocation [1, 12, 13].

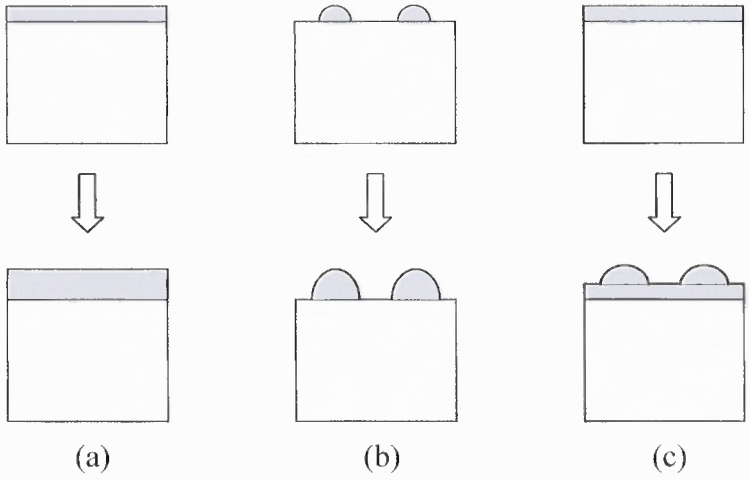

Figure 2.1 Three major modes of semiconductor epitaxial growth: (a) two-dimensional (2D) growth: Frank-van der Merwe mode, (b) three-dimensional (3D) growth: Volmer-Weber mode, and (c) a combination of 2D and 3D growth: Stranski-Krastanov mode.

Among these three major growth modes, S-K mode is the most common method of fabricating high-quality, CMOS-compatible, Si/Ge and Si/SiGe nanostructures. However, there are a few shortcomings of the S-K growth mode, the most important being the inhomogeneous cluster properties, such as $Si_{1-x}Ge_x$ composition, cluster size and shape, and the density of clusters. Figure 2.2 shows transmission electron microscopy (TEM) images of two different types of clusters: dome-shaped and pyramid-shaped [14].

The inhomogeneity of the clusters can be overcome by Si/SiGe multilayers SL structures grown at slightly lower temperatures [15]. In these nanostructures, layers of SiGe clusters are separated by Si layers within a critical thickness, where the strain fields of underlying clusters accumulate and progress through the separating layers and induce stacks of vertically aligned and laterally more homogeneous clusters in upper layers [16, 17].

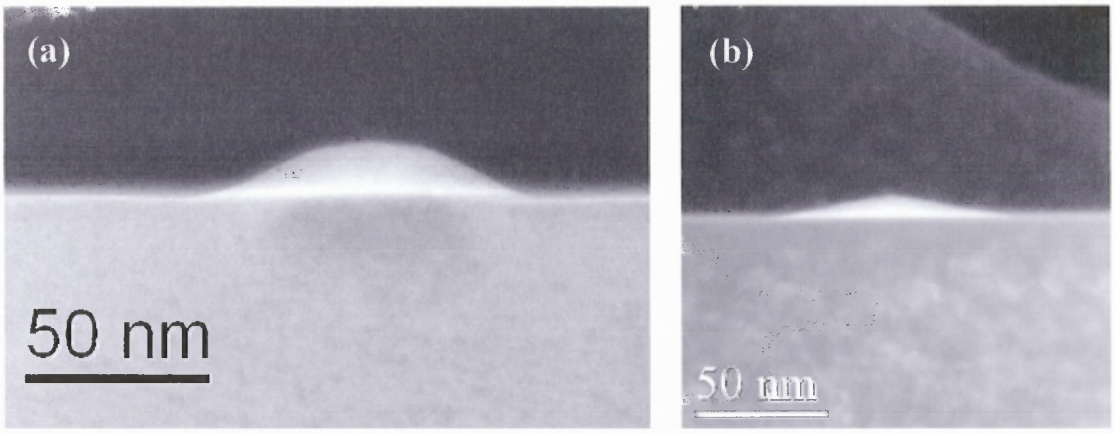

Figure 2.2 Transmission electron microscope (TEM) images of Ge cluster on Si (001) substrate with different cluster shapes: (a) dome-shaped and (b) pyramid-shaped [14].

The standard fabrication of 3D Si/SiGe multilayer nanostructures is based on the sequential physical sputtering of Si and Ge (or SiGe) in MBE or the thermal decomposition of SiH_4 and GeH_4 in CVD at temperatures ~550-650 °C. Figure 2.3 shows examples of MBE and CVD grown Si/SiGe clusters-morphology multilayer SLs [14]. The MBE sample clearly has better layer thickness control and stronger degree of self-alignment. Si/SiGe multilayer SL samples studied in this dissertation are fabricated using MBE and have 2D (planar) and 3D (cluster) morphology SiGe layers with high nominal Ge content, separated by Si layers. More details of sample description can be found in subsection 2.1.4.

It has been proposed that such Si/SiGe nanostructures, such as superlattices (SLs) with an enhanced carrier transport and an even lower thermal conductivity due to the nanometer-thick layers can have novel applications in efficient thermoelectric devices [18-21].

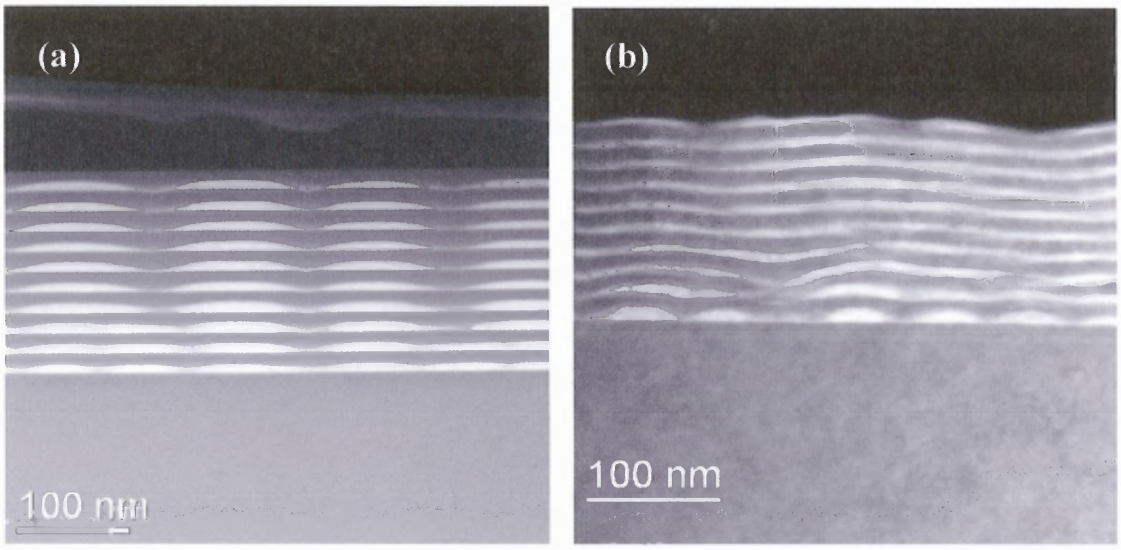

Figure 2.3 TEM images of $Si/Si_{1-x}Ge_x$ cluster multilayers grown in (a) MBE (x=0.46, grown at 625 ◦C) and (b) CVD (x=0.6, grown at 525 ◦C) [14].

2.1.3 Si/SiGe 1D Nanostructure: Vapor-Liquid-Solid Growth

The synthesis methods widely used in fabricating one-dimensional (1D) nanostructures, such as nanowires (NWs), nanotubes, and nanorods can be categorized by two major approaches: solution-based or vapor-based growth. An extensive review of nanowires synthesizing methods as well as a survey of properties of nanowires categorized by their materials can be found in Ref [22]. This subsection will focus on a vapor-based growth mechanism, by which the 1D nanostructures discussed in this dissertation is synthesized: vapor-liquid-solid (VLS) growth using CVD. The VLS growth of Si whiskers with Au catalyst was first proposed in 1964 by Wagner and Ellis with successful demonstration of sub-micron 1D structures [23]. The growth mechanism requires a metal catalyst which acts

as a nucleation site such that the size and location of the catalyst determines the size and location of the nanostructures. Although Au remains the most commonly used catalyst for Si NWs, many other metals (e.g., Ag, Ti, Ni, Fe, Ga and Al) have been used.

The process of growing Au-catalized Si and Si/Ge NW heterojunctions (HJs) on Si substrate starts with acquiring and distributing the Au particles in desired sizes by one of these commonly used approaches. The first approach is using pre-synthesized Au nanoparticles, often stored in liquid solutions. The particles are distributed on to the substrate by spin-coating. The second approach is by depositing an ultra-thin Au layer on the substrate, followed by annealing at temperature significantly lower than the Au-Si eutectic point. The atomic force interaction between Au atoms is much stronger than the interaction between Au and Si atoms. As a result, Au atoms form small droplets on the Si surface after deposition, and the annealing process provides the energy needed form larger droplets. Figure 2.4 shows a scanning electron microscope (SEM) image of <100 nm diameter Au clusters formed from sputtering 100 Å Au on Si and annealing at 200 °C for 20 minutes. The last approach is photoresist-based patterning of Au films. Besides the conventional photomask lithography or electron beam (e-beam) lithography, interference lithography (IL) is an excellent way to pattern Au catalyst for VLS growth, generating nano-scaled, mask-free and contact-free patterns with parallel processing ability.

When two coherent light beams interfere, they form a standing wave with period [24, 25]

$$d = \frac{\lambda}{2\sin\theta}, \tag{2.1}$$

where λ is the wavelength of the light and θ is the half angle between the two interfering

beams. By recording the interfered patterns in photoresist, a 1D grating can be produced. A schematic representation of the two-beam IL system is shown in Figure 2.5. As an endeavor in building patterned NWs and NW HJs in-house, an experimental setup for IL is assembled with a HeCd laser (λ =325nm). The laser beam is directed through a polarizer to ensure linear polarization. A short focal-length (~14 mm) lens is used to expand the beam pass the focal point. Mirrors are place to reflect the light and to form the standing wave pattern onto 4-inch test wafers, which is coated with photoresist. Both positive and negative photoresist are tested. The exposure doses are experimentally optimized for different types and thicknesses of the photoresist. After developing the photoresist, the wafers are inspected using SEM to determine the quality and dimension of the recorded patterns.

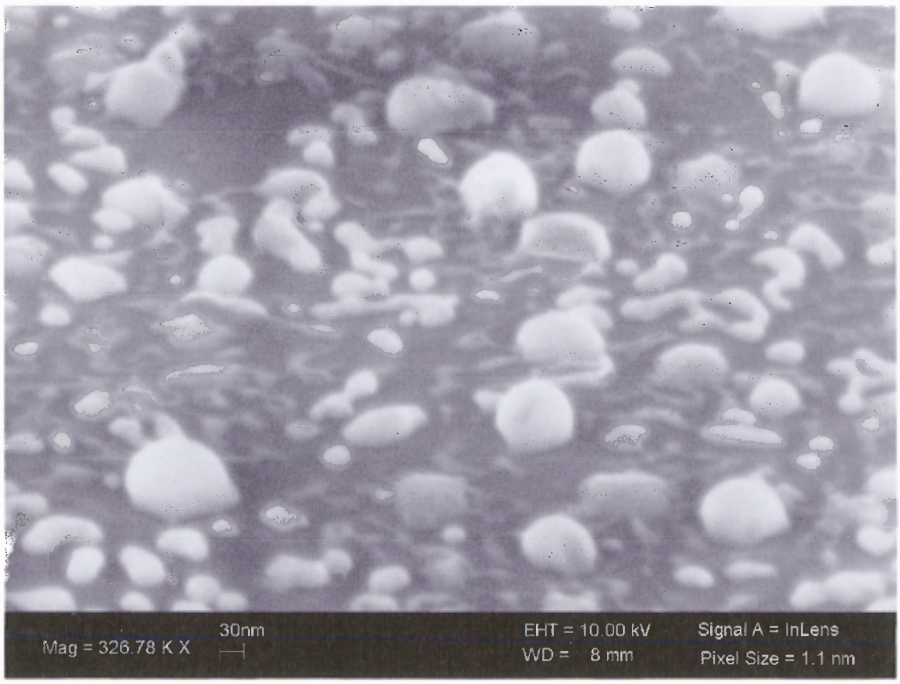

Figure 2.4 Scanning electron microscope (SEM) images of Au clusters formed from sputtering 100 Å Au on Si and annealing at 200 °C for 20 minutes.

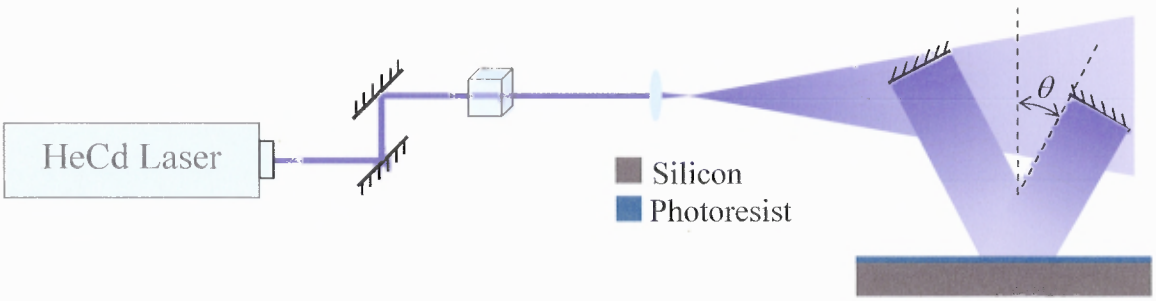

Figure 2.5 Schematics of the basic two-beam interference lithography setup.

In order to create the Au nano-cluster catalysts needed for VSL growth, 2D arrays are needed. Such arrays of dots (positive photoresist) or holes (negative photoresist) can be created with two-beam interference by double exposure, wherein the wafer is turned 90° between exposures. However, double exposure creates potential variables and complexity to the process, e.g. maintain the exact turn angle, which makes it difficult to incorporate the technique into a scan-and-step process [26]. Multi-beam interference is chosen as a solution to simplify the process and to produce a 2D pattern with single exposure [26-30]. Figure 2.6 lists SEM images patterns created on positive photoresist by single and double exposures of two-beam interference, and single exposure of three-beam and four-beam interference.

The last steps in creating patterned catalysts are depositing Au, forming Au-Si alloy by heating the wafer above the eutectic temperature (preferably in a vacuum environment to prevent Si oxidation), and after the wafer is properly cooled, removing the photoresist. Note that although the openings patterned by multi-beam IL are much larger than desired Au nanoparticle size, smaller dimensions can be obtained with thin layers of Au followed by proper annealing. The aforementioned Au cluster formation effect can take place and produce Au nanoparticles with diameters <100 nm for NW growth.

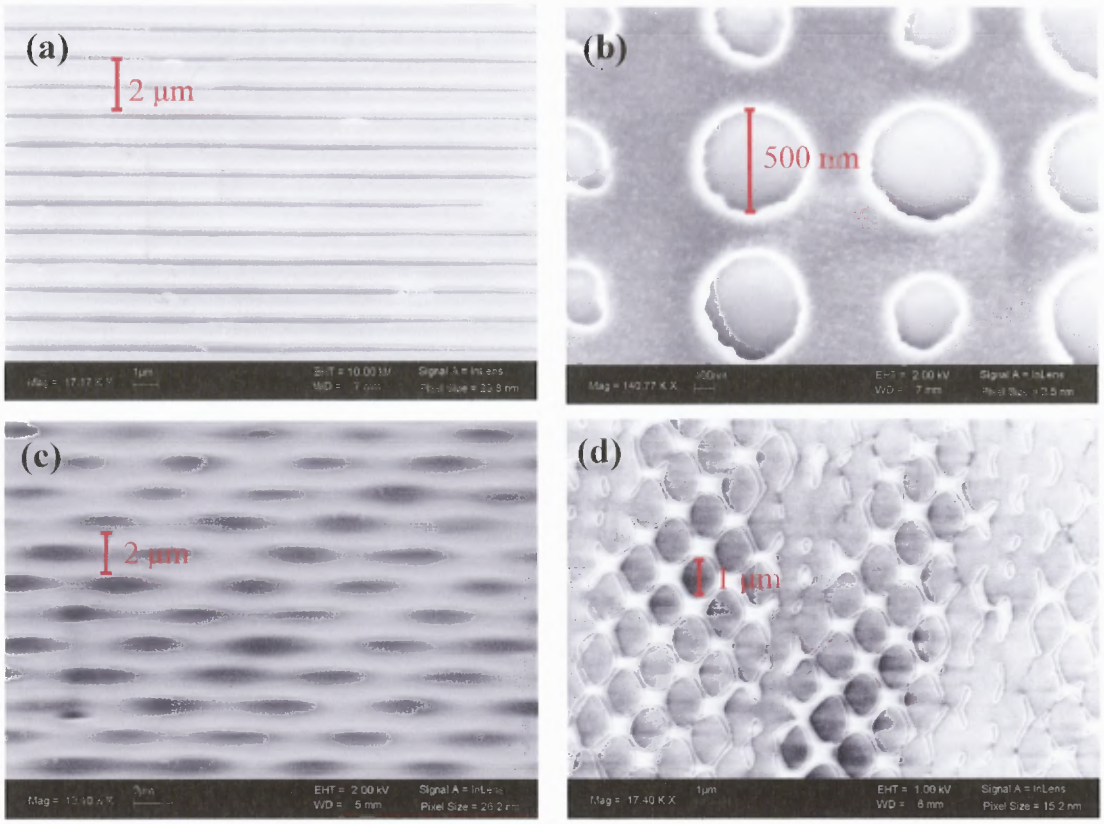

Figure 2.6 SEM images of positive photoresist exposed by multi-beam interference: (a) two-beam with single exposure, (b) two-beam with double exposure, (c) three-beam and (d) four-beam.

The VLS growth is done at temperatures equal to or higher than the eutectic point of the catalyst and the growth material. In Au-catalyzed Si growth, after reaching eutectic temperature, the Au nanoparticles form Au-Si alloy droplets with the substrate (Figure 2.7). Additional Si atoms are introduced into the system due to thermal decomposition of silane (SiH_4). The reactions can be express as follows:

$$SiH_4(g) \xrightarrow{\Delta} Si(g) + 2H_2(g). \tag{2.2}$$

These Si atoms will go through three phases, vapor, liquid and solid, as indicated in Au-Si phase diagram in Figure 2.8 [31], following the horizontal line at a set growth temperature,

from left to right. The gas (or vapor) phase Si atoms preferably diffuses into the Au-Si alloy droplets (Figure 2.7 (ii)) and become part of the alloy (Figure 2.8 (I)) as Si atoms undergo phase transition from vapor to liquid. After reaching saturation at growth temperature, Si atoms start to nucleate at the alloy/solid interfaces (Figure 2.7 (iii) and Figure 2.8 (II)) and Si atoms undergo phase transition from liquid to solid. As the wires grow, the alloy droplets remain on the top (Figure 2.7 (iv) and Figure 2.8 (III)) and continue to transform Si atoms through the three phases. To grow Si/Ge NW HJs, after reaching desired Si segment length, precursor gas is changed from SiH_4 to germane (GeH_4) and Ge atoms undergo the same thermal decomposition and VLS phase transitions (Figure 2.7 (v)). It is believed that the 4.2% lattice mismatch between Si and Ge can be partially relaxed at the HJ by means of expanded the diameter of the Ge segment, as illustrated in Figure 2.9.

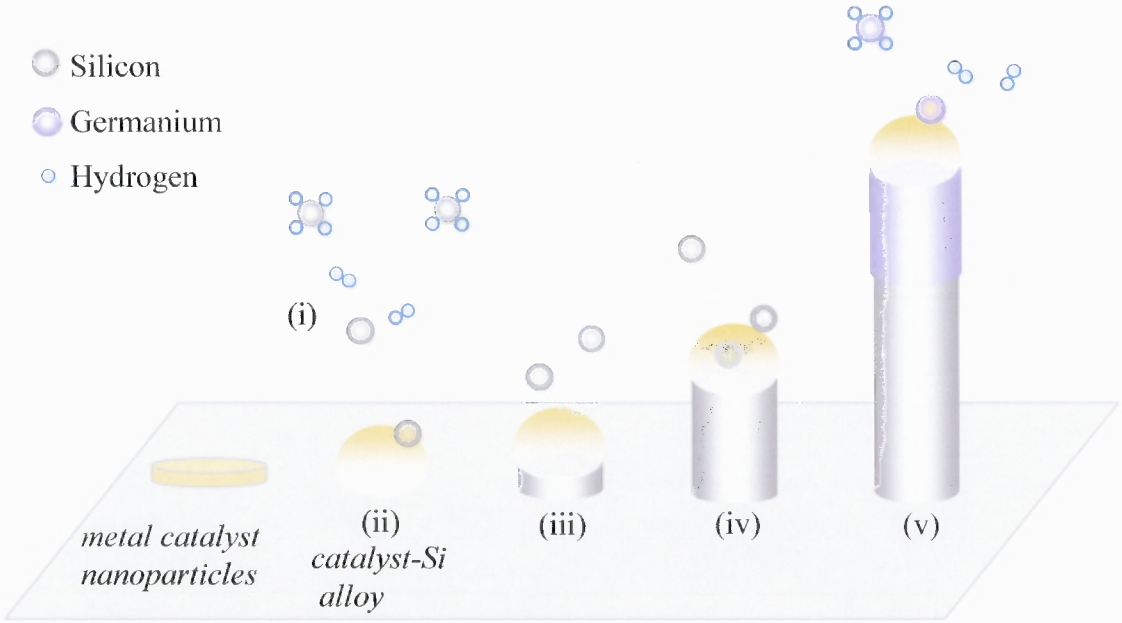

Figure 2.7 Step-by-step schematics of vapor-liquid-solid growth of Si nanowire and Si/Ge nanowire heterojunctions: (i) thermal decomposition of SiH_4, (ii) Si(g) diffuses into the Au-Si alloy droplet, (iii) nucleation of Si at the alloy/solid interface, (iv) growth of the Si nanowire, and (v) growth of the Ge segment of a Si/Ge heterojunction.

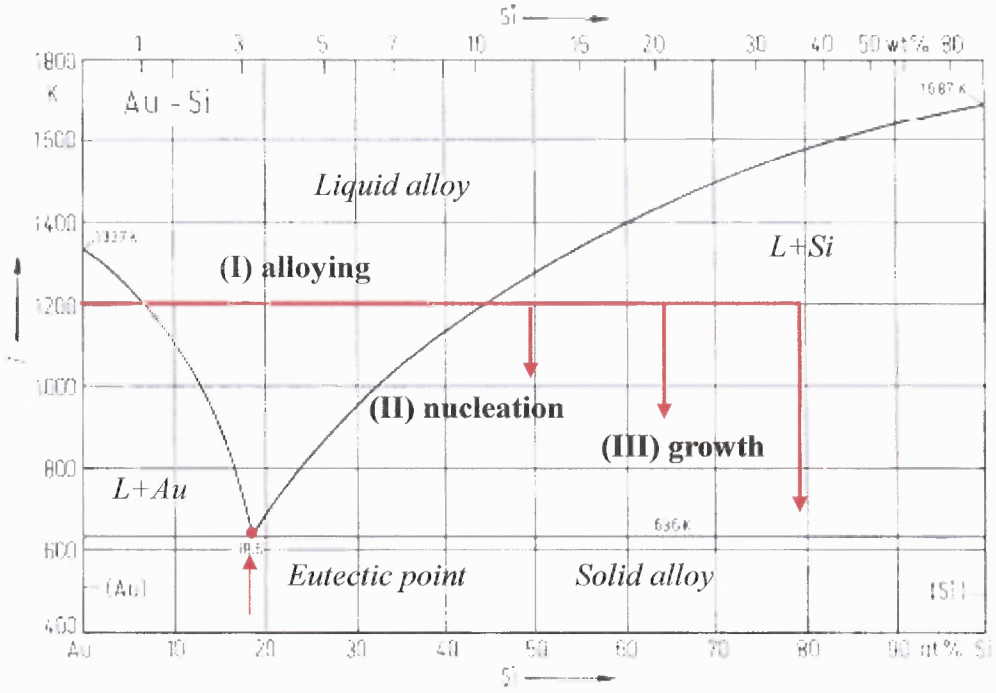

Figure 2.8 Phase diagram of the Au-Si alloy: (I) alloying (liquid Au-Si alloy phase) (II) nucleation (liquid Au-Si alloy and solid Si phase) and (III) growth (liquid Au-Si alloy and solid Si phase). Note that the eutectic point for Au-Si is at 636 K (363 °C) and 18.5% Au [31].

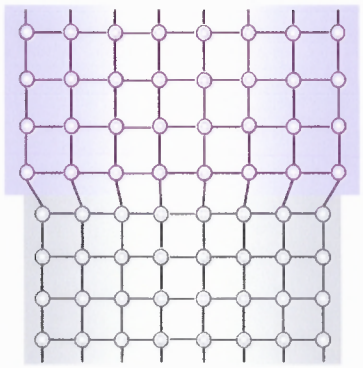

Figure 2.9 Schematic of the Si/Ge nanowire (NW) heterojunction (HJ) with the lattice-mismatch-induced strain relaxed around the HJ through expanded diameter of the Ge segment.

2.1.4 Samples Fabrication

The studied epitaxial Si/Si:B delta-doped multilayers were prepared by the Institute for Microstructural Sciences of National Research Council (NRC), Canada. The samples were fabricated in a VG V80 MBE system equipped with electron beam evaporators for Si and Ge. The wafer preparation consisted of a 600 s ultra-violet light exposure (UV ozone reactor) to photo-chemically remove surface hydrocarbon contamination. The wafers were then immediately introduced in the UHV apparatus and the surface native oxide was desorbed by annealing at about 900 °C for 600 s. The epitaxial Si was deposited at a rate of 0.1 nm/s at a substrate temperature of 640 +/- 25 °C, as measured by infrared pyrometry. Boron doping was achieved using a high temperature Knudsen effusion cell filled with elemental boron.

The 2D and 3D Si/SiGe multilayer samples were also prepared in NRC, Canada, using the MBE system described above. These multilayers are grown on Si (100) wafers and consist of 10 periods of alternating Ge-rich $Si_{1-x}Ge_x$ layers with separated by layers of Si. The growth temperature of the 2D multilayer sample was set at ~550 °C to maintain the planar morphology. The 3D multilayer samples were grown at much higher temperature of ~650 °C for S-K growth mode.

The metal-catalyzed Si NWs and Si/Ge NW HJs were prepared by Hewlett-Packard Laboratories (HP Labs). The Si NWs were grown by depositing Au and Ti on a Si (100) wafer. The wafers were then annealed at 900 °C in H_2 for 5 min to form Ti-Si or Au-Si alloy droplets. To grow Si NWs, the samples were exposed to a mixture of SiH_4, HCl, and H_2 at ~650 °C for ~30 min.

The Si/Ge NW HJ samples were grown using the VLS technique, Au catalysts, and the thermal decomposition of SiH_4 and GeH_4. The NW HJs were grown in a reduced-pressure, lamp-heated, CVD reactor. The substrate was p-type Si (111) with a resistivity of 0.01–0.02 Ω-cm. A thin layer of Au was deposited on the cleaned Si substrate and annealed in the CVD reactor for 10 min at 670 °C at 95 Torr in a H_2 ambient. The Si segments of the NWs were grown at 680 °C at 30 Torr using the gaseous precursors SiH_4 and HCl in a H_2 ambient. The sample was cooled to 350 °C at a nominal rate of 75 °C/min with the SiH_4–HCl–H_2 mixture flowing. The Ge segments of the NWs were then grown at 350 °C and 90 Torr, using GeH_4 and HCl as the gaseous precursors in the H_2 ambient.

2.2 Characteristics and Properties of Si and Si/SiGe Nanostructures

2.2.1 Structural Properties

In nano-scale Si and SiGe devices, the structural properties greatly affect the other characteristics. The most common structural characterizations are SEM and TEM with the addition of TEM-related techniques such as high-resolution TEM (HR-TEM) and energy-dispersive x-ray spectroscopy (EDX). These microscopy methods provide images of the nanostructure as well as qualitative analysis (e.g., dislocation, growth mode, crystalline orientation) and quantitative analysis (e.g., sizes and SiGe compositions).

The epitaxially grown Si:B delta-doped multilayers have structural properties nearly identical to bulk crystalline Si (c-Si), except for the possible dopant segregation at the heterointerfaces and structural defects from the high embedded strain, both due to the high doping concentrations. However, these characteristics can not be detected using microscopy because even with the highest doping concentration, only < 0.1% of the Si

atoms is replaced by dopants (B), which has similar atomic sizes. Thus, the structural properties of delta-doped multilayers (e.g., existence of dopant segregation or defects) are often extracted using SIMS, Auger electron spectroscopy and optical characterization.

In Si/SiGe multilayers, although MBE growth provides better control over the average SiGe layer composition, because of interdiffusion during growth, the layer composition is not uniform. Particularly, in the 3D multilayers, the clusters have ununiformed Ge composition within the cluster volume [32-34]. The fully grown, 3-10 nm high and initially near-pyramid-shaped SiGe clusters have a Ge-rich core (~50%, depending on the Ge flux), although the exact final cluster shape and composition strongly depends on the fabrication conditions (Figure 2.2). Detailed structural analysis also indicates that the Si matrix in the valleys between SiGe clusters is slightly compressed. To summarize, the buried SiGe clusters consists of $Si_{1-x}Ge_x$ crystalline alloys with x increasing toward the cluster center and reaching near 50% in the center; the clusters are surrounded by Si, which is tensile-strained above each SiGe cluster and compressed laterally between the clusters to maintain a low overall strain [32-34].

Unlike the 2D and 3D thin-film-based nanostructures, NWs do not follow the crystalline orientation of the substrate. The surface and edge tension during the liquid-solid phase of the VLS growth process results in preferential growth directions that is dependent of NW or catalyst nanoparticle sizes [35, 36]; NWs with diameters >40 nm are presumed to have preferential growth in the (111) direction. There are several possible structural defects; for instance, potential unwanted un-catalyzed NWs, worm-like amorphous NWs and kinks and bends. Figure 2.10 shows examples of the amorphous and bent NWs, prepared by plasma enhanced CVD and Au catalysts [37].

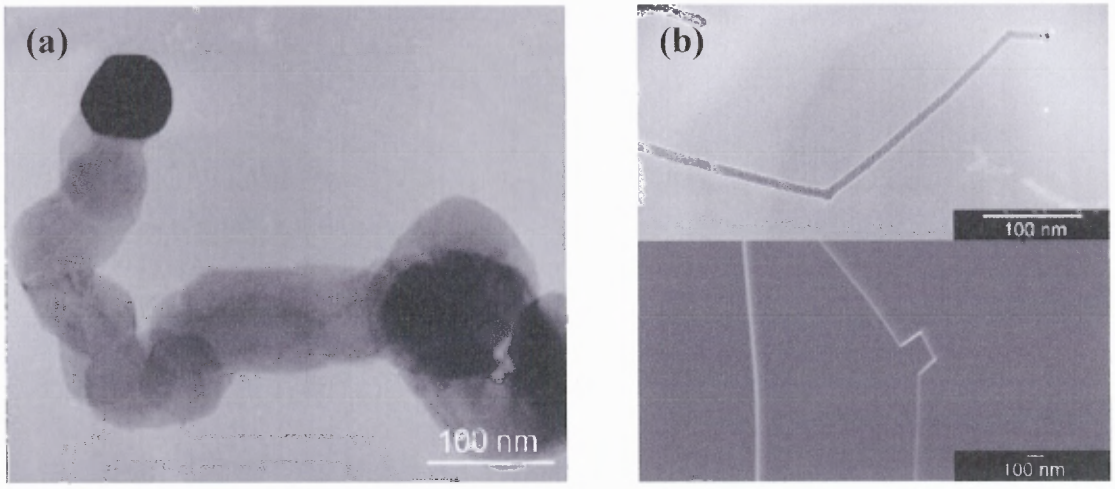

Figure 2.10 Defects in NWs: (a) high-resolution TEM (HR-TEM) image of a worm-like amorphous NW; (b) SEM and TEM images of NWs with kinks and bends [37].

2.2.2 Si/SiGe Heterojunction Energy Band Alignment

The electrical properties of the Si/SiGe and Si/Ge HJs are determined by the energy band alignment at the heterointerface. The discontinuity in the Si/Ge HJ energy bands with bulk, intrinsic materials can be calculated by the Anderson's affinity rule [38], and the ideal band alignment for an intrinsic Si/Ge HJ is as shown in Figure 2.11 with the electron affinities and room temperature bandgaps of Si and Ge as noted [39] and the offset in conduction bands and valence bands marked as ΔE_C and ΔE_V, respectively. This ideal type-I HJ band alignment applies if and only if the energy band properties (e.g., electron affinity and bandgap) of the material remains absolute and unaffected by the structure or surface properties (i.e., bulk Si and Ge with no strain).

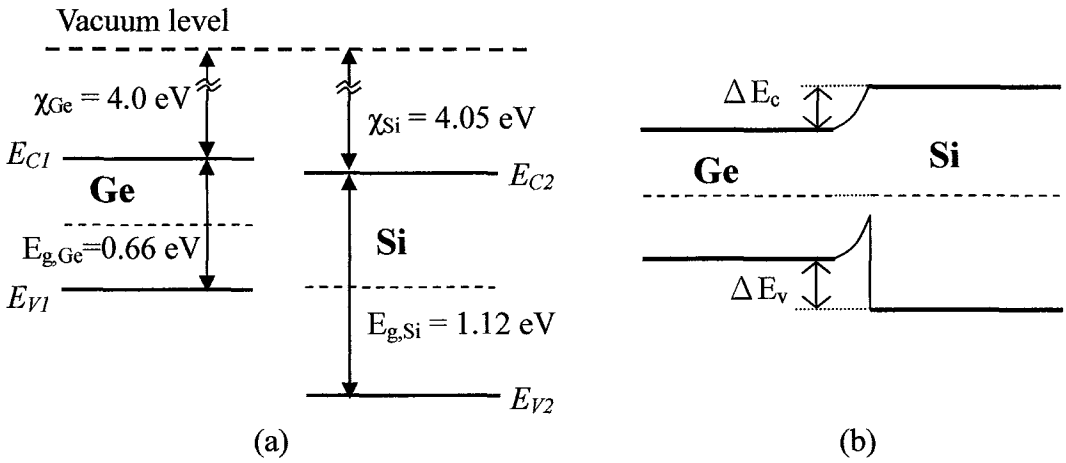

Figure 2.11 Energy band diagrams of (a) bulk, intrinsic Ge and Si and (b) ideal band alignment of Ge on Si derived from Anderson's affinity rule [38].

However, experimental measurements show the energy bands as well as the band alignment does change in the presence of strain and does depend on interface properties. Further investigation into the band edge modification is warranted to establish the proper HJ band alignment. In general, for a strained $Si_{1-x}Ge_x$ layer grown on (001) $Si_{1-y}Ge_y$ virtual substrate (unstrained), the calculated valence band offsets is comparable to the experimental results: $\Delta E_{V,av} = (x-y)\cdot(0.47-0.06y)$ eV, where $\Delta E_{V,av}$ is weighted averaged potential of strain-split heavy hole (HH) and light hole (LH) bands [12, 40]. The HJ band alignment of a strained $Si_{1-x}Ge_x$ layer on relaxed $Si_{1-y}Ge_y$ substrate has several general features. First, the valence band maximum always occurs in the higher Ge content layer. Second, for $x < y$, the energy band alignment is always of type-II regardless of x and y. Lastly, for $x > y$, the conduction energy band is expected to be nearly flat with $\Delta E_C < 20$ meV. Thus, for Ge or Ge-rich layer grown on unstrained Si, the alignment is quasi type-II (Figure 2.12) with the difference in the materials' bandgaps reflected as valence band offset (i.e., E_g or ΔE_v depends on Ge content and/or strain at the heterointerface) [40, 41].

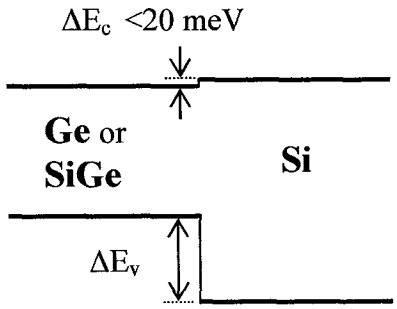

Figure 2.12 Band alignment of Ge or SiGe on relaxed Si substrate.

Under the presence of strain, not only do the relative energy levels (ΔE_V and ΔE_C) differ from the bulk characteristics but the bandgaps of the materials alter. Si and Ge, as well as $Si_{1-x}Ge_x$ alloys have indirect bandgaps with similar valence band structures and different conduction band structures in reciprocal space. For unstrained bulk Si, the conduction band minima are sixfold degenerates along the [100] direction, between Γ and X points and commonly referred to as the Δ minima. On the other hand, unstrained bulk Ge has conduction band minima that are eightfold degenerate along the [111] direction, at the edge of Brillouin zone, near the L point and referred to as the L minima (Figure 2.13).

In unstrained $Si_{1-x}Ge_x$ alloys, the room temperature bandgap changes from 1.12 to 0.66 eV as the Ge content x increases from 0 to 1. For low to moderate Ge content ($x < 0.85$), the conduction band is Si-like with Δ minima along the [100] direction. At high Ge content ($x > 0.85$), the conduction band is Ge-like with L minima along the [111] direction (Figure 2.14, top curve) [40, 42].

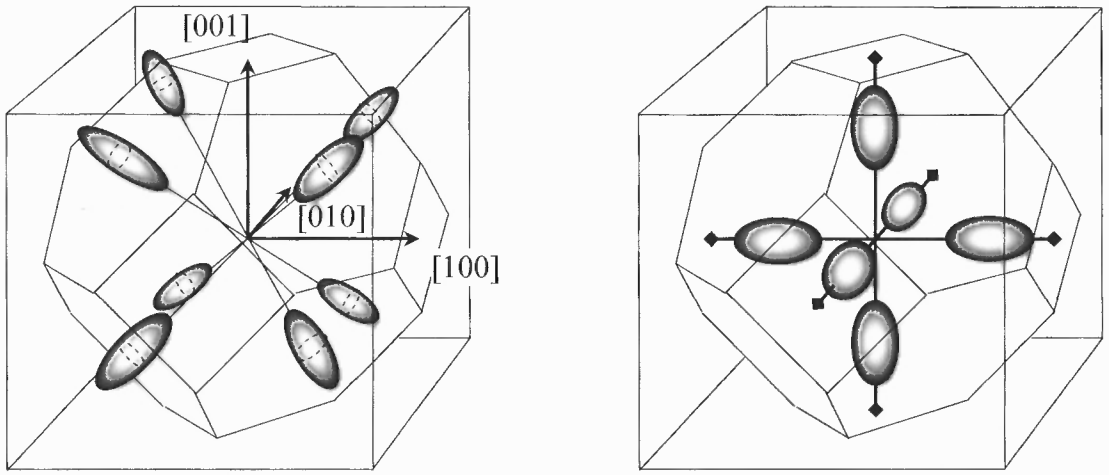

Figure 2.13 The conduction bands of bulk Ge and Si in the Brillouin zone [43].

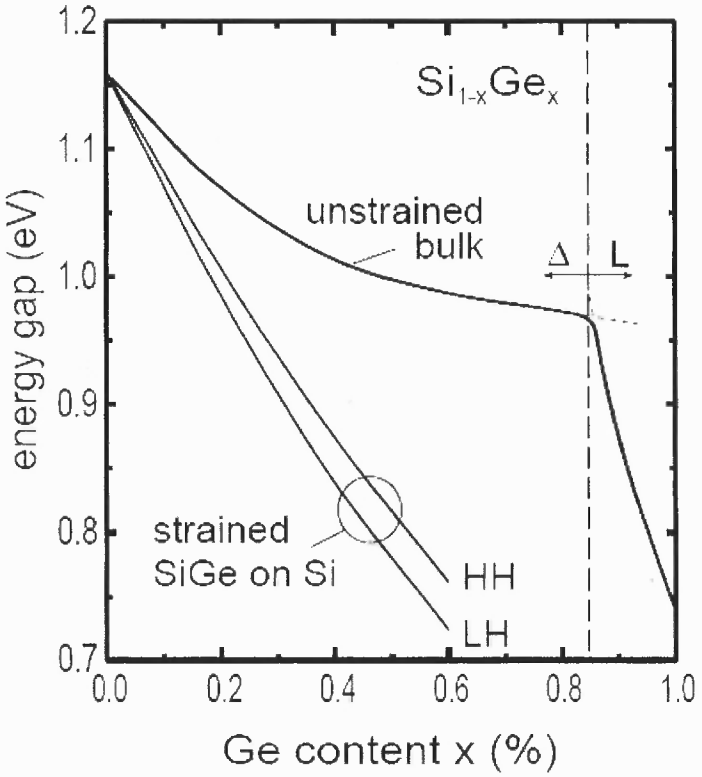

Figure 2.14 Bandgap of strained and unstrained (as indicated) $Si_{1-x}Ge_x$ alloys with respect to Ge content, x. The unstrained alloy bandgap curve shows transition from Si-like Δ minima to Ge-like L minima at x=0.85 [40, 42].

The $Si/Si_{1-x}Ge_x$ multilayer samples studied in this dissertation has moderate Ge content of ~0.5 in the $Si_{1-x}Ge_x$ layers and therefore Si-like conduction band with Δ minima. The SiGe sandwiched Si layers are under compressive strain while the Si layers are under tensile strain, both in the lateral direction, causing shifting and degeneracy splitting of energy band edges into Δ(2) and Δ(4) bands, shifting in opposite directions. In Si, Δ(2) bands shift to lower energy and Δ(4) bands shift to higher energy. In SiGe, Δ(2) and Δ(4) move in opposite directions. As a result, fundamental band gap is formed between Δ(2) (in the [100] direction) and LH for tensilely strained $Si_{1-x}Ge_x$ and Δ(4) (within the layer plane) and HH for compressively strained $Si_{1-x}Ge_x$ (Figure 2.14, lower curves) [40, 42, 44]. The shifting and splitting of the bands also result in lower conduction band in the wide gap material (Si), forming a quasi type-II HJ.

For the 2D multilayers, lateral strain is tensile in the Si layers and compressive in the SiGe layers. In the 3D clusters, the strain-induced S-K growth mode forms clusters for elastic relaxation. Therefore, the Si above and below the elastically relaxed SiGe clusters experience tensile strain and while the Ge-rich cluster experience compressive strain. Figure 2.15 shows a simplfied energy band alignment of Si/SiGe multilayers.

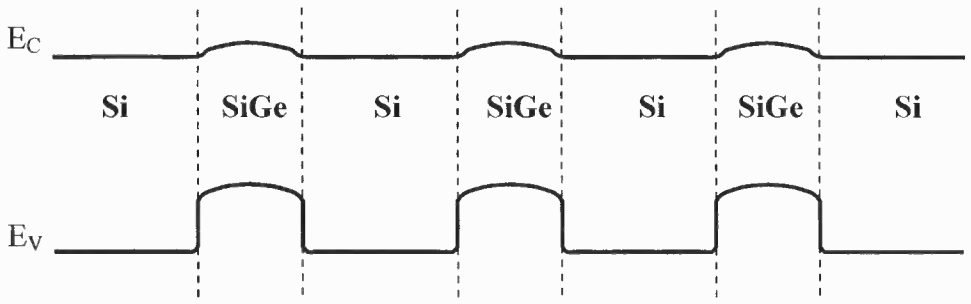

Figure 2.15 Band alignment for Si/SiGe multilayers.

2.2.3 Thermal Properties

In addition to the unique electronic and structural properties of bulk c-Si, single crystal Si possesses one of the best known lattice thermal conductivity [45, 46]. This exceptional heat conductance is critically important for Si device heat management and circuit reliability. However, most of the modern CMOS platforms are no longer single crystal Si wafers but rather thin layers of Si-on-insulator (SOI), ultra-thin strained Si and SiGe hetero-structures that are the foundation of SiGe HBTs, and high mobility metal-oxide-semiconductor field-effective transistors (MOSFETs). Major properties of these Si-based nanostructures are very different compared to that in bulk c-Si. For example, thermal conductivity in ultra-thin SOI layers, SiGe alloys and Si/SiGe nanostructures could be reduced by more than an order of magnitude compared to that in c-Si [18, 20, 47, 48], and heat dissipation has became an important issue for modern nanoscale electronic devices and circuits. Thus, the understanding and improvement of heat management in Si-based nanostructures is critically important for the evolution of microelectronic industry. On the other hand, many interesting applications of nano-structured Si (ns-Si) in photonic devices and CMOS-compatible light emitters were recently discussed [49-53]. These ns-Si materials and devices produce an efficient and tunable light emission in the near-infrared and visible spectral region [54, 55]. Also, it has been shown that under photoexcitation with energy density > 10 mJ/cm^2, optical gain is, possibly, achievable [56-60]. Such energy density absorbed by a sub-micrometer film generates a lot of heat. Thus, thermal properties and heat dissipation in ns-Si based photonic devices need to be understood in great details. Many device applications were recently proposed for the Si and SiGe nanostructures studies in this dissertation (e.g., Si nanowire electrical interconnects [36, 61], Si nanowire

thermoelectric devices [62, 63], Si nanowire sensors [64-66], SiGe cluster-based memory devices [67-69], SiGe cluster-based near-infrared light emitters [70-74], etc.), and detailed understanding of thermal processes in these nano-structures is absolutely necessary.

In general, thermal energy in a solid is transported by the means of particles or quasi-particles moving to restore thermodynamic equilibrium in a system with a temperature gradient ∇T. In metals, heat is mainly conducted by mobile electrons (i.e., electronic thermal conductivity κ_e), while in insulators and lightly doped semiconductors, heat is primarily transported by phonons. Phonons are quasi-particles representing lattice vibrations, and phonon processes are responsible for the lattice thermal conductivity κ_l. An ideal pure single crystal is an excellent thermal conductor because phonon inharmonicity (i.e., inelastic phonon scattering) is the only phonon mean free path limitation. When electronically active dopants (donors and acceptors) and other impurities are introduced into a pure single crystal, phonon scattering associated with impurity atoms strongly reduces the lattice conductivity. For crystallites with reduced dimensions, such as micro- or nano-crystals (nc), the conductivity decreases as the grain size of the crystallites decreases, mainly due to phonon scattering at the grain boundaries. This effect becomes dominant as the grain size approaches the phonon mean free path in a single crystal. Thermal conductivity in amorphous Si (a-Si) is drastically reduced, mainly because the ideal Si crystal lattice with the long range atomic order is replaced by an amorphous network of Si atoms. Furthermore, amorphous materials might have significant number of structural defects providing additional phonon scattering. Similarly, crystalline alloys (e.g., SiGe, SiCGe, etc.) have strongly reduced thermal conductivity due to compositional disorder. Figure 2.16 summarizes experimental results on thermal conductivity in different

forms of c-Si, SiGe-alloy-based nanostructures, a-Si and ns-Si-based materials [18, 75-77]. In these Si-based nanostructures and compounds, thermal conductivity is reduced dramatically compared to that in c-Si, from ~10^3 to less than 10^{-1} W/m-K at T=100K (Figure 2.16).

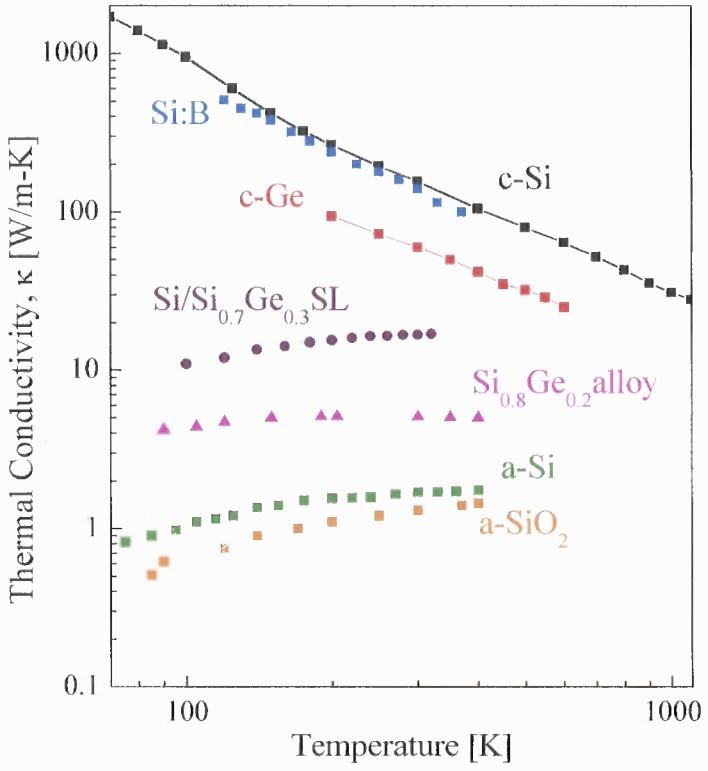

Figure 2.16 Temperature dependence of thermal conductivity of Si-based materials and nanostructures, including c-Si, a-Si, a-SiO_2, lightly B-doped c-Si ($4 \cdot 10^{14}$ cm^{-3}), $Si/Si_{0.7}Ge_{0.3}$ SL (200 Å /100Å), and $Si_{0.8}Ge_{0.2}$ alloy. Thermal conductivity of c-Ge is also included for comparison. Note the double logarithmic scale. Data compiled using Ref. [18, 75-77].

In addition, thermal conductivity temperature dependence is found to be qualitatively different in c-Si, Si-based alloys, amorphous materials and nanostructures. An overview of the classical kinetic theory which is the foundation of thermal physics can

be found in Appendix A. It mainly consider lattice thermal conductivity in semiconductors, and specifically focuses on phonon boundary scattering, which is primarily responsible for the observed thermal conductivity reduction in different forms of Si nanostructures (Figure 2.16). A brief overview of thermal conductivity measurement techniques for micro- and nano-scale materials and devices is provided in Appendix A. The following is a general discussion and comparison of thermal properties of the Si and Si/SiGe nanostructure studied in this dissertation.

A strong thermal conductivity size-dependence is found in 1D Si nanostructures or NWs with typical diameter < 100 nm. One of the proposed applications for the NWs is thermoelectric devices. Thermal conductivity of individual Si NWs was studied using a micro-device containing two bridging membranes, a technique specifically developed for low-volume objects [63, 78, 79]. In individual Si NWs with diameters ranging between 115 and 22 nm, the measured thermal conductivity clearly exhibits a dependence on the NW diameter, which is summarized in Figure 2.18 (from ref. [80]). It has been proposed that phonon boundary scattering is the dominant mechanism controlling thermal conductivity in Si NWs [80]. Thus, in 1D Si nanostructures, thermal conductivity is controlled by the nanostructure characteristic size (when it is comparable or smaller than phonon mean free path) and by quality of the interfaces.

Bulk crystalline SiGe alloys have quite low thermal conductivity, mainly due to their compositional disorder [81, 82]. It has been proposed that Si/SiGe superlattices (SLs) with an enhanced carrier transport and an even lower thermal conductivity due to the nanometer-thick layers could be used in efficient thermoelectric devices [18-21]. Figure 2.17 summarizes some studies demonstrating that, in undoped Si/SiGe SLs, thermal

conductivity mainly depends on interface roughness, density of interface defects, and non-uniform strain due to the 4.2 % lattice mismatch between Si and Ge. In doped Si/SiGe SLs with a possibility of dopant segregation at the Si/SiGe hetero-interfaces, thermal conductivity is found to be reduced by ~50-60% (Figure 2.17) [19]. It has also been proposed that in Si/SiGe 3D, i.e. cluster morphology multilayers, thermal conductivity could be reduced even further [83].

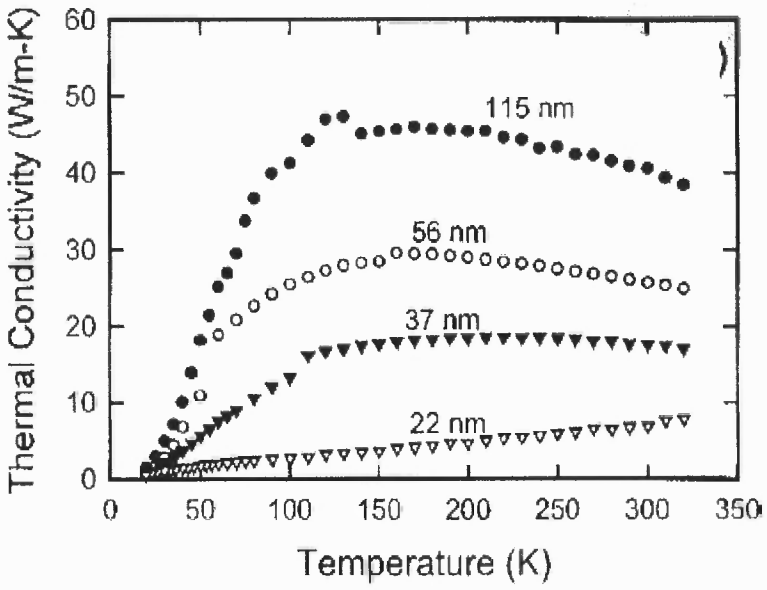

Figure 2.17 Thermal conductivity temperature dependence in controlled (indicated) diameter Si NWs [80].

There are many reports on thermal conductivity in 2D and 3D Si/SiGe multilayers studied by 3ω or similar electrical methods [19, 84-87], and fewer data collected by optical measurements [88-91]. The calculated thermal conductivity obtained from the optical measurements is found to be close to values obtained by the 3ω method. It has been noticed that in several samples with significant degree of SiGe cluster vertical self-ordering, thermal conductivity slightly increases [92].

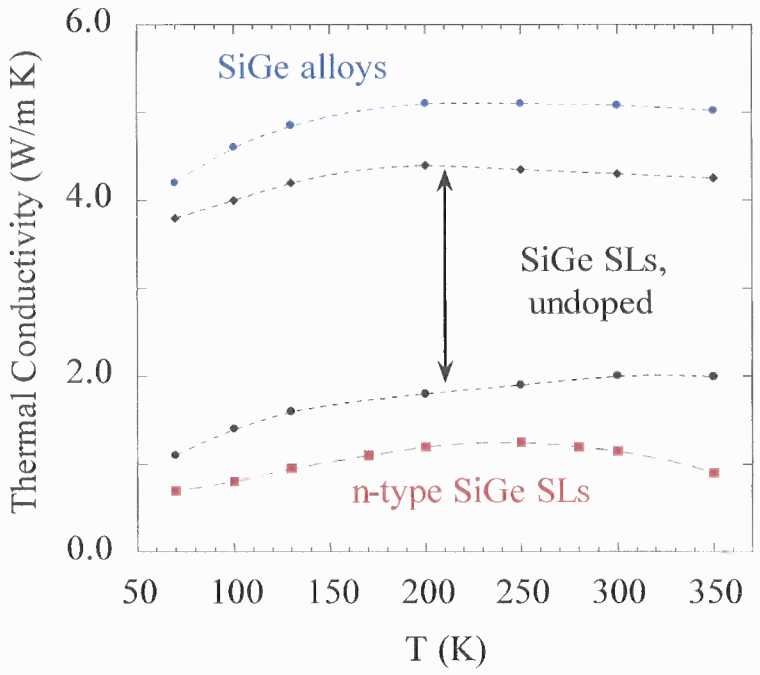

Figure 2.18 Thermal conductivity temperature dependence in SiGe alloys and SiGe superlattices (SLs). Note: data complied from [18-21].

2.2.4 Optical Properties: Photoluminescence

In photoluminescence (PL), carriers are generated under the illumination of a light source, and photons are emitted as these carriers recombine. The recombination process for the indirect bandgap Si and Ge does not occur directly across the bandgap but through phonon assistance for conservation of momentum. Other possible recombination process can be through a defect or trapping level [93]. Strain in semiconductors lowers the energy bandgaps of the materials, and as a result, the PL spectra shift toward lower photon energies [94]. Thus PL can be used to determine the bandgap, strain and the existence of defects. Figure 2.19 is a low temperature (10 K) PL spectrum of c-Si. Since Si is indirect bandgap material, carrier recombination is mostly phonon-assisted and the peaks are marked with the major phonon modes: transverse optical (TO), transverse acoustic (TA) and combination of two transverse optical phonons (2TO).

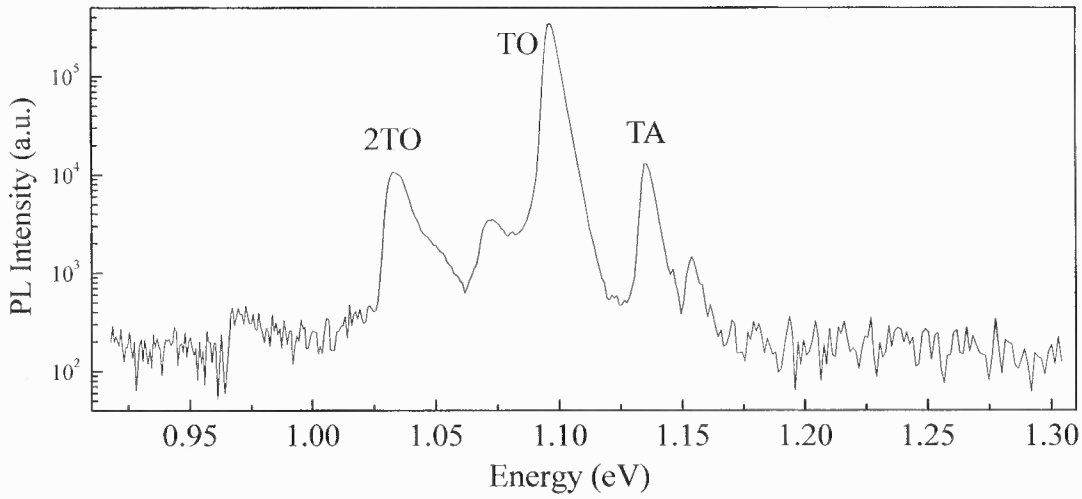

Figure 2.19 Photoluminescence spectrum of c-Si at low temperature (10K) with phonon modes as marked. Note the vertical logarithmic scale.

In SiGe, the strain-induced bandgap narrowing effect (described in subsection 2.2.2) can be observed in the shifting of PL peaks. By finding the PL peak positions and taken in account the known phonon energies (at $x < 0.85$, $TO_{Si\text{-}Si(\Delta)}$ is 58 meV, $TO_{Ge\text{-}Ge(X)}$ is 34.5 meV and is $TO_{Si\text{-}Ge}$ is 48 meV), the bandgap of the SiGe nanostructure can be found. Moreover, using the major PL peak positions from SiGe nanostructures and the information from literature, the SiGe composition can be estimated. Another notable SiGe PL characteristic is the are the stronger direct optical transitions (no phonon or NP) due to the relaxed selection rules [94]. In c-Si, the NP transition has < 1% intensity of the TO PL peak; while in SiGe, it can be comparable or even stronger than TO. Figure 2.20 shows a series of PL spectra in SiGe alloys with different composition. The PL peaks are marked with X_i^j, where j gives the type of transition (NP or phonon assisted) and i gives the nature of the phonon (Si-Si, Si-Ge or Ge-Ge) [94].

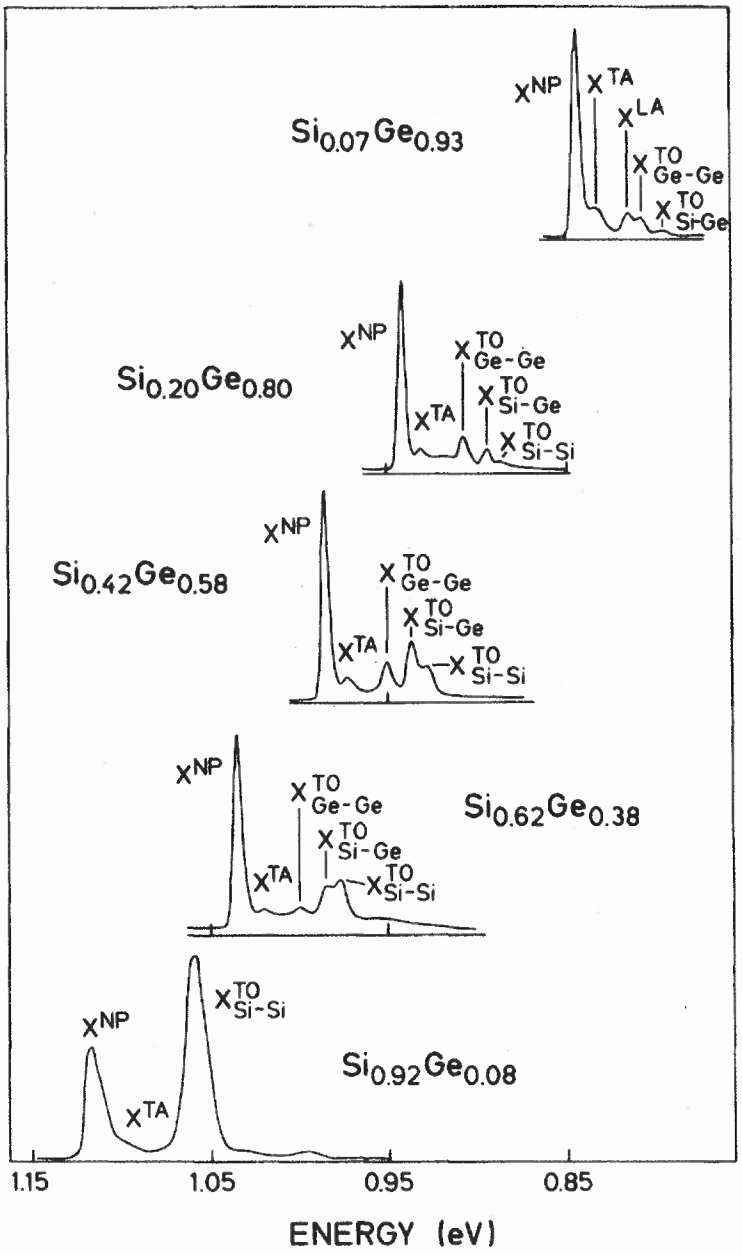

Figure 2.20 Photoluminescence spectrum of SiGe alloys at low temperature (4.2 K) with transition modes marked with X_i^j, where j gives the type of transition and i gives the nature of the phonon [94].

2.2.5 Optical Properties: Raman Scattering

When light travels through a medium, most of it is reflected, transmitted or absorbed following the laws of reflection and refraction and a small portion of the light is scattered by inhomogeneities inside the medium. From the quantum mechanics point-of-view, when a photon is incident on a molecule, the energy it carries excites an electron and elevated the electron to a higher energy state. Scattering happens when the incident photon excites a conduction band electron to virtual energy states that has lower in energy than real electronic states. The electron then relaxes quickly either to a vibrational state or to the ground state, often with a change in vibrational energy, and emits a photon. There are two types of scattering: elastic and inelastic. Elastic scattering, e.g. Rayleigh scattering, emits photons with the same frequency as the incident photon. Inelastic scattering emits photons with different frequency (energy) from the incident photon. Raman scattering is an example of inelastic scattering due to energy transfer as molecular vibrations, i.e. interactions between photons and phonons [95].

In solids with transitional symmetry, such as crystals, the wave vectors are restricted in the first Brillouin zone, whose zone edge is defined as the reciprocal space π / R, where R is the translational period [95]. In a crystal, the wave vectors take the forms a phonon energy-momentum dispersion relationship in reciprocal space. Figure 2.21 (a) shows the first Brillouin zone (commonly referred to as just "Brillouin zone") of the phonon dispersion relationship with zone edge π / a, where a is the lattice constant. In the Brillouin zone, the optical phonon has near constant energy while the acoustic phonon energy increase linearly around from zone center (k=0). When a light of wavelength λ incites the crystal, its wave vector is represented as a vertical line at position $k = \pi / \lambda$ in

reciprocal space, close to the zone center ($\lambda >> a$). The photon-phonon interaction is shown as the intercepting points of the π / λ line and the phonon curves: the interception with acoustic phonon is Rayleigh scattering and the interception with optical phonon is Raman scattering. The strong optical phonon can be detected while acoustic phonons, at low frequencies close to the laser line, are hard to detect.

In an ideal, periodic, multi-layered heterostructure with abrupt and defect free interfaces, such as superlattices, interference by reflected wave vectors, which satisfy the Bragg condition, forms a standing wave known as the reduced Brillouin zone or Brillouin minizone (BMZ), with new edge π / d, where d is the period of the structure [95-98]. The phonon dispersion relationship folds between the zone center and the BMZ edge, and Figure 2.21 (b) is an illustration of the phonon folding. When probing the BMZ, the excitation wave vector becomes in the center of the BMZ or even close to the zone edge, enabling the detection of the characteristic doublets of the folded acoustic phonons at higher frequency. These measurements can be use to reconstruct the BMZ for a better understanding of spatial localization in semiconductor nano-structures [99]. The optical phonon folding, however, is difficult to resolve, and the detected Raman scattering of the optical phonon, in the presence of BMZ formation, becomes a broader peak.

Raman shift is the difference between the incident and scattered photon frequencies. When a phonon is emitted in the scattering process ($\omega_S = \omega_i - \omega_o$), the scattered light frequency is Stokes shifted; on the other hand, an anti-Stokes shift is when the scattered light has higher energy than the incident light due to phonon absorption ($\omega_{AS} = \omega_i + \omega_o$). Note that ω_S, ω_{AS}, ω_i and ω_o are the Stokes, anti-Stokes, incident light and vibrational phonon frequencies, respectively.

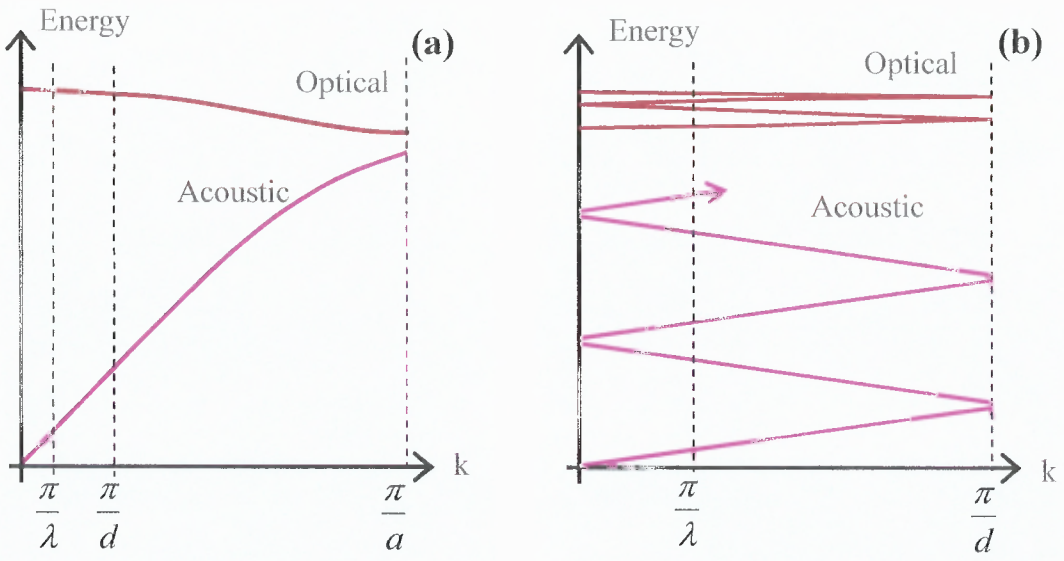

Figure 2.21 Phonon dispersion relationship of (a) crystals and (b) periodic structures, where a, d and λ are the lattice constant of the crystal, the periodicity of the structure and the wavelength of the excitation laser used in Raman spectroscopy, respectively. Note: (b) is a schematic drawing demonstrating the zone folding phenomenon and is not drawn to scale with respect to (a).

The Stokes and anti-Stokes spectra shift from the laser line by the same amount of photon energy, which is equal to the energy of the emitted or absorbed phonons, respectively. In semiconductor bulk crystals, layered structures, and superlattices, the frequencies or locations of different peaks denote vibrations between two particular atoms such that they carry information about phonon dispersion, chemical composition and presence of impurities. Strain in the sample can also be deciphered by the shift of the spectrum; tensile strain in the structure will shift the line toward higher frequency while a compression strain will shift the line toward lower frequency [100, 101]. The ratio of Stokes to anti-Stokes intensity at a particular vibrational frequency is an indication of

the local temperature, which can be obtained from the Boltzmann relation [102-105]:

$$T = \frac{\hbar\omega_0}{k_B \cdot \ln(I_S / I_{AS})}, \tag{2.3}$$

where $\hbar$, k_B, I_S and I_{AS} are the reduced Planck constant, Boltzmann constant, Stokes intensity and anti-Stokes intensity, respectively.

Figure 2.22 is a Raman spectrum in c-Si (n-type Si wafer). Si exhibits a strong and narrow single phonon peak at ~520 cm^{-1}, which corresponds to the zone-center optical (transverse, TO and longitudinal, LO) phonons. The two broad Raman features on either side of the optical phonon line are originated from scattering involving two or more phonons. The much weaker low frequency band around 200-450 cm^{-1} is an overtone of acoustic phonons, the features around 600-700 cm^{-1} is the combination of one optical phonon and one acoustic phonon, and the high frequency peak around 900-1050 cm^{-1}, commonly referred to as the Si second order, is an overtone of two optical phonons in combinations with some acoustic phonons [95, 106].

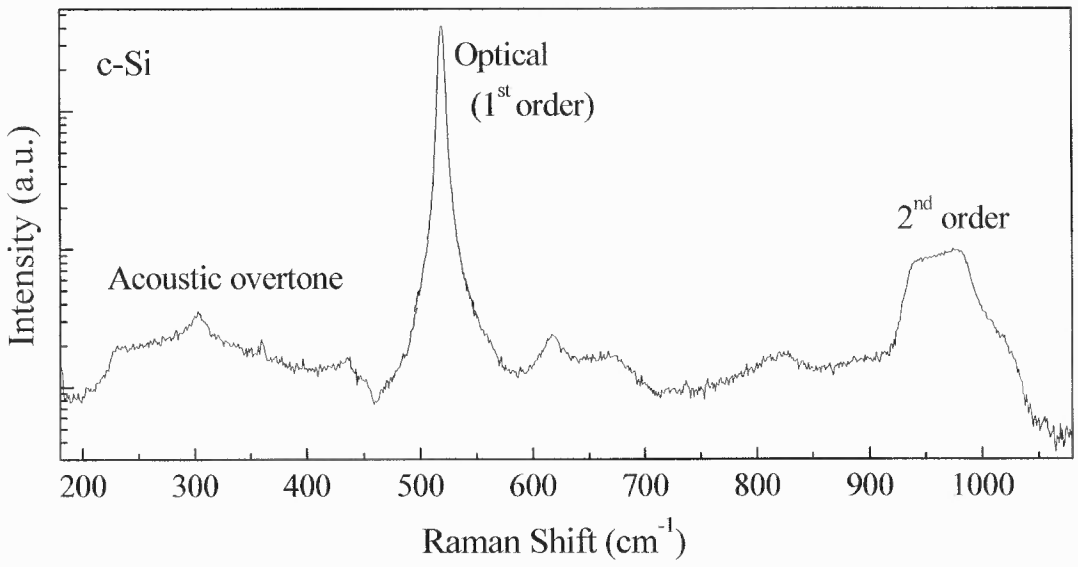

Figure 2.22 Raman spectrum of a c-Si sample under 488 nm excitation. The major Raman features are marked with the phonon modes associated with them. Note the vertical logarithmic scale.

In SiGe materials and systems, Raman spectroscopy is a unique characterization technique due to the multi-modal nature of Raman scattering from optical phonons in SiGe [34, 84, 92]. Typical Raman spectra reveal three major vibrational modes known respectively as the Si-Si vibration at ~520 cm^{-1}, the Si-Ge vibration at ~410 cm^{-1} and the Ge-Ge vibration at ~300 cm^{-1}. Figure 2.23 is an example of the SiGe Raman spectrum with laser line, Stokes and anti-Stokes signals. The sample is a 3D Si/SiGe cluster multilayers. Raman features also reveals strain in the SiGe nanostructure. Additional features around ~505 and ~250 cm^{-1} reveal the existence of stained Si-Si and Ge-Ge vibration; while the shifting of the positions of three major peak can be used to calculate the amount of strain [107, 108].

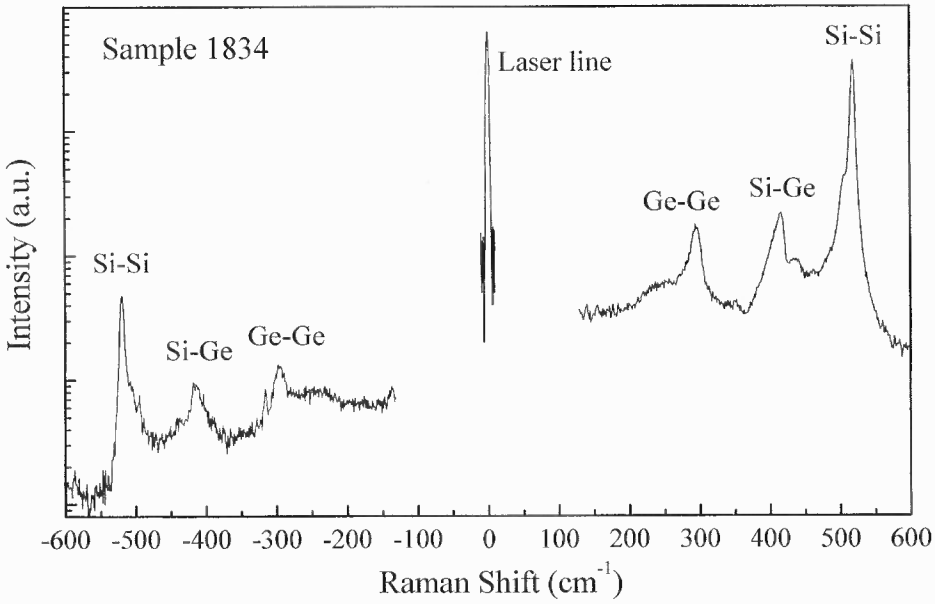

Figure 2.23 Raman spectrum in Stokes and anti-Stokes region of a Si/SiGe 3D multilayer sample under 488 nm excitation. The laser line and major Raman features are marked with the phonon modes associated with them. Note the vertical logarithmic scale.

CHAPTER 3

EXPERIMENTAL METHODS

3.1 Scanning Electron Microscopy

Using the short wavelength of electron beams (<1 Å), electron microscopes are able to achieve much higher resolution than their optical counterparts. In a scanning electron microscope (SEM), by moving a tightly focus electron beam across the sample surface, collecting and counting either the reflected electrons or secondary electrons, 3D images of the sample surface can be generated on the control monitor. Figure 3.1 shows a schematic of the SEM and a high magnification SEM image of Si NWs grown using VLS technique in CVD with Au catalyst. The SEM images in this research are prepared using a LEO 1530VP field emission scanning electron microscope in the Material Characterization Laboratories at NJIT. The microscope operates at high voltage mode with voltages ranging from 0.1k eV to 30k eV, magnification of 20k to 900k times and resolution up to 1 nm. The sample is held in high vacuum on a sample stage that is equipped with motorized controller for moving and rotating laterally, allowing access to multiple samples. The stage also tilts along a central axis with manual control outside the chamber, enabling scans of the sample at angles from -15° to 90°. The images shown in this research are taken by collecting the reflection of electrons with the in-lens detector at moderate voltages of 1k-10k eV.

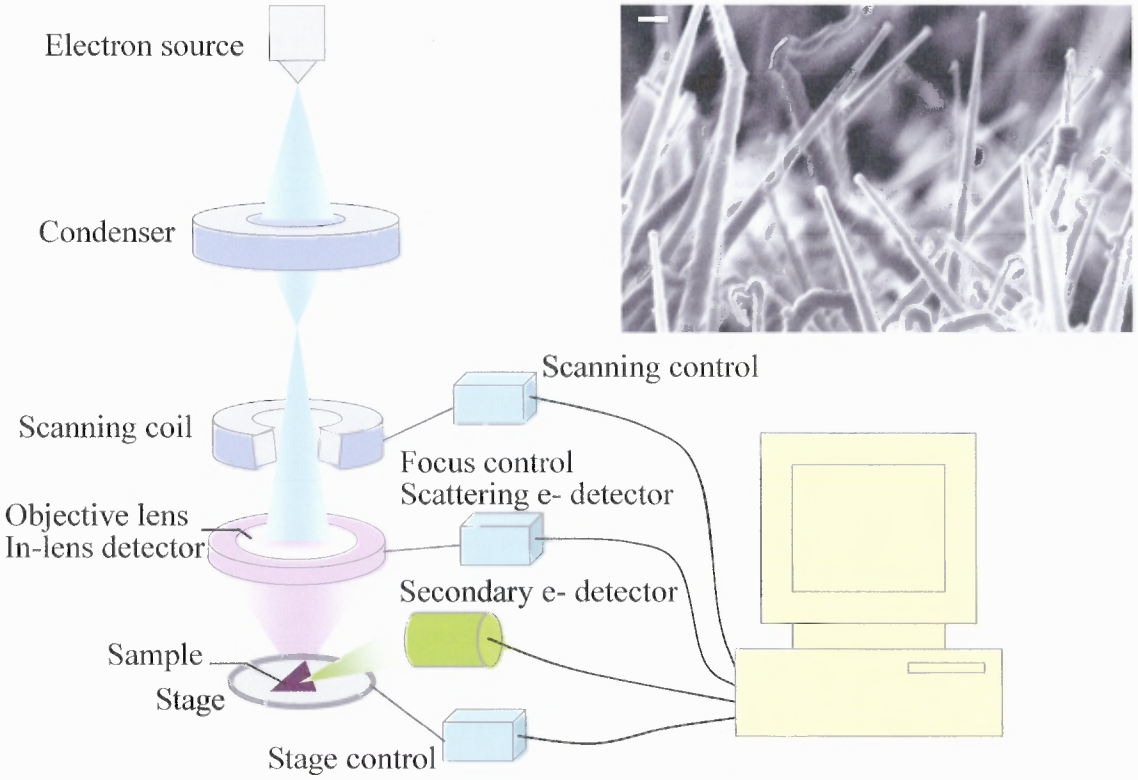

Figure 3.1 Schematics of a scanning electron microscope (SEM) and a high magnification (scale bar equals to 500 nm) image of a Si NW sample taken with the stage tilted to 85° from normal (near side view).

3.2 Photoluminescence Spectroscopy

In the PL setup used in this research, the samples are held in a He closed-cycle cryostat, wherein the temperature can be controlled in the range of 10 to 300 K. A multi-line Ar^+ laser with a wavelength selector is used as excitation source with intensity varied from 0.1 to 10 W/cm^2. The laser is modulated by a mechanical chopper. The PL signal is dispersed using a single grating Acton Research 0.5 m focal length monochromator and detected by a cooled InGaAs photomultiplier tube (PMT) or charged-couple device (CCD) camera in the range of 0.9-1.6 μm. The dispersed signal is amplified by a lock-in amplifier in reference to the mechanical chopper and recorded by Spectra Sense software.

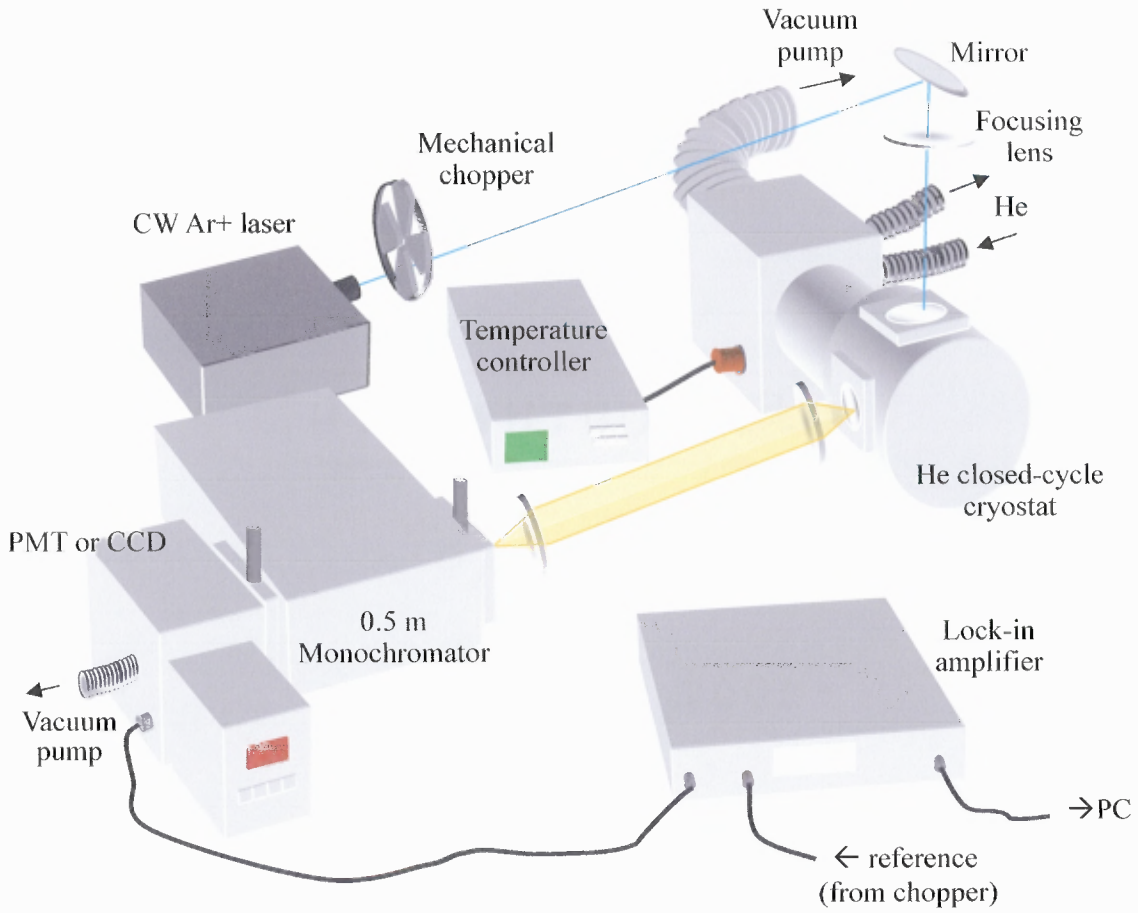

Figure 3.2 Schematic of photoluminescence measurement setup [43].

3.3 Raman Spectroscopy and Raman-based Thermometry

To measure a Raman spectrum, a source of collimated and monochromatic light is required. For the measurements in this research, an Ar^+ laser is used as the excitation source for Raman spectra measured at room temperature in a flexible geometry. The laser light passes through a polarizer to ensure single polarization, and the measurements are done with incident light at or close to Brewster's angle (<3 % reflection, measured by a Newport optical power meter equip with a Si photodetector). The multi line feature of the Ar^+ laser provides choices of wavelengths best fitting the measurements with maximum power intensities, measured at the sample, ranging from ~10 kW/cm^2 (with 514.5 nm) to

~2 kW/cm^2 (with 457.9 nm). The scattered light is analyzed by a Jobin Yvon U-1000 double spectrometer with focal length of 1000 mm, wavelength range of 185-40000 nm and resolution up to 0.004 nm [109]. The spectrometer is equipped with a thermoelectrically cooled Hamamatsu R943-02 photomultiplier tube (PMT) and photon counting system. The PMT has maximum spectral response in the wavelength range of 300-800 nm and a low dark current count of ~20/s. The measurements done in this research include detecting scattered light with wavelength in the range of approximately 430-550 nm, which is located in the optimal region for the spectrometer and PMT performances [110].

In Raman-based thermometry, the Ar^+ laser beam is used both as the heating source and as the photo-excitation source. Although the index of refraction is temperature dependent, the change is miniscule and the resultant change in reflectivity is well within the estimated 3% reflection error. For instance, Si has refractive indexes of $n_{Si}^{300K} = 4.8$ and $n_{Si}^{450K} = 4.9$ [111] and room temperature Brewster's angle of $\theta_B^{300K} = 78.232°$, at which the laser incident angle is set. When the surface temperature is increase to 450 K, the increased index of refraction changes reflectivity. Using Fresnel equations, the reflectivity can be found as $R^{450K} \sim 1\times10^{-4} \sim 0.01\%$ (calculated with θ_B^{300K} and n_{Si}^{450K}). Similar calculations are done using $Si_{1-x}Ge_x$ indexes of refraction and the change in reflection from 300 to 450K is found to be within 2%. Therefore, taking in account the surface scattering (measured by the optical power meter) and the changes in reflectivity due to increase of temperature and refractive index, the difference between power intensity measured by the detector and power absorbed in the sample is $\leq$10%. Note that this discrepancy in applied power does not affect the Raman-based temperature calculation.

The penetration depths of green (514.5 nm) and blue (457.9 nm) laser lights in Si are ~600 and ~300 nm, respectively; while both wavelength have very short penetration depth of ~20 nm in Ge [39, 112]. Therefore, the laser penetration depth in the Ge-rich SiGe multilayers is estimated to be ~20-50 nm. Thickness of Si wafer typically is in the range of 150-500 μm, depends on the diameter of the wafer. The nanostructures studied are fabricated on small diameter wafers with thickness in the range of a couple hundred microns. When considering the whole system (c-Si wafer reference sample or Si and SiGe nanostructures on top of a carrier wafer), the penetration depth is <1% of the total thickness. Hence, the laser light creates a thin virtual heating strip atop the sample. Figure 3.3 shows a schematic of the nanostructure on a carrier wafer under laser excitation. The spot size in the Raman setup is in the range of ~$(0.1\ mm)^2$=$(100\ \mu m)^2$=$10^{-8}\ m^2$, which is comparable to the wafer thickness; thus the heat conduction is generally in the cross-plane direction, with low heat loss in the in-plane direction (Figure 3.3).

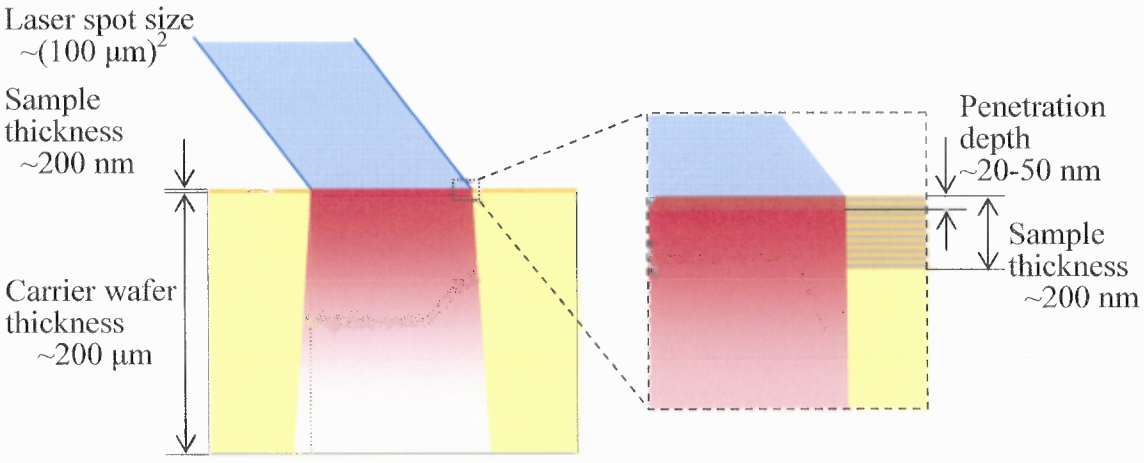

Figure 3.3 Schematic for Raman-based thermometry with dimensions of the laser beam, sample thickness and carrier wafer thickness as marked.

By comparing the topside Raman temperature (calculated using Equation 2.3) and the wafer backside temperature (measured by a thermal-couple thermometer), the overall system thermal conductivity can be found as [113]

$$\kappa = P \cdot \frac{L}{A} \cdot \frac{1}{\Delta T} , \tag{3.1}$$

where P is the laser power in Watts, L is the heat conduction path length (approximately the carrier wafer thickness, 200 μm), A is the cross-sectional area of heat conduction (approximately the laser spot size, 10^{-8} m^2) and ΔT is the temperature gradient between the Raman temperature and the backside temperature. Figure 3.4 shows the calculated thermal conductivity of a Si wafer compare to the thermal conductivities of c-Si and moderately B-doped Si:B from literatures [75, 114]. It shows that Raman-based thermometry and thermal conductivity calculation yields reasonably accurate results.

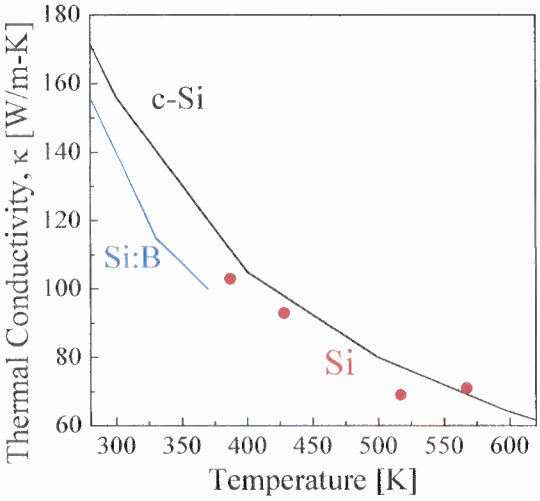

Figure 3.4 Comparison of Si thermal conductivity: intrinsic c-Si and moderately B-doped Si from literatures (Ref. [75, 114]) as solid lines, and Raman-based thermometry thermal conductivity calculation of a c-Si wafer in dots.

3.4 Electrical Measurements

For the electro-optical and electrical measurements of the delta-doped Si/Si:B multilayers, the top contacts are fabricated by sputtering thin, semi-transparent (~50 nm) Au dots on the samples and connected to Ag wires by soldering with Wood's alloy. The back contacts are made by affixing the sample on thin Cu tape with silver paste, and Ag wires are soldered to the Cu tape with Wood's alloy (Figure 3.5). The room temperature pulse-modulated optical reflectance of the Ar^+ laser is measured using a LeCroy 9310M oscilloscope. The electrical measurements, including current-voltage (I-V) and capacitance-voltage (C-V) characteristics in the dark and under illumination by an Ar+ laser were performed at room temperature using an automated system based on a Keithley 6517A electrometer.

3.5 Transmission Electron Microscopy (Collaboration)

The transmission electron microscopy (TEM) uses high-energy electron beam transmitting through ultra thin samples. As the beam passes through the sample, the interactions of electrons and the sample form an image that is magnified and recorded by detectors. The TEM is commonly used to analyze thin film or multilayer samples in the cross-sectional direction. Comparing to SEM, TEM provides much high resolution. High resolution TEM can provide details of lattice structures by recording the lattice fringes as the electron beam diffracts at the lattice planes. The Si/SiGe multilayer TEM images shown in this dissertation are performed by NRC Canada on a JEOL JEM-2100F field emission source transmission electron microscope operating at 200 kV. High angle annular dark field (HAADF) scanning TEM images were obtained using a Fischione annular dark field

detector attached to the JEM-2100F to enhance chemical contrast in SiGe heterostructures. The Si/Ge NW HJ sample is analyzed by high-resolution TEM (HR-TEM) and dark-field TEM (DF-TEM) in HP Labs using a Philips CM20 field-emission TEM.

The chemical composition of the various SiGe nanostructures is studied quantitatively by the TEM analytical techniques of energy-dispersive x-ray spectroscopy (EDX). EDX provides a fast and nondestructive analysis a sample at a single point, along a line or over a plane. The EDX spectra of Si/SiGe multilayers shown in this dissertation are done in NRC, Canada using an Oxford INCA Energy TEM 200 attached to the JEM-2100F and electron energy loss spectroscopy (EELS) using a Gatan GIF Tridiem attached to the JEM-2100F. The EDX spectra are calibrated by probing thick $Si/Si_{1-x}Ge_x$ heterostructures of known germanium composition [14].

CHAPTER 4

RESULTS AND DISCUSSION

4.1 Si/Si:B Delta-doped Multilayers

The nominal physical parameters for the various delta-doped samples are presented in Table 4.1. The doping profile for these samples was measured by secondary ion mass spectrometry (SIMS) using a Cameca 4f magnetic sector SIMS system. Figure 4.1 shows one of the SIMS dopant concentration profiles. The profiles were calibrated using a boron-doped Si(001) standard. For these measurements, an oxygen ion primary beam and a sputtering rate of about 0.5 nm/s is used.

Table 4.1 Details on Sample Fabrication of Si/Si:B Multilayers

Sample #	T (B cell) [°C]	$t_{Si:B}$ [nm]	t_{Si} [nm]	N_A [cm^{-3}]
1815	1575	4	10	$1 \cdot 10^{18}$
1816	1575	4	20	$1 \cdot 10^{18}$
1817	1650	2.5	40	$5 \cdot 10^{18}$
1818	1530	2.5	10	$5 \cdot 10^{17}$
1819	1650	2.5	10	$5 \cdot 10^{18}$
1820	1650	2.5	10	$5 \cdot 10^{18}$
1821	1650	1	10	$5 \cdot 10^{18}$

Note: T (B cell), temperature of the Knudsen effusion cell filled with elemental boron; $t_{Si:B}$, delta-doped Si:B layer thickness; t_{Si}, Si separating layer thickness; N_A, nominal dopant concentration

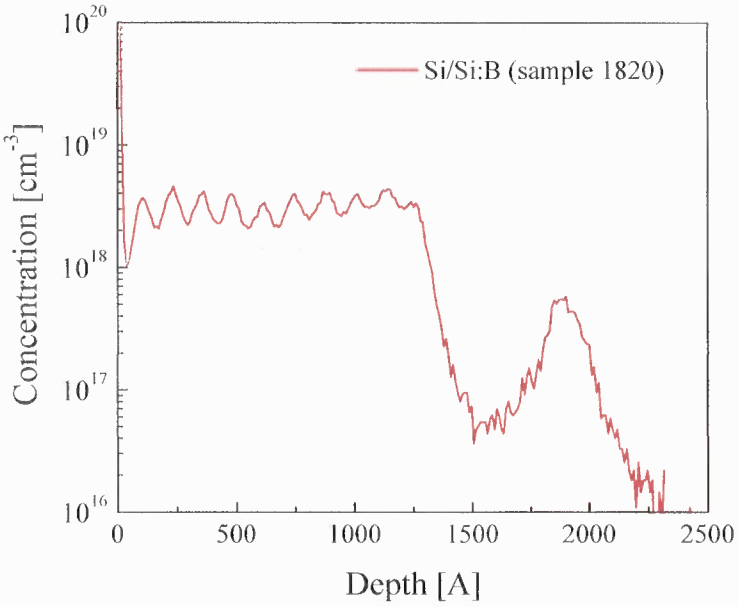

Figure 4.1 Doping concentration profile of a delta-doped multilayer sample ($t_{Si:B}$=2.5 nm, t_{Si}=10 nm and N_A=5·10^{18} cm^{-3}), measured by secondary ion mass spectrometry (SIMS).

4.1.1 Raman Spectroscopy

Figure 4.2 compares Raman spectra in Si/Si:B delta-doped multilayers and in a moderately phosphorus-doped (P-doped) c-Si. The Si transverse optical (TO) phonon peak should be a Lorenzian peak centered at exactly 520 cm^{-1} with full width of half maximum (FWHM) ~3.5 cm^{-1}. Since the overall Si/Si:B multilayer sample thickness varies from ~110 to 425 nm, which is less than penetration depth of the probing laser, it is concluded that the Raman signal at ~520 cm^{-1} is originated from scattering within the c-Si substrate as well as the Si separating layers. Figure 4.2(a) compares the Raman peaks near 520 cm^{-1} from samples with different doping concentrations and delta-doped layer thicknesses. When compared to c-Si, despite the high doping concentrations in the multilayers (up to 5·10^{18} cm^{-3}), very slight shift (~0.15 cm^{-1}) and broadening (~1 cm^{-1} in FWHM) of the peaks can be found. Shifts and broadenings of Raman features are indications of strain in the samples. Figure

4.2(b) shows the Si main peak and the weaker Raman features at higher frequencies. A Lorezian curve simulating an ideal Si TO peak (located at 520 cm^{-1} with FWHM of ~3.5 cm^{-1}) with same maximum value as the sample spectrum is shown to demonstrate the amount of peak shift and broadening. The Raman spectra show low, yet noticeable strain.

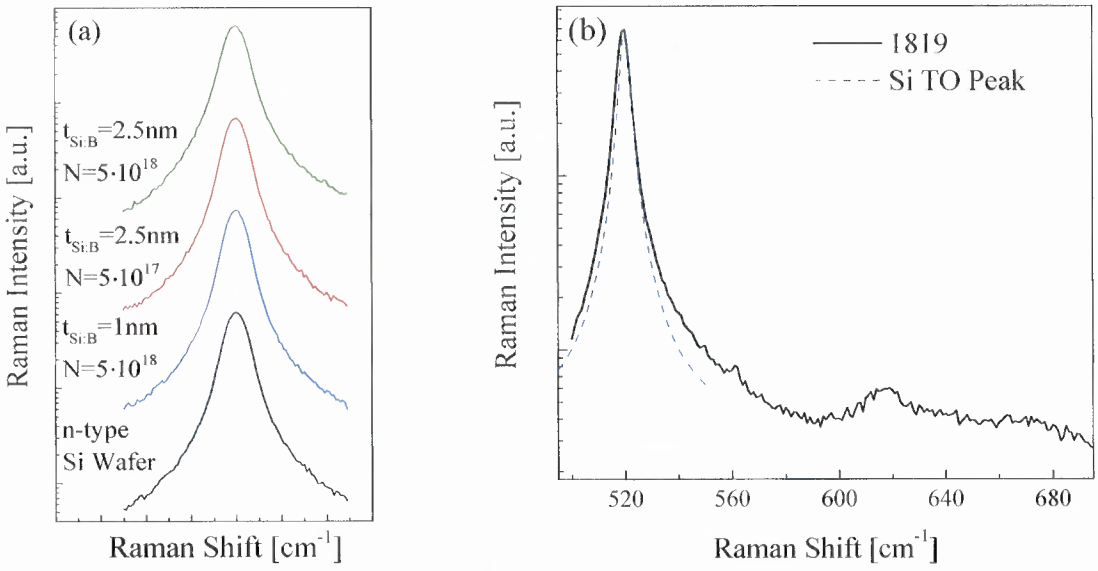

Figure 4.2 Raman spectra of Si/Si:B multilayer structures: (a) Si transverse optical (TO) peak in the vicinity of 520 cm^{-1} measured in the delta-doped samples with different doping concentrations and Si:B layer thicknesses (as marked) with a comparison of c-Si. The spectra are shifted vertically for clarity. (b) A delta-doped sample with a high B concentration (N_A=5·10^{18} cm^{-3}) extended toward higher wavenumbers. An ideal c-Si Raman TO peak at 520 cm^{-1} with full width of half maximum (FWHM) of 3.5 cm^{-1} is shown to demonstrate the peak shift and broadening. Note vertical logarithmic scale on both figures.

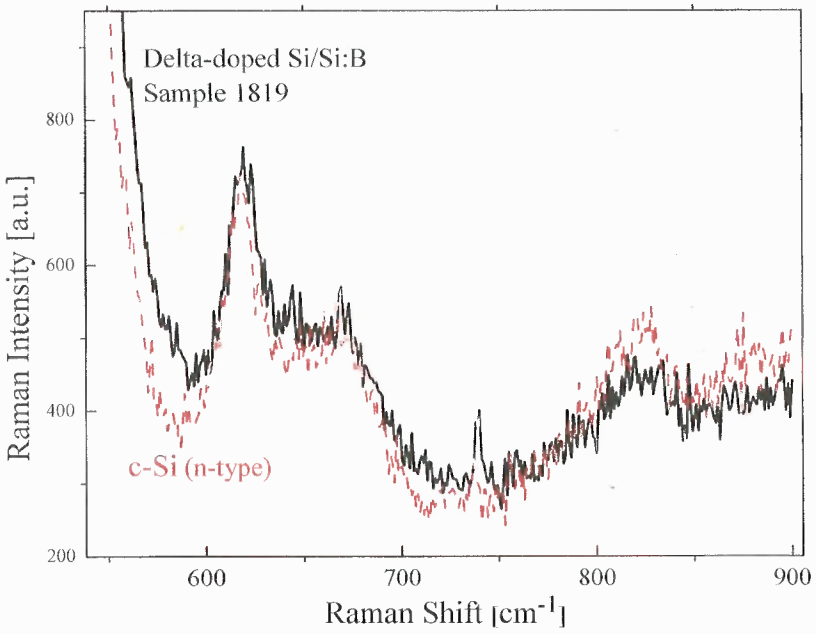

Figure 4.3 Comparison of Raman spectra in a delta-doped multilayer sample with B concentration, $N_A=5\cdot10^{18}$ cm^{-3} and moderately doped n-type c-Si at wavenumbers corresponding to Si-B local vibration modes.

Previous publications [115, 116] suggested the Raman features in the frequency region around 600-680 cm^{-1} are associated with Si-B vibration modes (~620 cm^{-1} for ^{11}B and ~640 cm^{-1} for ^{10}B) [117]. Detailed Raman spectra are performed on several samples in this region and compared to that of the n-type (P-doped) Si control sample (Figure 4.3). Note that the two spectra are normalized to c-Si (520 cm^{-1}) intensity. Although two distinct Raman peaks are found around 600-680 cm^{-1} in the delta-doped samples, the same features with same intensities can also be found in the Si control sample. It is thought that the peaks are more likely multi-phonon Raman features with TO and transverse acoustical (TA) phonons (TO(X)+TA(X)) combinations rather than $Si\text{-}B^{10}$ or $Si\text{-}B^{11}$ vibrations [100, 118]. From these results, it is concluded that despite the high doping concentrations, there is no evidence of dopant segregation in the delta-doped multilayers.

Anti-Stokes spectra are also measured. The relative intensities of Stokes and anti-Stokes TO peaks (Figure 4.4) are used to calculate sample temperatures using Equation (2.3). The results show that the thermal conductivities in Si:B layers are similar to that of c-Si.

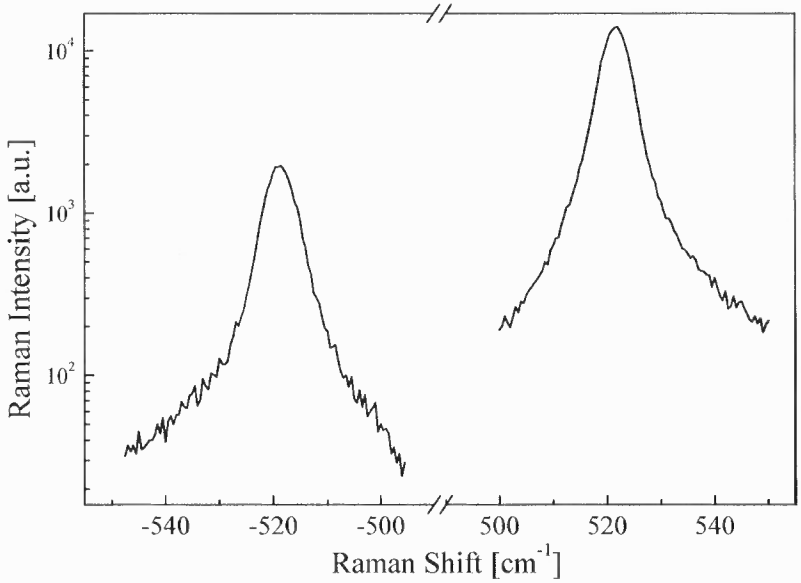

Figure 4.4 Relative intensities of Stokes and anti-Stokes Si optical phonon peaks of sample 1819 (N_A=5·10^{18} cm^{-3}). Note vertical logarithmic scale.

4.1.2 Photoluminescence

Figure 4.5 shows the PL spectra of a heavily delta-doped sample and the c-Si control sample, recorded at low temperature (10 K) with liquid-nitrogen-cooled diode array. Similar to c-Si, the delta-doped multilayers have sharp and well defined PL peak with characteristic Si phonon energies, such as TO, TA and no-phonon (NP) transitions. The slight shift and broadening of these PL features, particularly the Si TO peak at ~1.10 eV and the TA peak at ~1.14 eV, confirms the Raman spectroscopy findings of strain in the Si/Si:B multilayers. The shifts and broadenings of the peaks are more apparent in PL

because PL is more sensitive to strain than Raman spectroscopy. The PL features below 1.09 eV, though stronger in delta-doped multilayers, still exhibit the same characteristic peaks at ~1.03 and ~1.07 eV, which are from the combination of two TO phonons (2TO), or of a TO phonon and a phonon selected from intervalley scattering of two electrons (TO+IV) [119]. The <1.09 eV PL signals are believed to be from the B delta-doped layers, and the increased broad background intensity is the result of dopant-induced strain in the disturbed Si lattice.

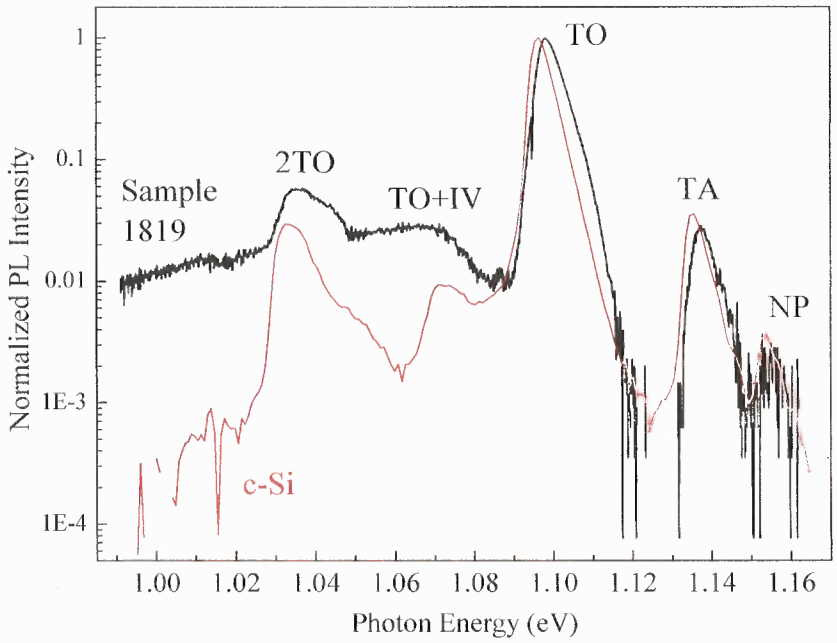

Figure 4.5 Normalized low-temperature (10 K) photoluminescence (PL) spectra of c-Si and Si/Si:B (sample 1819, $N_A=5\cdot10^{18}$ cm^{-3}) with characteristic phonon modes as marked. Note vertical logarithmic scale.

Figure 4.6 shows the normalized spectra of the PL temperature dependence in the range of 17 to 100 K. The PL spectra also exhibit temperature dependence similar to that in c-Si with broadening and decrease of peak intensity as temperature increases. The room

temperature PL spectra of several samples are shown in Figure 4.7. There is a correlation between the PL intensities and the B-doped layer concentrations. However, the highest PL intensity at room temperature is found in the undoped Si control sample. Contrary to previously reported data [11], the delta-doped multilayers exhibit no room temperature PL enhancement when compared to the room temperature PL of undoped c-Si.

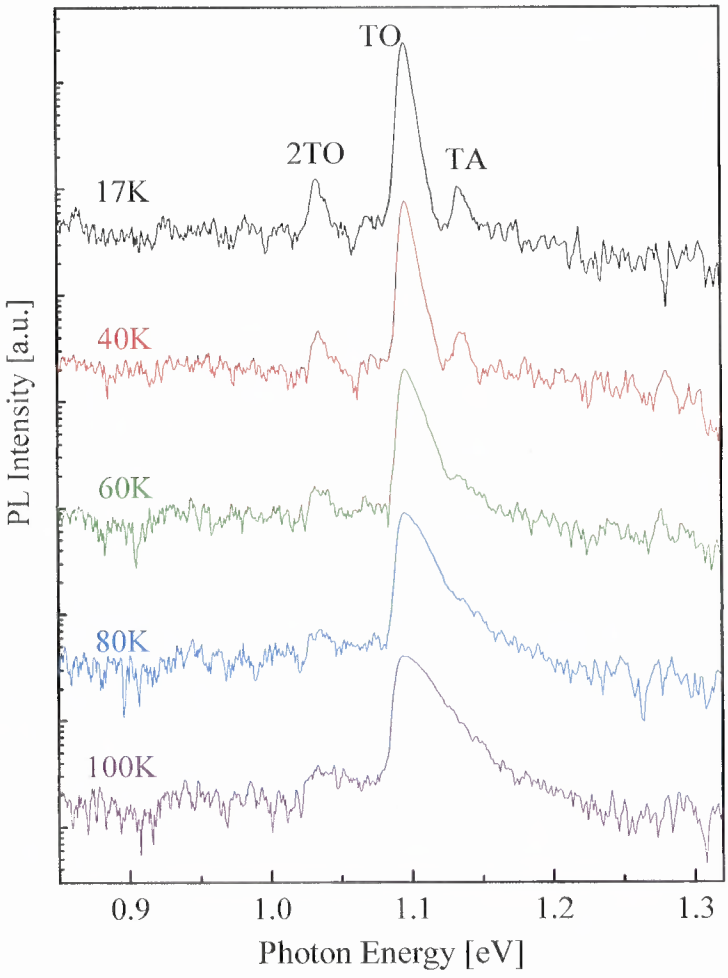

Figure 4.6 Temperature dependence of PL with the temperature and phonon modes as marked. Note that the vertical axis is in logarithmic scale, and the spectra are normalized and offset for clarity.

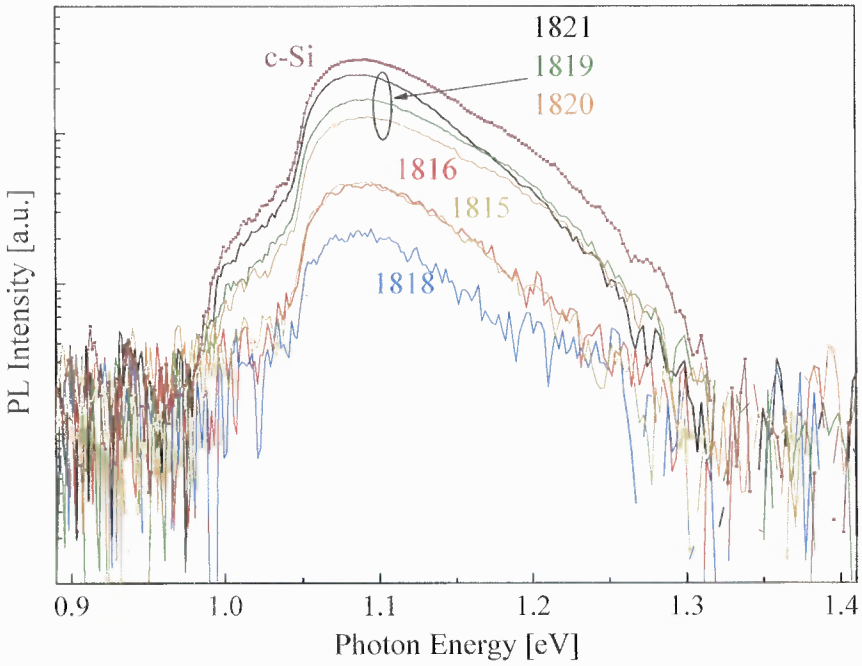

Figure 4.7 Room temperature PL spectra of Si/Si:B multilayers and a c-Si control sample collected under identical conditions. Note vertical logarithmic scale.

In several samples, at rare areas, strong PL can be found at photon energies significantly below the c-Si bandgap, in the region of 0.77 to 0.9 eV. Figure 4.8 shows details of such PL under different excitation conditions. Note that the spectra are normalized to the Si TO peak intensity and the rapid signal decrease below 0.76 eV is due to the detector cut-off. The positions of at least two broad PL peaks can be assigned to the Si defect-related luminescence lines [120]. The PL intensity increases as the excitation wavelength and the penetration depth increases, indicating that the defects are not within the delta-doped multilayers (which have total thickness of ~110 to 425 nm) but rather from the substrate immediately underneath the multilayers and the Si buffering layer.

The defects are presumed to be a result of imperfect surface conditions prior to fabrication of the samples, most likely imperfections or contaminations on the wafer before the buffer layer is deposited.

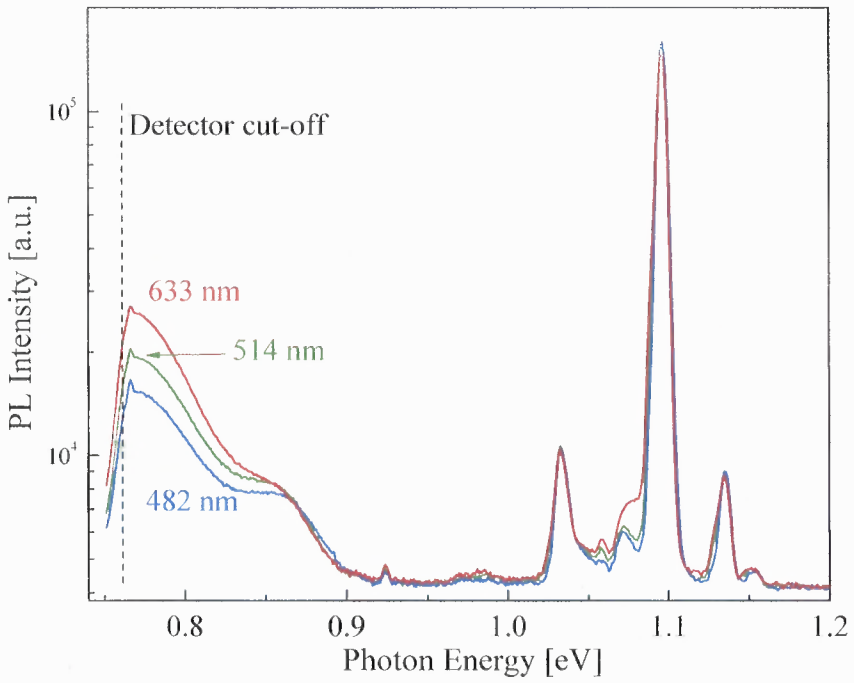

Figure 4.8 Low temperature PL spectra collected using different (indicated) excitation wavelengths, showing a broad PL band at 0.77-0.9 eV. Note that the spectra are normalized to Si TO peak intensity, and the vertical axis is in logarithmic scale.

4.1.3 Reflectance, Electrical Properties and Electro-reflectance

The observed temperature dependence of optical reflectivity near the Si bandgap is shown in Figure 4.9. The results indicate a relatively high reflectivity at room temperature in the energy range of 0.8-1.3 eV. As the temperature decreases from 300 to 200 K, a rapid decrease in reflectivity is observed, most likely due to carrier freeze-out. At temperatures

≤100 K, the reflectivity is nearly constant. This result indicates a possible metal-insulator transition in delta-doped multilayers. It is quite unusual because a carrier freeze-out in moderately doped Si normally occurs at a lower temperature, near 50-60 K [39].

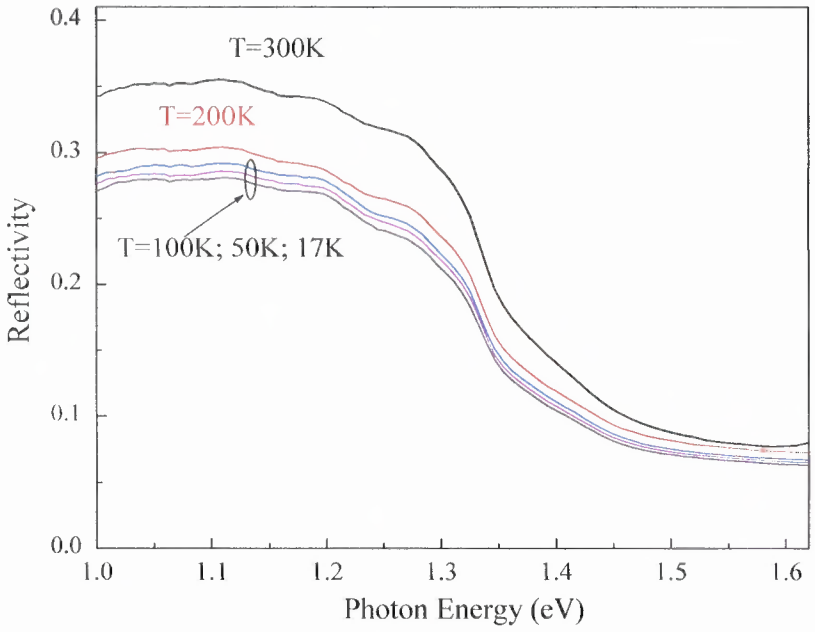

Figure 4.9 Optical reflectivity at different temperatures (as marked) in sample 1816 (N_A=1·10^{18} cm^{-3}).

The current-voltage (I-V) and capacitance-voltage (C-V) measurements show Schottky-barrier-like characteristics (Figure 4.10), which suggest that the applied electric field impels the mobile carriers in the delta-doped layers to the edges to form metal-like thin layers. This result shows the possibility of controlling the interface properties by applying electric fields across the multilayers. Time-resolved measurements of electro-reflectance modulated by square pulses are performed and the result of +1.6 V at 100 kHz modulation is shown in Figure 4.11. Increases in the optical reflectance can be found when electrical pulses are applied, which further confirms the gathering of charges at

the delta-doped layer edges as a result of applied electrical field. The ability to vary optical reflectance and create metal-like high reflectance layers indicates the possibility of designing electrically controllable mirrors. This feature can be especially useful in the optical switches or routers, replacing the traditional microelectromechanical systems (MEMS) mirrors with the advantages of simpler fabrication process, more compact dimensions and faster reaction time.

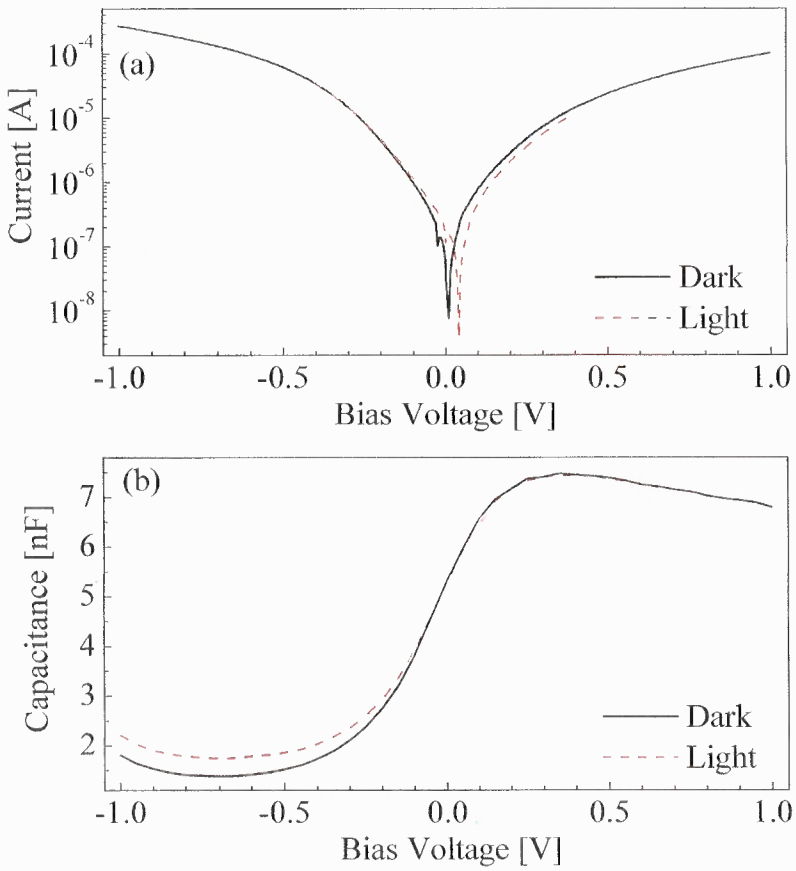

Figure 4.10 Current-voltage (I-V) and capacitance-voltage (C-V) characteristics in the dark and under Ar^+ laser illumination.

The optical characterizations revealed low strain and no dopant segregation from the B delta-doped multilayers. Delta-doping with Si separating layers is proven to be an effective way to achieve high localized doping concentrations without creating significant dopant-induced strain or dopant segregation by maintaining moderate overall average doping concentrations. Relative intensities of Stokes and anti-Stokes Raman signal showed no change in thermal conductivity from heavy doping or the multilayer structure. Temperature varying reflectance, I-V and C-V characteristics, and pulse-modulated electro-reflectance measurements demonstrate electrically controllable reflectivity. These results show that the molecular beam epitaxy (MBE) multilayer delta-doped structures can achieve the same performance goals as highly doped bulk materials without the risk of strain or dopant segregation and have promising potentials as electrically controllable mirror in high speed, sub-micron CMOS applications.

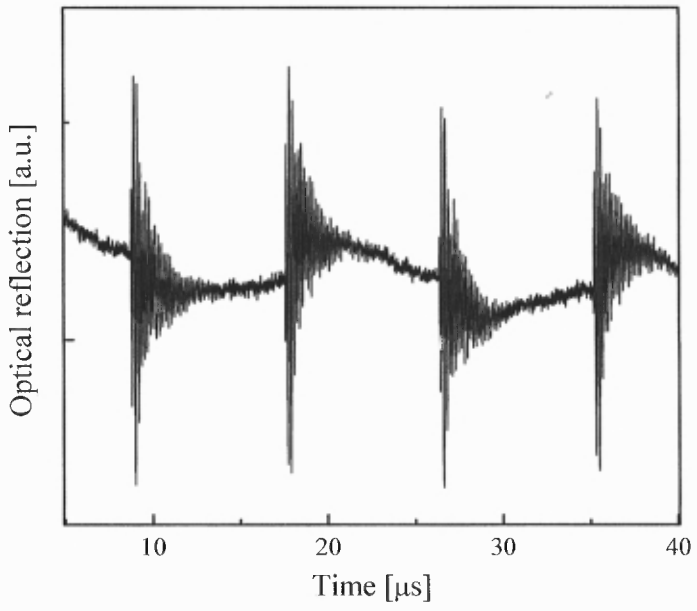

Figure 4.11 Time-resolved electro-reflectance modulated by square pulses of +1.6 V and frequency of 100 kHz.

4.2 Si/SiGe Multilayers

The sample details of the two-dimensional (2D) and three-dimentional (3D) $Si/Si_{1-x}Ge_x$ multilayers, including nominal physical parameters and growth temperatures are presented in Table 4.2. The samples' physical structures are examined by cross-sectional transmission electron microscopy (TEM) and shown in Figure 4.12. Special attention is given to Sample 1810 (Figure 4.12(a)), which has developed as 2D planar multilayers with uncommonly high Ge content. The 2D morphology is achieved by carefully monitoring the growth conditions, in particular, the growth temperature, which has to be high enough to prevent the formation of defects and maintain epitaxial growth, and yet low enough to prevent Stranski-Krastanov (S-K) mode. The TEM data (Figures 4.12 and 4.13) reveal good epitaxial structures, and the observed slight waviness at the layer boundaries indicates strain-induced interdiffusion between Si and SiGe layers.

Table 4.2 Details on Sample Fabrication of $Si/Si_{1-x}Ge_x$ Multilayers

Sample #	Morphology	x	$t_{Si/Ge}$ [nm]	t_{Si} [nm]
1810	2D planar	0.518	3.9	13.5
1814	3D cluster	0.53	3.5	14.9
1830	3D cluster	0.6	3.3	11.4
1834	3D cluster	0.6	3.0	14.0

Note: $t_{Si/Ge}$ – SiGe layer thickness, t_{Si} – Si separating layer thickness, x – nominal Ge content.

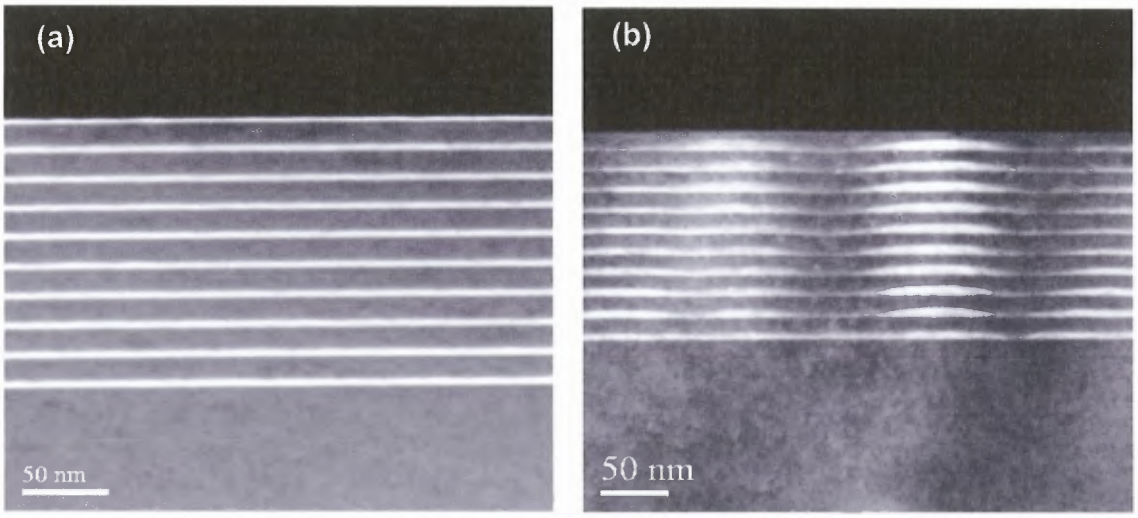

Figure 4.12 Cross-sectional transmission electron microscopy (TEM) images of (a) two-dimensional (2D) Si/SiGe multilayers (sample 1810) and (b) three-dimensional (3D) vertically self-aligned Si/SiGe nanoclusters (sample 1831).

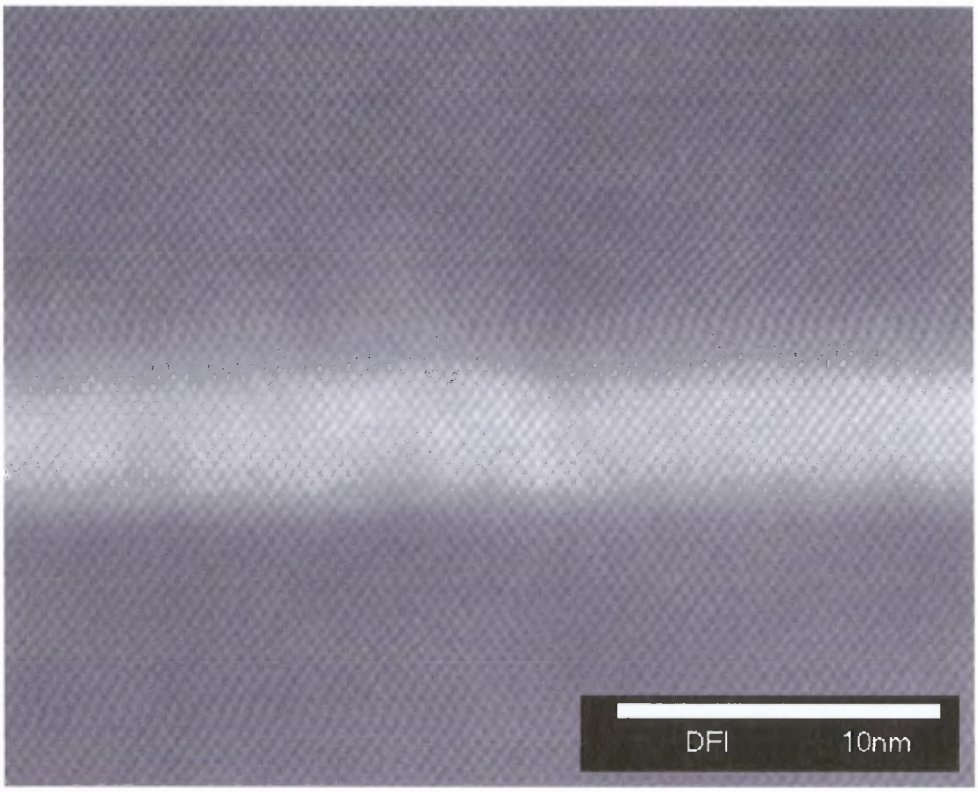

Figure 4.13 Cross-sectional, high-resolution TEM (HR-TEM) focusing on the second from the top layer of the 2D Si/SiGe multilayers.

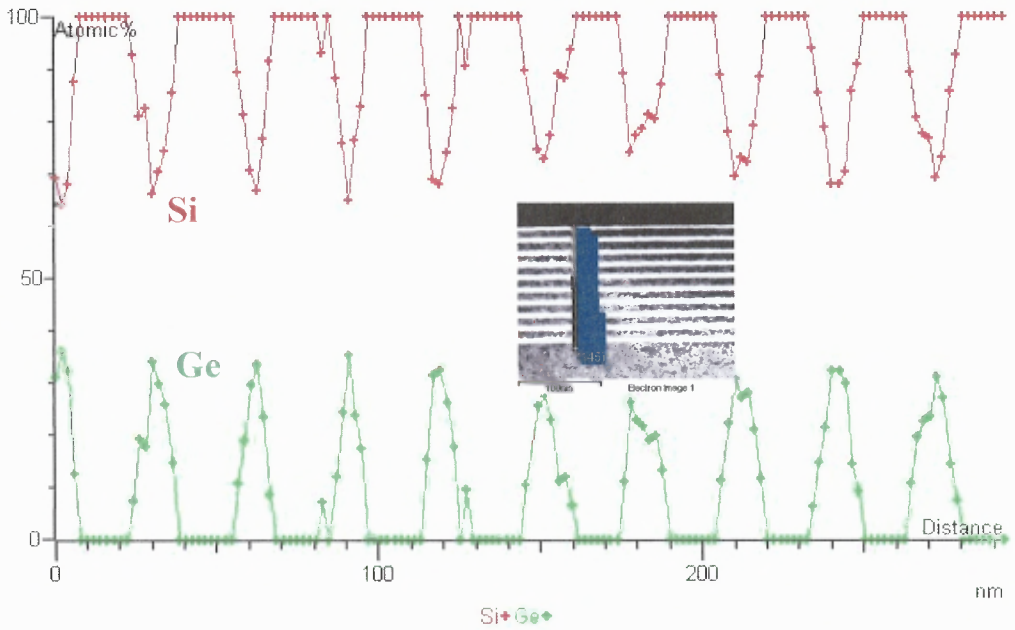

Figure 4.14 Energy-dispersive x-ray spectroscopy (EDX) composition analysis of the 2D Si/SiGe multilayers with the inset shows the schematics of the measured area.

The multilayer chemical compositions are also examined using energy-dispersive x-ray spectroscopy (EDX) (Figure 4.14). The nominal Ge content (from MBE growth parameters) is shown in green line for comparison, and the inset TEM image shows the direction in which the analysis is done. The layer centers have relatively higher Ge content compare to usual epitaxial Si/SiGe superlattices, and evidence of diffusion can be seen at the interfaces, confirming the findings of analytical TEM.

The 3D SiGe multilayers have 3-10 nm high, initially nearly pyramidal-shaped clusters. The thin Si separating layers allow the strain field to propagate in the growth direction and induce different degree of vertical self-organization. A cross-sectional TEM image of the self-organized cluster is shown in Figure 4.12 (b). Cross-sectional chemical composition analysis along the cluster column and the valleys between the clusters are

shown in Figure 4.15 [14]. The nominal Ge content from the MBE growth parameters is also shown for comparison. Detailed structural studies find the clusters have Ge-rich centers, with composition up to 50%. The Si around the top of the clusters is under tensile strain while the Si in the valleys between the clusters is under compressive strain [14, 121, 122].

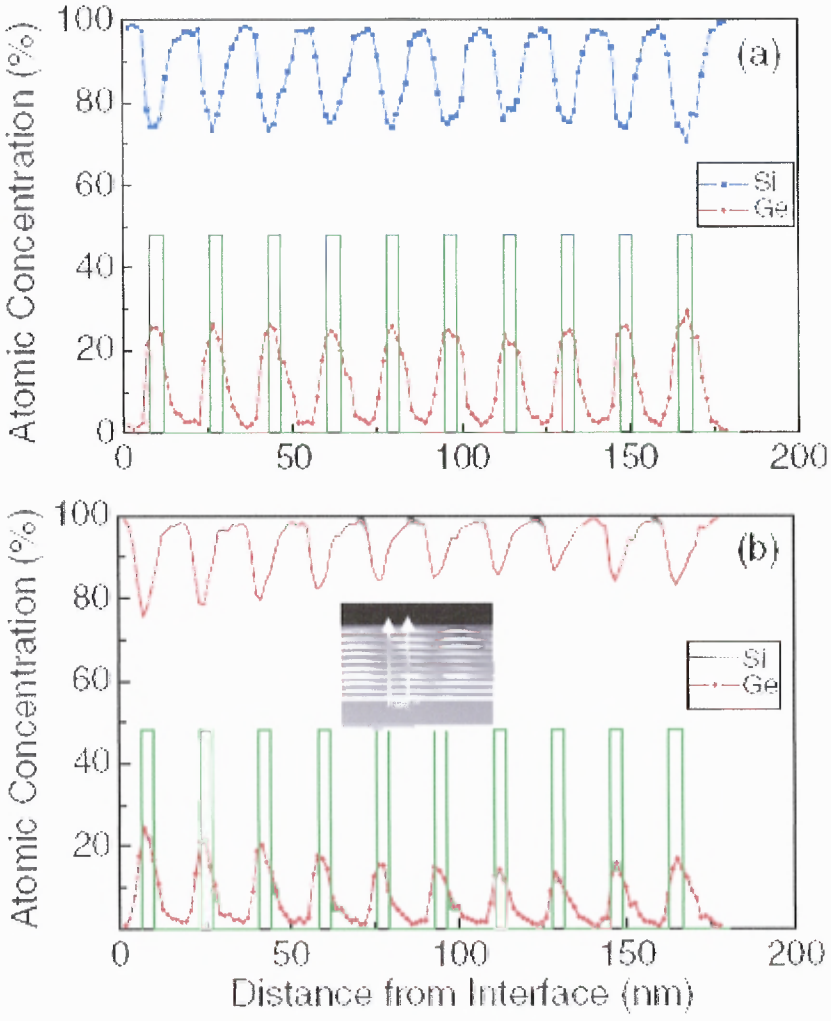

Figure 4.15 EDX chemical composition profiles in the growth direction for a Si/SiGe 3D cluster multilayers. The measurement is performed (a) along the center of the clusters and (b) in the valleys between the clusters, as shown in the micrograph in the inset. Also indicated on the graph is the nominal Ge concentration profile based on the growth parameters [14].

4.2.1 Raman Spectroscopy

Figure 4.16 compares the result of Raman spectroscopy using different excitation wavelengths. Note the spectra are shifted for clarity. In Si/SiGe nanostructures, the Raman spectra have three major vibrational modes known as the Si-Si vibration (at ~520 cm^{-1}), the Si-Ge vibration (at ~400 cm^{-1}) and the Ge-Ge vibration (at ~300 cm^{-1}). Note that, under excitation with λ=514.5 nm, the ratio of the Raman peak intensity associated with Si-Si vibration to the Si-Ge or Ge-Ge Raman peaks is much higher than that of under a shorter wavelength excitation, which indicates that under a longer wavelength excitation with deeper penetration depth, the Raman signal at ~520 cm^{-1} has a stronger contribution from the crystalline Si substrate. Figure 4.17 shows a closer look of the Si-Si vibration by comparing normalized Stokes and anti-Stokes Raman spectra in the vicinity of 500 cm^{-1}. Besides the main peak associated with the Si-Si vibration mode at ~±520 cm^{-1}, an additional Raman feature at ~±505 cm^{-1}, which corresponds to the Si-Si vibration in the presence of a Ge atom and/or associated with strained Si sandwiched between SiGe cluster multilayers [85-90] can be clearly seen, especially when using the shorter wavelength (Figure 4.17(a)).

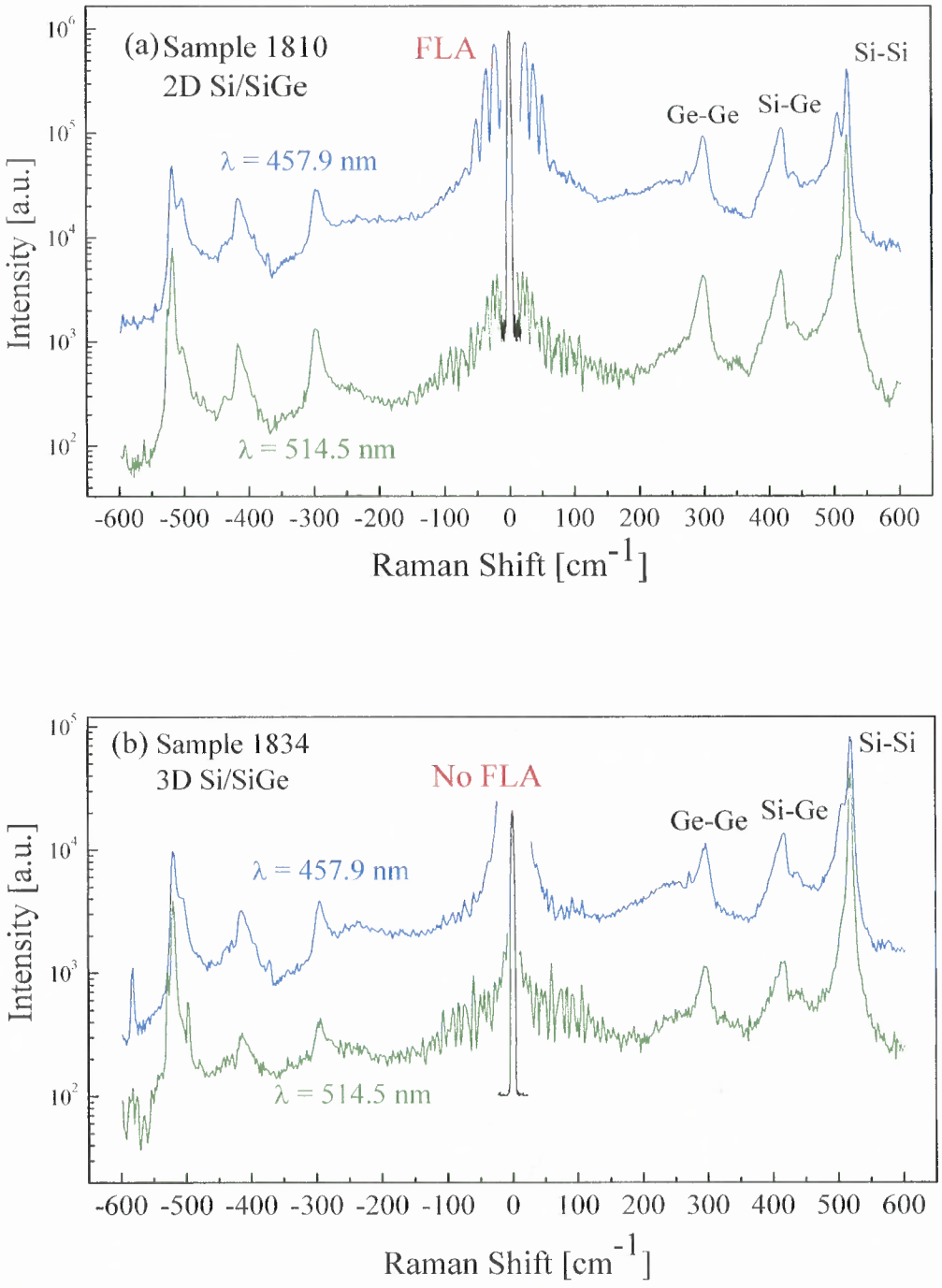

Figure 4.16 Stokes and anti-Stakes Raman spectrum of (a) sample 1810 with high intensity folded longitudinal acoustic (FLA) phonon signals and (b) sample 1834 (no FLA phonon signal), each with two different excitation wavelengths, and the three-mode local vibrations of Si-Si, Si-Ge and Ge-Ge are as marked. Note the spectra are shifted for clarity and the vertical axes are in logarithmic scale.

In a sample without a temperature gradient, these normalized Stokes/anti-Stokes Raman lines should be identical. In Figure 4.17(b) (with longer wavelength), the Stokes and anti-Stokes Raman signals at ~±520 cm^{-1} are similar to each other, are symmetrical and have a FWHM of ≤5 cm^{-1}. The narrow peak indicates the signal is originated from c-Si; presumably, most of the ~±520 cm^{-1} signal in this spectra is collected from the substrate, which corroborates the finding in Figure 4.16. However, the small difference between Stokes and anti-Stokes signals around ±505 is cm^{-1} should not be overlooked. The increase in anti-Stokes Raman signal around -505 cm^{-1} indicates that under laser excitation, the sample surface temperature (associated with the Si/SiGe multilayers) is higher than the Si substrate temperature.

In Figure 4.17(a), when using 457.9 nm excitation wavelength with shallower penetration depth of ~100 nm, the signals are collected only from the Si/SiGe nanostructure and the difference in the Stokes and anti-Stokes Si-Si peaks (around ±520 cm^{-1}) is much more pronounced as the peaks asymmetrically broadened. In addition, the Raman feature around ±505 cm^{-1} has even more noticeable asymmetrical broadening with FWHM of 14 and 21 cm^{-1} for Stokes and anti-Stokes, respectively. The large difference between the intensity ratio of the Stokes and anti-Stokes peaks indicates a large temperature gradient between strained Si and c-Si. Since the entire laser excitation energy is absorbed in the nanostructure, the temperature gradient, in this case, exist not between the nanostructure and the substrate but wholly within the nanostructure, as differences in c-Si separating layers and the strained Si in the SiGe layers.

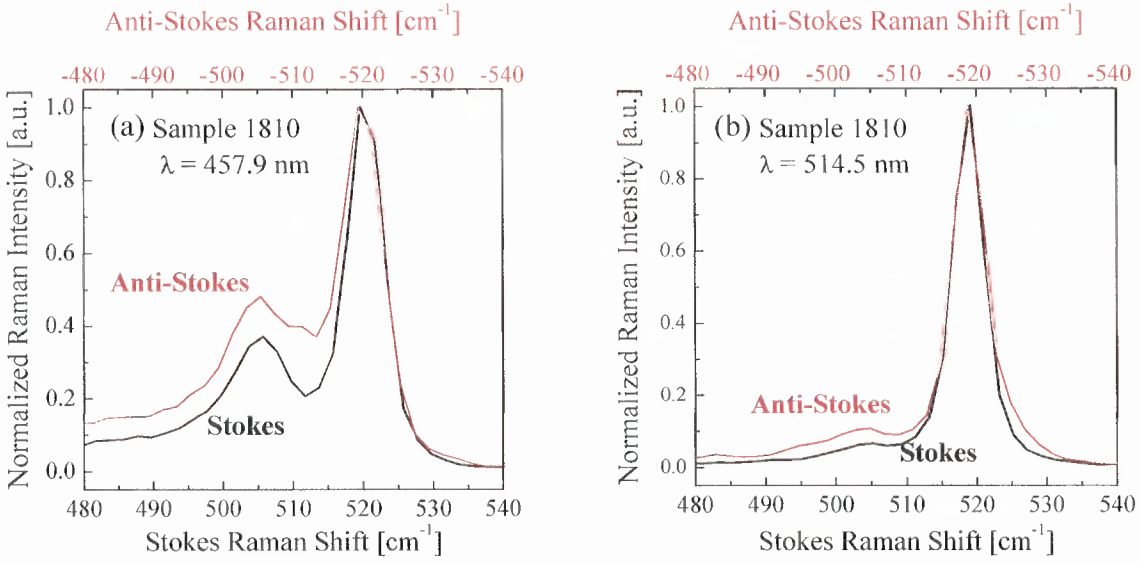

Figure 4.17 Normalized Stokes and anti-Stokes Raman peaks in the vicinity of Si-Si Raman mode with excitation wavelength of (a) 457.9 nm and (b) 514.5 nm, showing relative enhancement of the Raman feature at ~505 cm^{-1}. The differences presumably are due to higher temperatures in (a) the SiGe layers than the separating layers and (b) the Si/SiGe multilayers than the substrate.

Raman scattering with a laser source whose wavevector is close to the center of the Brillouin zone (BZ), detects the aforementioned distinct, strong optical phonon signals from Raman scattering and much weaker acoustic phonon signals from Brillouin scattering at lower frequencies [98, 123-125]. In structures that form Brillouin minizone (BMZ), acoustic phonon folding can be detected in Raman Spectroscopy as folded longitudinal acoustic (FLA) phonon doublets (for details on zone folding and BMZ, see subsection 2.2.5). In Figure 4.16(a) prominent FLA signals can be seen in the region closer to BZ center (|Raman shift| < 100 cm^{-1}). The intensity of the FLA phonon Raman peaks increases and more characteristic doublets can be resolved as the excitation wavelength decreases from 514.5 to 457.9 nm. Figure 4.18 is a detailed spectrum showering the FLA in sample

1810 (2D) with the peak positions marked and used to reconstruct the BMZ in the inset [125, 126]. The positions of the estimated Brillouin scattering peak is also shown in Figure 4.18, marked as m_0.

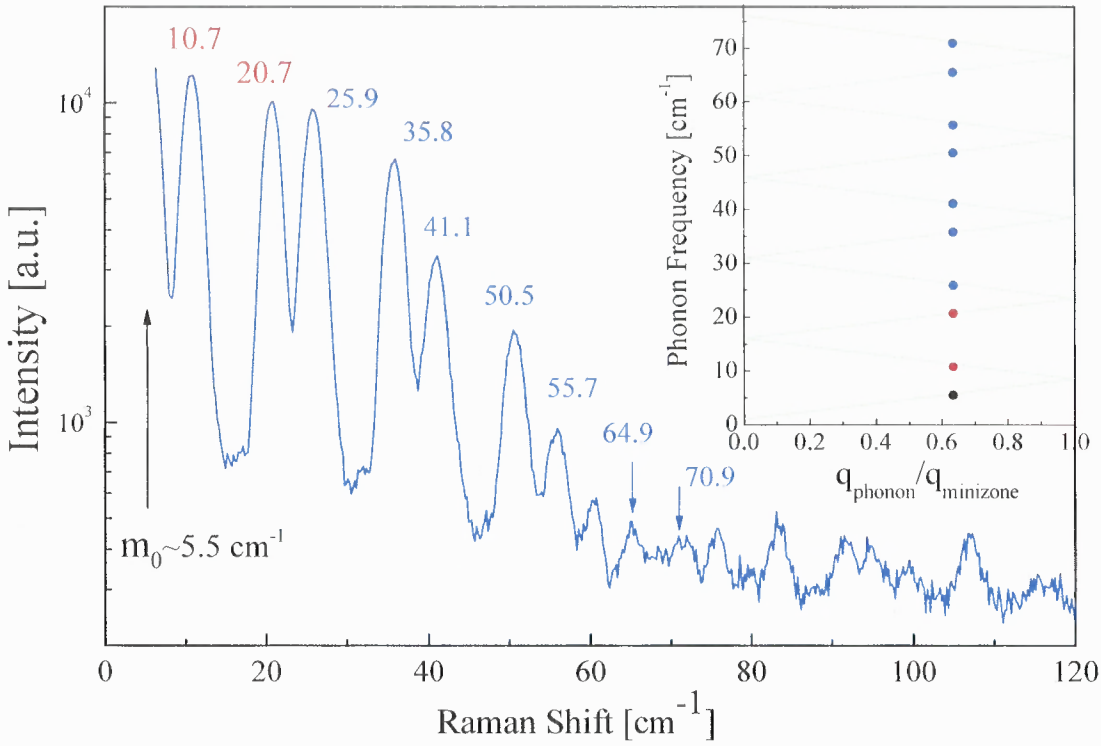

Figure 4.18 Characteristic doublets of FLA close to the Brillouin zone center (2D multilayers). Note the vertical logarithmic scale. The reconstruction of Brillouin minizone (BMZ) is shown in the inset.

The low-frequency Raman spectra differentiate the Si/SiGe multilayer samples into two groups: those with FLA and those without FLA. This difference may be explained by $Si_{1-x}Ge_x$ layer composition and quality of the multilayer interfaces. In samples with slightly lower Ge content (1810 and 1814), more abrupt Si/SiGe interfaces and presumably better superlattice (SL) structures, high intensity FLA signals are revealed with half a dozen of

the characteristic doublets (Figure 4.16(a) and Figure 4.18). The highest FLA intensity is found in the 2D $Si/Si_{1-x}Ge_x$ multilayers with Ge concentration approaching x=0.4 (which is much higher compared to conventional Si/SiGe SLs with Ge concentration x~0.1-0.2). It is believed that the quasi-planar structure is a key factor in forming BMZ. On the other hand, no FLA signal is detected in samples with higher Ge content (1831 and 1834, Figure 4.16(b)). The 4.2% lattice mismatch between Si and Ge induces strain and more interdiffused interfaces. Such strain presumably shapes the multilayers into wavy SL structures, which does not form BMZ. Our measurements show that the BMZ formation and the FLA intensity are not only sensitive to multilayer morphology (SiGe planar alloy or SiGe clusters) but also to interface quality, and can be a useful, quick detection tool in characterizing Si/SiGe nanostructures.

4.2.2 Raman-based Nano-thermometry and Thermal Conductivity Calculations

Using Equation 2.3 and the Raman Stokes and anti-Stokes peak intensity ratio of Si-Ge vibrations, the surface temperature can be found. The Si-Si vibration peak intensity ratio can be used to find either the temperature of the substrate immediately underneath the nanostructure (under 514.5 nm excitation) or separating layers (under 457.9 nm excitation). These calculated temperatures are listed in Table 4.3. The Si substrate has temperature close to the temperatures measured on the back of the sample with a thermal-couple thermometer and the ambient temperature in the laboratory. Comparing the FLA formation and intensity to the temperature measurements, a clear correlation can be seen: in sample with high intensity FLA signals, the temperature gradient between Si-Ge and Si-Si modes is nearly half of that in samples without FLA. Since thermal conductivity is inversely

proportional to the temperature gradient (see Equation 2.3), the thermal conductivity is almost reduced to half when compare the 3D Si/SiGe nanoclusters multilayers to the 2D Si/SiGe planar multilayers.

Table 4.3 Summary of Temperature Measurements by Raman-based Nano-thermometry with Two Different Wavelengths, and the Correlation Between FLA Intensities and Temperature Gradients

Sample	x (nominal)	FLA	Temperature [K]					
			λ=457.9 nm Power ~100 mW			λ=514.5 nm Power ~400 mW		
			Si-Ge	Si-Si	ΔT	Si-Ge	Si-Si	ΔT
1810 (2D)	**0.52**	**High**	**~380**	**~350**	**30**	**~370**	**~300**	**70**
1814 (3D)	0.53	**Lower**	~440	~380	60	~420	~315	105
1831 (3D)	0.53	None	~440	~370	70	~460	~340	120
1834 (3D)	0.61	None	~410	~340	70	~450	~315	135

The difference in thermal conductivity is hypothesized to come from the zone folding and/or the multilayer structural properties. In samples with FLA, the zone folding provides additional acoustic phonon modes, which contribute to the prominent heat conducting mechanism in semiconductors – lattice conductivity. Presumably, the increased phonon modes increase the cross-plane thermal conductivity (heat conduction in the direction normal to the multilayers). Samples with strong FLA signal also have more abrupt, planar interfaces and less Si/SiGe interface scattering, and more homogeneous SiGe layers, both of which contribute to a better in-plane thermal conductivity (heat conduction in the direction parallel to the multilayers) [127]. In samples with wavy SL

structure, there is more Si/SiGe interface scattering from the strained and interdiffused wavy interfaces. Moreover, the cluster morphology with strain in and around the clusters and inhomogeneous Ge compositions (up to ~50 % Ge at the core) further reduces the thermal conductivity.

4.3 Si Nanowires

4.3.1 Photoluminescence

At low temperatures, the Au-catalyzed Si nanowires (NWs) have PL peaks close to the Si TO line around 1 eV (Figure 4.19). The peaks are not as well defined, significantly broadened and shifted toward lower energy, all of which is strong evidence of significant strain in the nanostructure. The PL temperature dependence is more sensitive in the Si NWs than in c-Si PL signals and can not be clearly detected above 40 K, presumably also due to the strain in the NWs. The PL spectra of the Ti-catalyzed Si NWs have very different characteristics (Figure 4.20). These spectra have weak or no ~1.1 eV PL signal that is associated with c-Si. Instead, a strong ≤1 eV PL signals (presumably associated with Ti-Si alloy or Titanium Silicides). Note that the rapid decrease of PL intensities below 0.78 eV is due to detector cut-off. The absence of ~1.1 eV PL signal could be a result of additional strain due to the even smaller Si NW diameters (≤50 nm).

4.3.2 Raman Spectroscopy

The Raman spectroscopy confirms the existence of significant strain in these NW samples. Figure 4.21 compares the normalized Raman spectra around 500 cm^{-1}. All three Si NW samples have c-Si peak around 520 cm^{-1}, indicating epitaxial growth and good crystalline structure inside the NWs. Besides the c-Si signals, there are significant signals from amorphous Si (a-Si) and strained Si in the region of 460-510 cm^{-1}. Comparing Raman and PL spectra, a correlation of the Raman stronger signal intensities in the region of 460-510 cm^{-1} and the decreased intensity or absence of the ~1.1 eV PL line is found. No Titanium Silicide ($TiSi_2$) Raman scattering (C49 or C54 phases) is detected in the 200-350 cm^{-1} region [128-130]. It is thought that the amount of $TiSi_2$ is so trivial that it can only be detected by the much more sensitive PL spectroscopy and not by Raman spectroscopy.

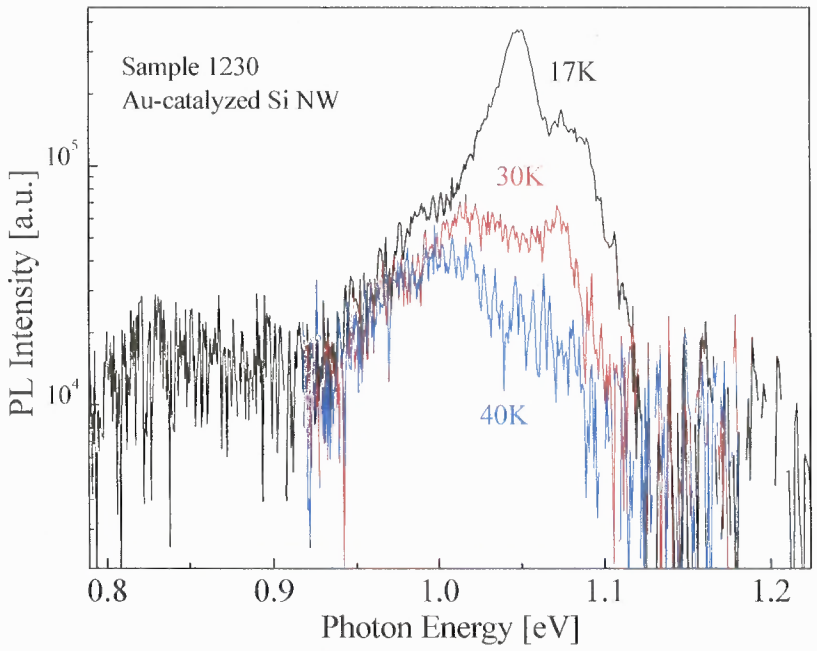

Figure 4.19 Low temperature and temperature dependent PL of Au-catalyzed Si nanowires (NWs).

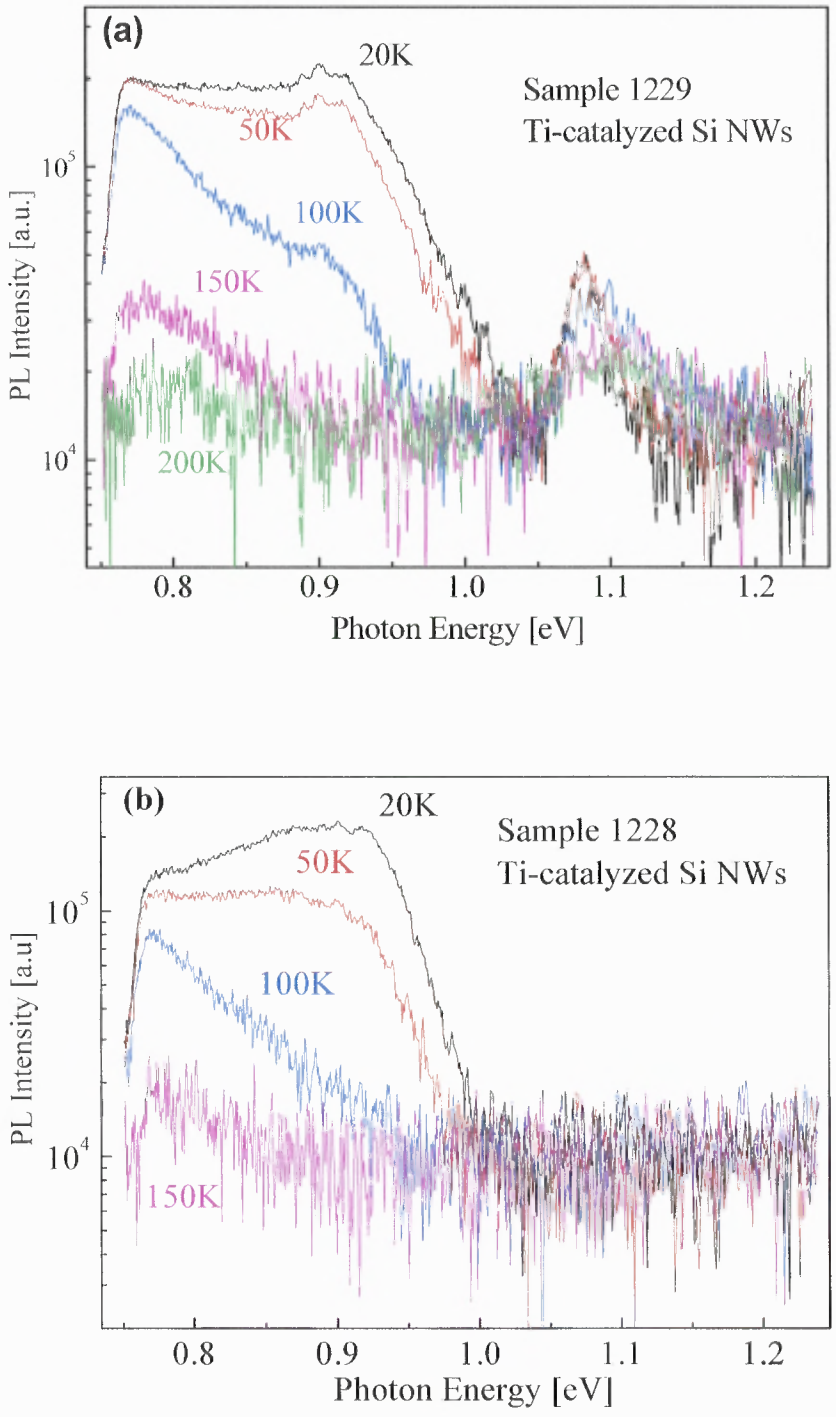

Figure 4.20 Low temperature and temperature dependent PL of two Ti-catalyzed Si NW samples with strong below bandgap PL: (a) significant strain causing weak ~1.1 eV peak and (b) even stronger strain resulting in no ~1.1 eV signal and strong below bandgap PL.

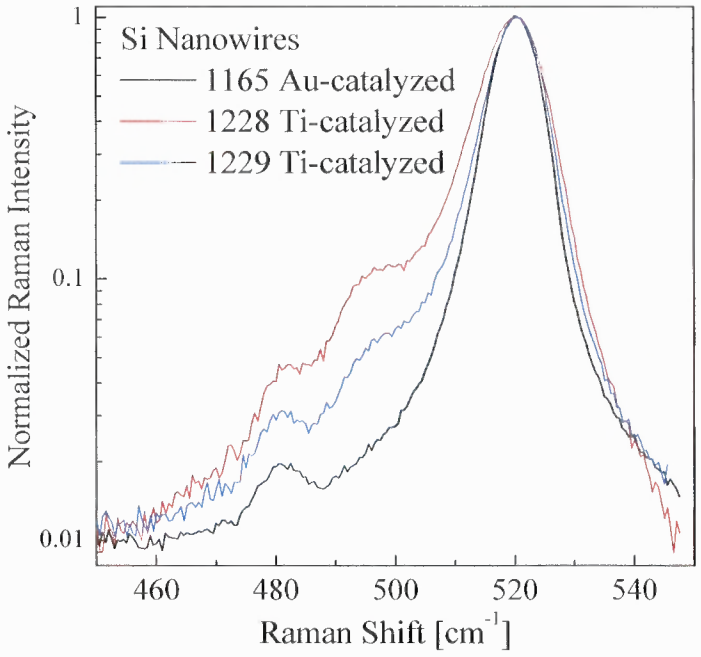

Figure 4.21 Normalized Raman spectra of Ti- and Au-catalyzed Si NW samples. Note the vertical logarithmic scale.

4.3.3 Raman-based Nano-thermometry and Thermal Conductivity Calculations

The surface temperatures of the Au-catalyzed Si NW sample, under 457.9 nm excitation with power intensities of 0.3-1.5 kW/cm^2 have been measured using Raman-based thermometry (calculated using the 520 cm^{-1} c-Si peak Stokes/anti-Stokes ratio), and sample backside temperatures and laboratory ambient temperatures have been measured using thermal-couple thermometer and the results are show in Figure 4.22(a). The overall system (Si NWs on Si carrier wafer) thermal conductivities are calculated using the method described in Section 3.3 and the results are plotted with respect to Raman surface temperature. The thermal conductivity results are comparable to measurements of Si NW with similar diameters (≤50 nm) found using microfabricated electrical heating and

sensing setup (Figure 2.14, from Ref. [80]). The calculated thermal conductivity does not include certain effects that would yield a even lower thermal conductivity, e.g., the power loss due to light scattering off the very rough NW sample surface and the heat loss due to the air (with very low thermal conductivity) around the NWs. Therefore, the actual thermal conductivity should be slightly lower than the calculated number shown in Figure 4.22. The low thermal conductivity in the Si NWs is believed to be dominated by phonon scattering (in the NWs with diameters smaller than phonon mean free path).

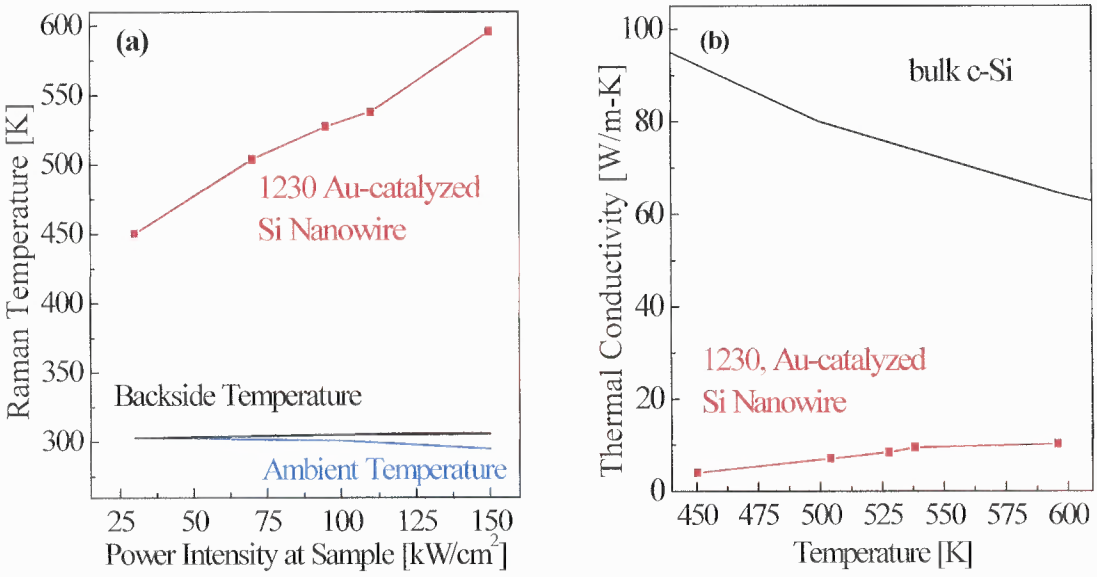

Figure 4.22 Raman-based thermometry in Au-catalyzed Si NWs: (a) calculated surface temperatures compared to backside and ambient temperatures (measured by a thermal-couple thermometer), and (b) estimated thermal conductivity compared to bulk c-Si.

4.4 Si/Ge Nanowire Heterojunctions

Figure 4.23 shows a scanning electron microscopy (SEM) image of the Si/Ge NW heterojunction (HJ) sample and a high resolution TEM (HR-TEM) micrograph of a single NW HJ. In both images, it is clearly visible that the HJ interface is very sharp with NW diameter expansion from Si to Ge, which is a result of the 4.2% lattice constant mismatch. However, the closer inspection by the HR-TEM reveals that the expansion of the NW diameters is not as abrupt as predicted (see Figure 2.9) but rather tapered over several tens of nanometers. It is believed that over this tapered expansion, Si lattice is under tensile strain while Ge lattice is under compressive strain. Figure 4.24 is a dark field TEM (DF-TEM) image showing lattice fringes in the (111) direction around the Si/Ge heterointerface. Note that the lattice fringe spacing does not directly reflect lattice constant but rather the distance between parallel planes in the same direction (hkl), as $d_{(hkl)} = a \times (h^2 + k^2 + l^2)^{-1/2}$, where a is the lattice constant. For unstrained Si and Ge (111) crystals, $d_{(111)}$ are 0.3136 and 0.3267 nm, respectively. The DF-TEM image shows lattice fringes exhibiting expansion in Si side of the HJ and compression in Ge side of the HJ, confirming that Si is under tensile strain and Ge is under compressive strain.

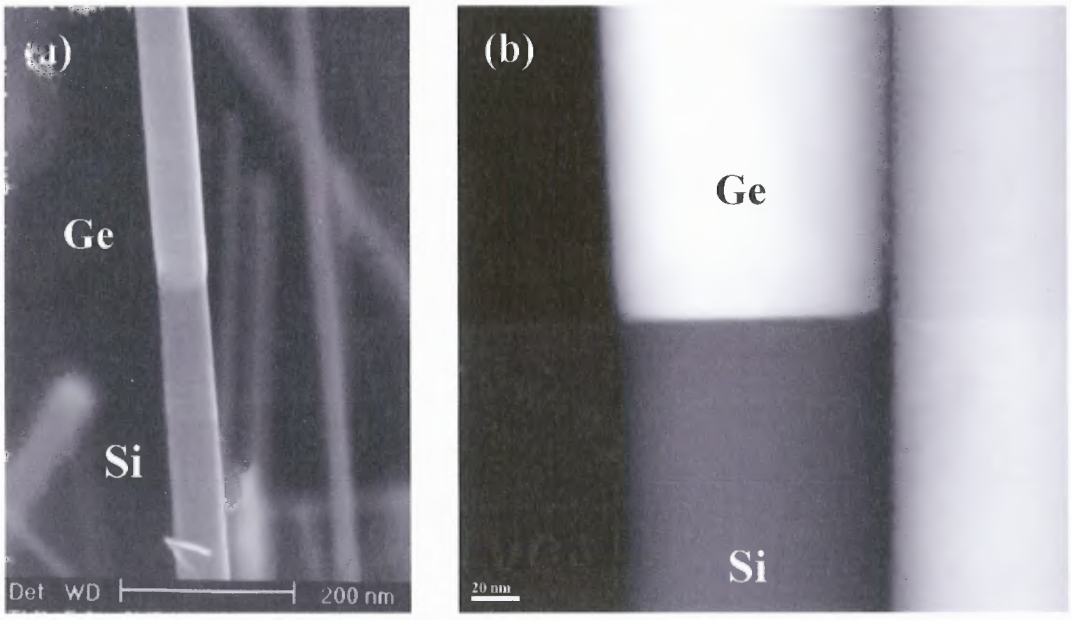

Figure 4.23 (a) Scanning electron microscopy (SEM) image of the Si/Ge NW heterojunction (HJ) sample with visible NW diameter expansion in the Ge part, and (b) HR-TEM image of a single NW HJ with visible sharp interface and tapered NW expansion.

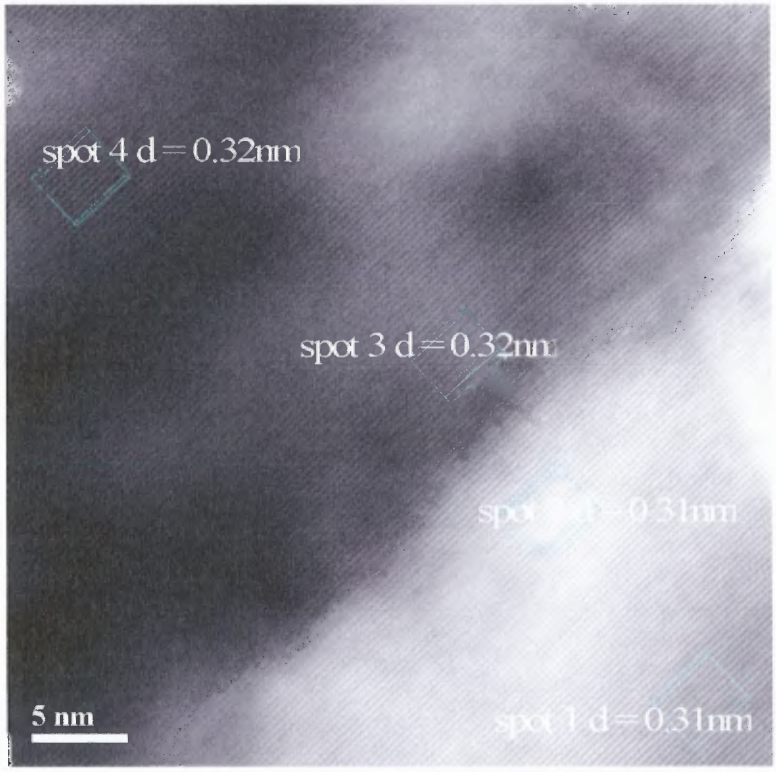

Figure 4.24 Lattice fringes image from high resolution, dark field TEM (DF-TEM) showing expansion of Si lattice and compression of Ge lattice around the HJ.

4.4.1 Photoluminescence

Figure 4.25 compares the normalized Si/Ge NW PL spectra to the c-Si PL spectrum measured at the same (T=20 K) temperature under different excitation intensity. The Si/Ge NW PL spectra clearly exhibit at least two peaks (a narrower PL peak at ~1.08 eV, and a broader PL peak at ~1.025 eV) and, no significant PL with photon energies close to the bulk c-Si TO PL peak at ~1.1 eV. The relative intensities of the two Si/Ge NW PL peaks are found to be excitation and temperature dependent (Figures 4.25 and 4.26). Upon further inspection, the ~1.025 eV is found to be comprised of two peaks, which is most clearly seen at T≥60 K, with the peak positions at ~0.96 and ~1.0 eV (Figures 4.26 and 4.27). The ~1.08 eV PL peak exhibits an asymmetric broadening at higher temperatures (T≥60 K), which can be well fitted using Boltzmann thermal broadening on the high photon energy side of the PL spectrum [131]. The PL peaks at ~1.08 eV and 0.96 eV do not change their positions significantly with temperature, while the PL peak at ~1.0 eV shifts nonmonotonically and exhibits the lowest photon energy between 60 and 80 K.

The absence of bulk, c-Si TO phonon PL at 1.1 eV indicates that in a heavily doped Si substrate the PL is suppressed by Auger processes. The PL related to pure c-Ge is outside of the detector sensitivity spectral range. Thus, the observed PL (Figures 4.25 and 4.26) is associated with radiative transitions in Si/Ge NW HJs. Since no PL associated with D-lines is observed, these Si/Ge nanostructures are found to be substantially dislocation-free, as confirmed from TEM analysis. The PL peak at ~1.08 eV is ~20 meV redshifted and strongly broadened when compared to the c-Si PL spectrum (Figure 4.25), indicating, in agreement with the Raman data and theoretical analysis in Ref. [132], significant strain in the Si/Ge NWs. The PL at hv ~1.0 eV indicates spontaneous formation

of $Si_{1-x}Ge_x$ alloys between the Si and Ge parts of the NWs. Based on the strain introduced into the Si NW part, which can be estimated from the strained Si PL peak spectral position (the PL peak at ~1.08 eV), the peak is believed to be related to $Si_{1-x}Ge_x$ with x~0.2.

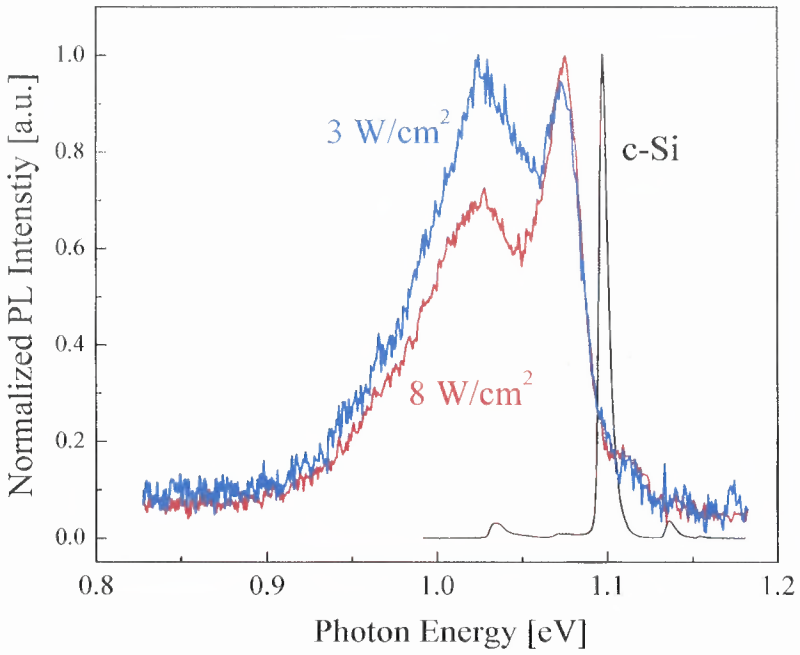

Figure 4.25 Low temperature (T=20 K) normalized PL spectra of Si/Ge NW HJs recorded under two different excitation intensities, as indicated. The normalized PL spectrum of c-Si is shown for comparison.

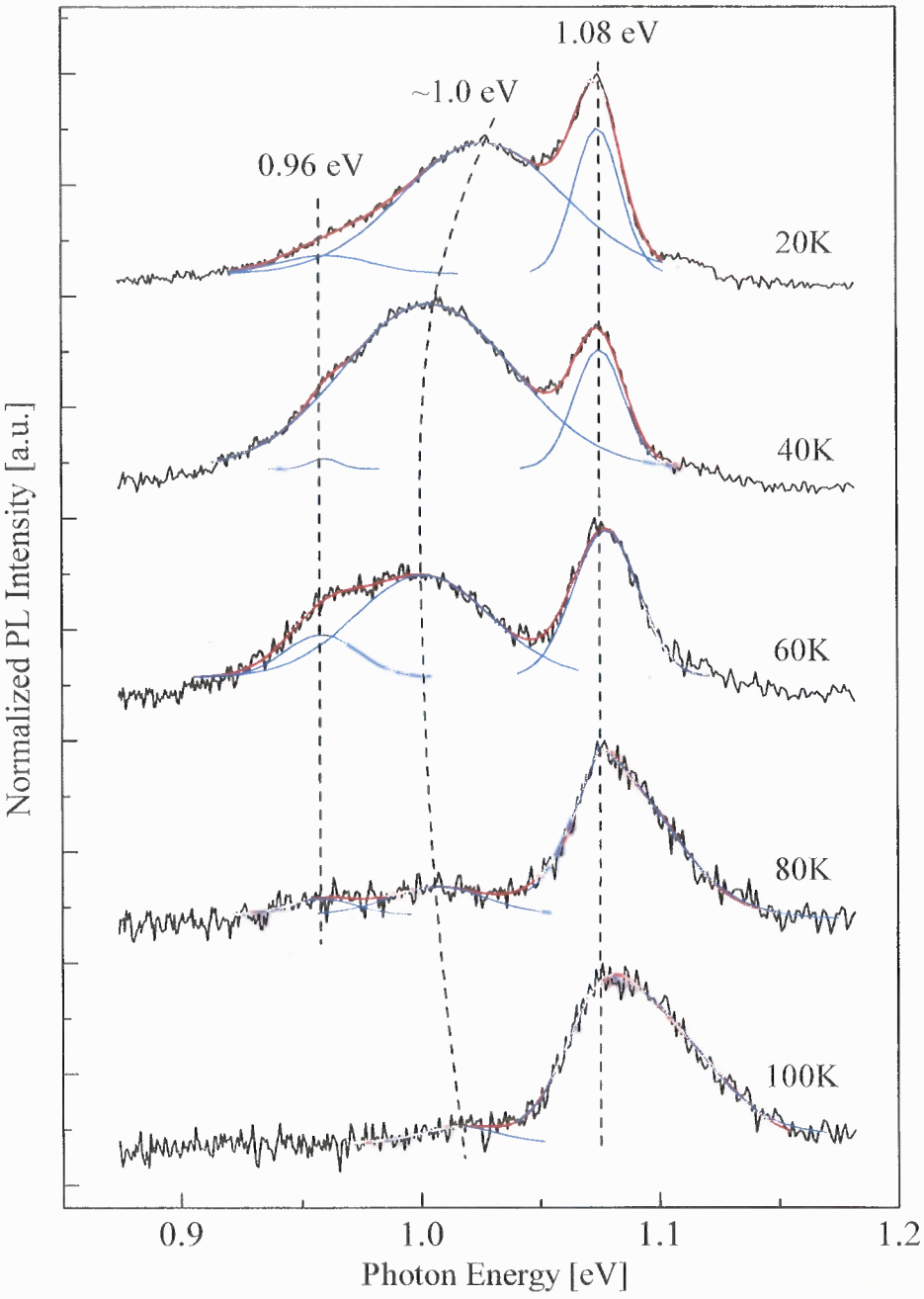

Figure 4.26 Normalized PL spectra of Si/Ge NW HJs measured under 8 W/cm^2 excitation intensity at different (indicated) temperatures with the fitted PL peaks and marked peak positions. The PL spectra are shifted vertically for clarity.

Indeed, the PL peak at ~1.0 eV corresponds to the bandgap PL in a strained $Si_{1-x}Ge_x$ alloy on (111) Si with an alloy composition close to x~0.15-0.2 [1, 12, 133]. Since the PL peaks at ~0.96 and ~1.0 eV show different temperature dependences, they are not associated with TO-phonon replica and no-phonon PL, which is frequently observed in SiGe alloys [1, 12]. Most likely, the PL peaked at ~0.96 eV corresponds to the bandgap of a $Si_{1-x}Ge_x$ alloy with x~0.5 [1, 12].

The spontaneous SiGe intermixing found in VLS grown Si/Ge NW HJs is, most likely, due to residual Si atoms in the eutectic Si-Au alloy after switching to Ge deposition and to strain-induced Si and Ge interdiffusion caused by the 4.2% lattice mismatch between Si and Ge. Our PL data show that the concentration gradient from Si to Ge within the VLS grown Si/Ge NW HJ is not constant and that the $Si_{1-x}Ge_x$ alloy composition x does not change uniformly from 0 to 1. Instead, the PL data suggests the formation of $Si_{1-x}Ge_x$ alloys with preferential compositions of x~0.15-0.2 close to the Si part of the Si/Ge NW and x~0.5 close to the Ge part of the Si/Ge NW. This conclusion, supported by the preliminary TEM and EDX analysis (Figures 4.23, 4.24 and 4.28), is also in agreement with the PL data and SiGe composition measurements in Si/ $Si_{1-x}Ge_x$ 3D (i.e., cluster morphology) nanostructures, where x~0.2 is a typical composition of the SiGe wetting layer and $x \leq 0.5$ is a stable composition close to the SiGe cluster core [3, 12, 34, 133].

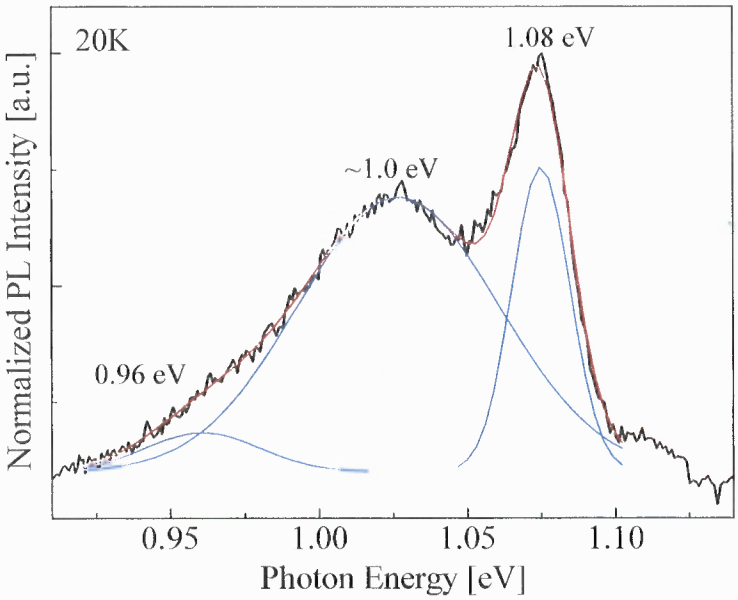

Figure 4.27 Fitted normalized PL peaks with peak positions as marked, demonstrating, in detail, that the broader peak is comprised of two peaks. The spectra is collected in low temperature (T=20 K) and with higher excitation intensity (8 W/cm^2).

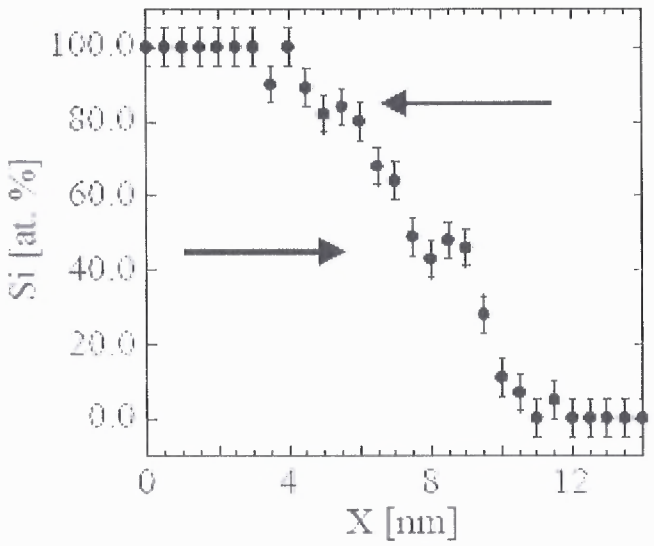

Figure 4.28 EDX data along the NW axis with arrows pointing to the expected preferential compositions of ~80 and 50 atomic percentage of Si (x~0.2 and 0.5, respectively) within the SiGe NW HJs [134].

Figure 4.29 supports this conclusion by showing that the PL peak at ~1.0 eV exhibits an unusual non-monotonic temperature-dependence with a minimum at around 60-80 K. It is proposed that that this shift is produced by a change in Si/Ge NW strain due to the large difference in Si and Ge coefficients of thermal expansion (CsTE). Specifically, as the temperature increases from 20 to 120 K, the Si CTE first decreases and then increases, with a minimum around 60-80 K, while the Ge CTE monotonically increases [135]. The PL peak at ~1.0 eV, which is thought to relate to a strained $Si_{1-x}Ge_x$ alloy (x~0.15-0.2) near the Si part of the Si/Ge NW, follows the direction of the c-Si CTE temperature dependence (Figure 4.29), while the PL peak (at ~0.96 eV) associated with $Si_{1-x}Ge_x$ alloy near the Ge part of the NW (x~0.5) does not show this behavior. Thus, the mismatch in Si and Ge CsTE creates an additional, temperature-dependent strain in the Si/Ge NW HJs.

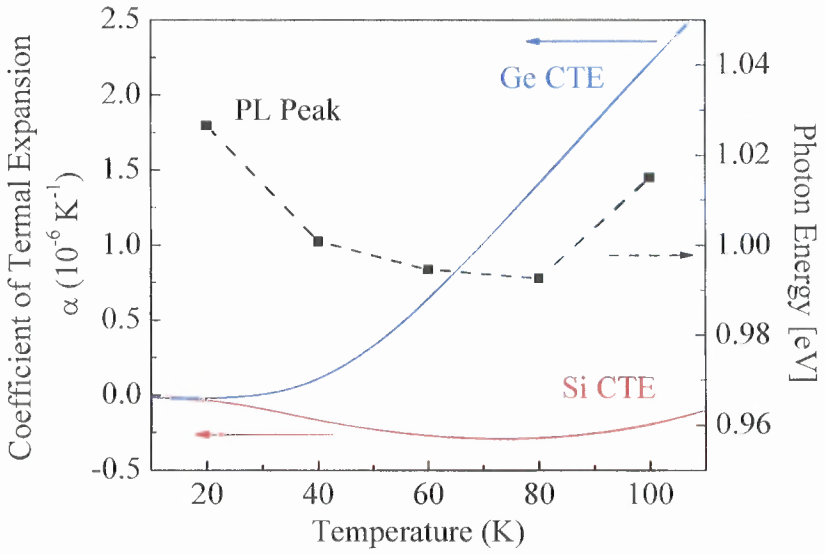

Figure 4.29 Temperature dependence of the PL peak near 1.0 eV in comparison with the temperature dependences of Si and Ge coefficients of thermal expansion (CsTE).

4.4.2 Raman Spectroscopy

Raman scattering measurements of several similar Si/Ge NW HJs (using 514.5 nm excitation wavelength) are shown in Figures 4.30. The Raman spectra confirm the presence of Ge in the NWs (Raman peak at 300 cm^{-1}) as well as strong SiGe intermixing (a peak near 400 cm^{-1}). Also, a broad Raman peak near 500 cm^{-1} associated with Si-Si vibration in SiGe indicates a nonuniform strain [136], while the Raman signal associated with the Si substrate is found at 520 cm^{-1}. A correlation between the strain Si-Si signal near 500 cm^{-1} and PL is also found: PL can only be detected in samples with weaker near 500 cm^{-1} Raman scattering. The absence of PL in samples 1292 (Figure 4.30 (a)) and 1909 (Figure 4.30 (b)) are most likely due to the severe strain and possibly, surface defects in the NWs. Note that the PL spectra discussed in subsection 4.3.1 is sample 1301 (black curve in Figure 4.30 (a)), on which the following Raman-based thermometry and thermal conductivity estimation will focus in details.

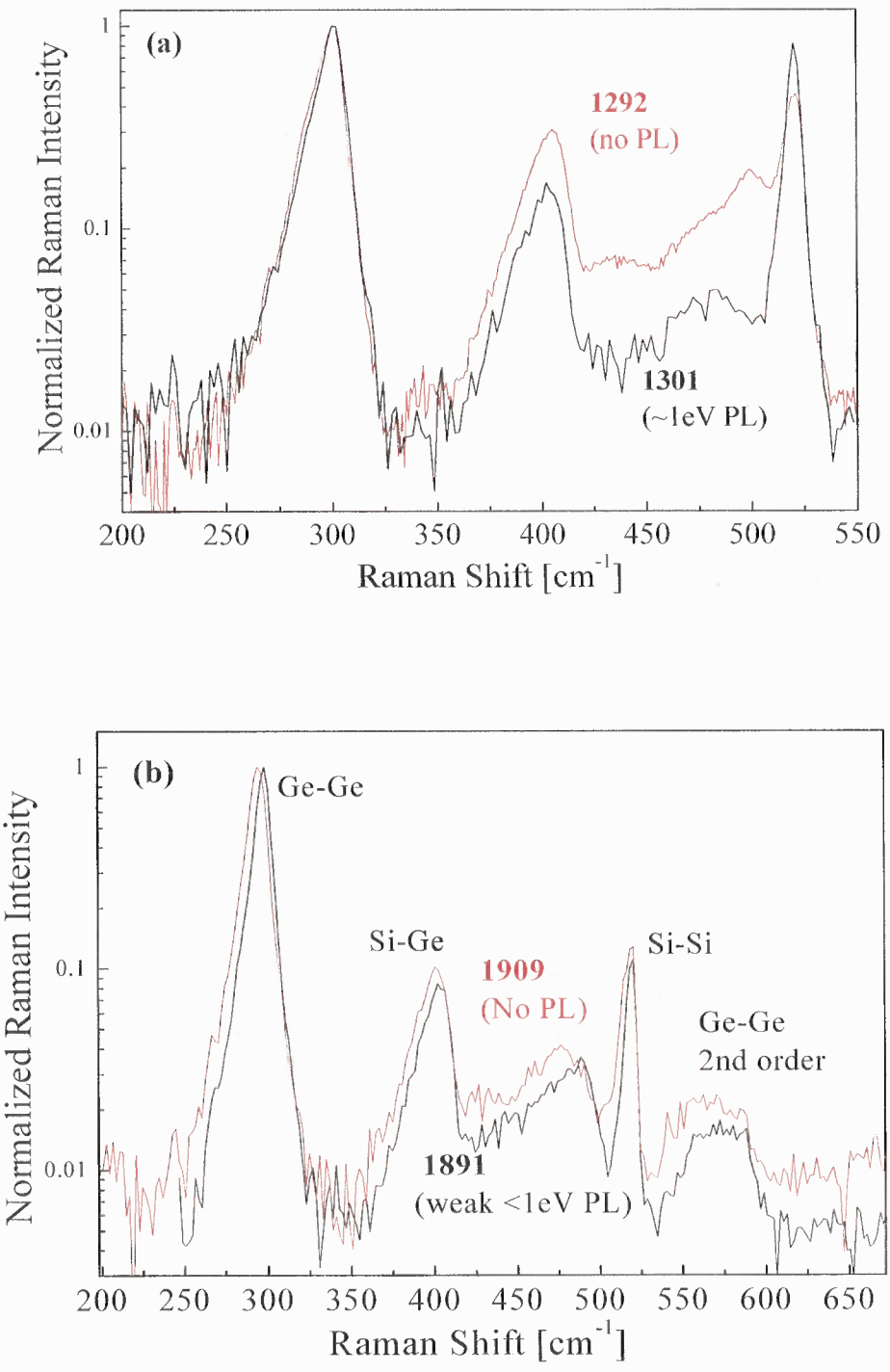

Figure 4.30 Normalized Raman spectra of two Si/Ge NW HJ samples. There is significant SiGe intermixing (a peak at ~400 cm^{-1}) and strained Si (broad peak near 500 cm^{-1}) in all the samples. Note the vertical logarithmic scale.

4.4.3 Raman-based Nano-thermometry and Thermal Conductivity Calculations

Two surface temperatures of Si/Ge NW HJs samples 1292 and 1301 are calculated from Raman-based thermometry by comparing the Stoke/anti-Stoke peak intensity of Ge-Ge vibration mode (~300 cm^{-1}) and unstrained Si-Si vibration mode (~520 cm^{-1}). The sample is under 457.9 nm excitation with power intensities of 0.35-1.5 kW/cm^2. The calculated temperatures with comparison to backside temperatures, taken by a thermal-couple thermometer, are show in Figure 4.31 (a). The overall system (Si/Ge NW HJs on Si carrier wafer) thermal conductivities are calculated using the method described in Section 3.3 and the results are plotted with respect to Raman temperature obtained from Ge-Ge vibrations (Figure 4.31 (b)).

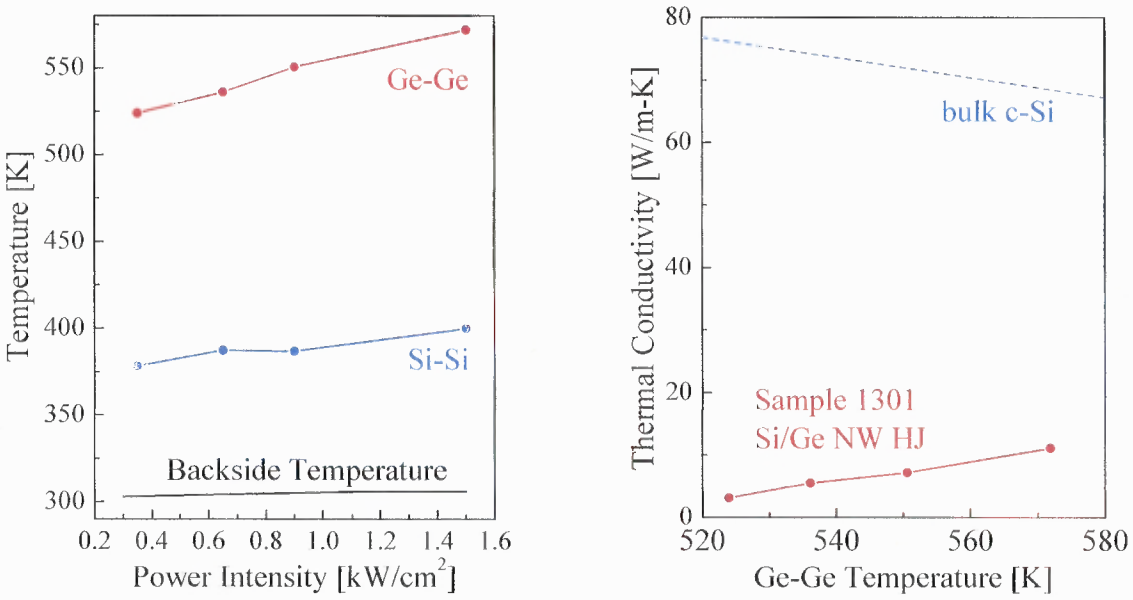

Figure 4.31 Raman-based thermometry in Si/Ge NW HJs: (a) calculated surface temperatures from Si-Si and Ge-Ge vibration modes compared to backside and ambient temperatures (as indicated), and (b) estimated thermal conductivity compared to bulk c-Si.

In the NW HJs, due to the long, thin NW geometry, the (111) substrate and NW crystal orientation (i.e., NW preferential growth direction is perpendicular to the wafer surface [35, 36]) and extremely short penetration depth of 457.9 nm light in Ge (<20 nm), most of the laser power is presumed to be absorbed in the Ge part. From the ~300 nm penetration depth of 457.9 nm light in Si, the Raman temperature calculated from Si-Si vibration modes are presumed to be the average temperature in Si part of the NWs, rather than the substrate. The large temperature gradient between the Si-Si and Ge-Ge modes is presumably over only a couple hundred nanometers in length (compare to temperature gradient between Si-Si Raman temperature and backside temperature over ~200 μm) indicates the NW HJs have thermal conductivity ($\kappa \propto L / \Delta T$) much lower than the system thermal conductivity shown in Figure 4.31. With the reduced thermal conductivity, good carrier transport and high carrier mobility, the Si/Ge NW HJs are good candidates for thermoelectric (TE) device applications.

4.4.4 Thermal Voltage Measurements

In general, the TE figure of merit (FOM) is expressed as:

$$ZT = S^2 T \cdot \frac{\sigma}{\kappa}, \tag{4.1}$$

where S is the Seebeck coefficient or TE power, T is the temperature, σ is the electrical conductivity and κ is the thermal conductivity. The studies shown in this dissertation, in particular, the Raman-based thermometry have illustrated that the SiGe nanostructures have very low thermal conductivity, which enhances the TE FOM. The Seebeck coefficient can be found by measuring the thermal voltage (V) induced by a temperature gradient ΔT:

$V = S \cdot \Delta T$. An illustration of the preliminary TE power measurement is shown in Figure 4.32. The sample is adhered to a Cu sheet by silver paste. In setup (a), Ag wire is attached to the NWs and the Cu sheet by silver paste and the heat source is placed on the substrate side of the sample; in setup (b), Al foil is attached to the NWs by silver paste to provide even heat distribution and heat source is placed on the NW side of the sample. The experiment is done in a chemical hood, where the constant air flow keeps the cool side temperature close to the laboratory ambient temperature. On the hot side, heat is created by a hot plate, and the thermal voltages are measured by a Keithley 2000 electrometer with resolution of 0.1 μV.

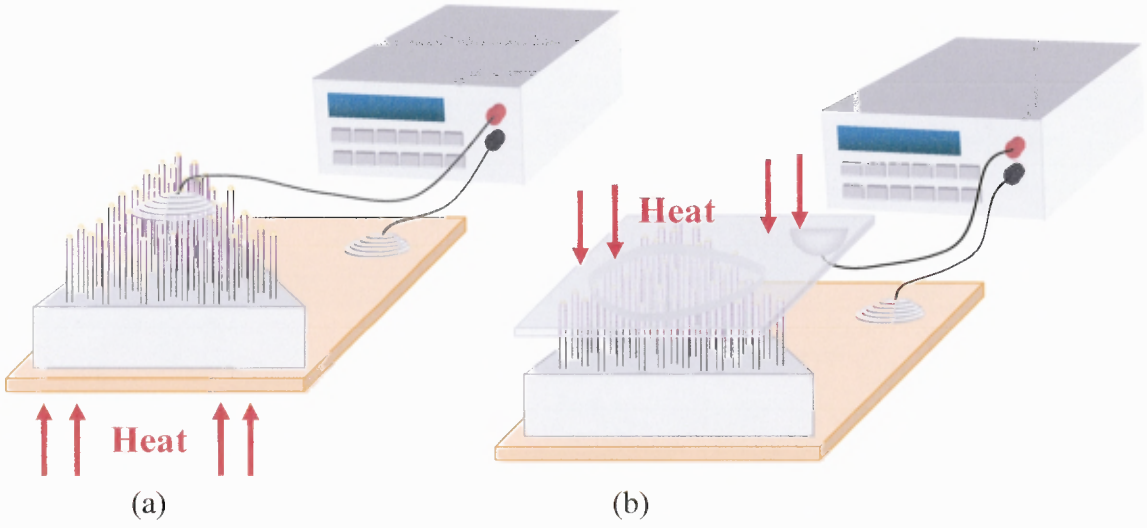

Figure 4.32 Setup for thermopower (Seebeck coefficient) measurement: (a) heat source on the wafer side of sample and (b) heat source on the NW HJ side of sample.

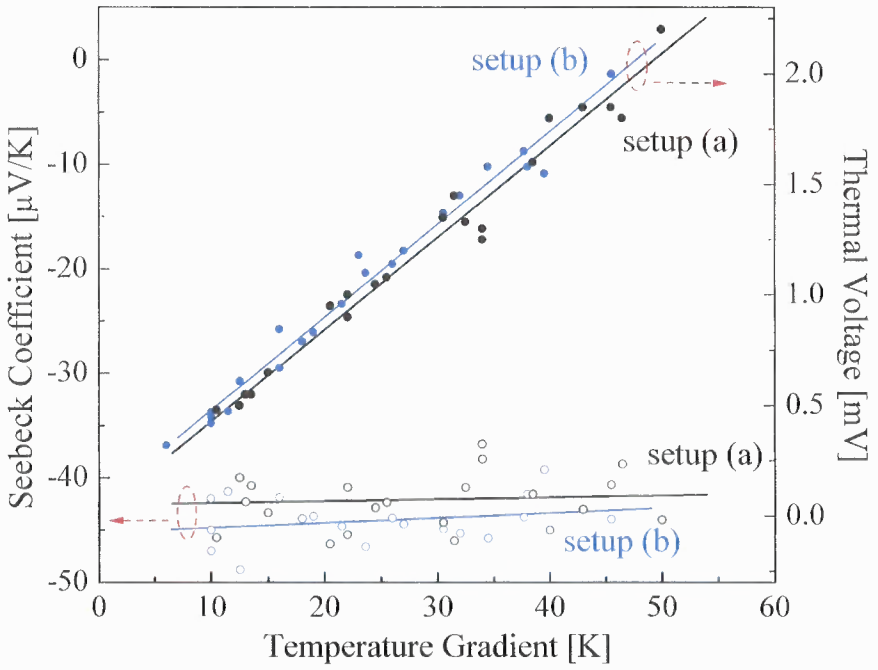

Figure 4.33 Thermal voltages (solid dots) and the calculated Seebeck coefficients (circles) of Si/Ge NW HJs measured with different setups: (a) heat source on the wafer side of sample (black) and (b) heat source on the NW HJ side of sample (blue). Linear fittings of the data are also shown for clarity.

Figure 4.33 shows the results of the preliminary thermal voltage measurements as solid dots and the calculated Seebeck coefficients as circles. In addition, the results by using setup (a) is shown in black and setup (b) is shown in blue. Linear fittings are done with each set of data, and the Seebeck coefficient is estimated to be about -42 and -45 μV/K for setup (a) and (b), respectively. Note that the negative sign comes from the opposite direction of the electric field (higher potential to lower potential) and temperature gradient (lower temperature to higher temperature). These preliminary results are comparable to the thermal voltages of SiGe alloys in literatures (~100 μV/K for doped $Si_{0.8}Ge_{0.2}$) [47, 137].

The small difference can be explained by the fact that flowing air is not a sufficient enough heat sink, thus the cold side temperature is actually higher than laboratory ambient temperature used in the calculations. Although a more complex experiment setup is needed to measure the precise thermal voltage of the nanostructure, these preliminary results shows definite applicability of Si/Ge NW HJs in TE devices.

CHAPTER 5

CONCLUSION

This dissertation has presented detailed studies of the structural, optical, electrical and thermal properties of Si and SiGe nanostructures, including Si:B delta-doped multilayer SLs, three-dimensional (3D) cluster morphology and two-dimensional (2D) planar $Si/Si_{1-x}Ge_x$ multilayer superlattices, one-dimensional (1D) Si nanowire (NW) and Si/Ge NW heterojunctions (HJs). A review of the nanostructure fabrication techniques, their fundamental properties (structural, optical, electrical and thermal) and characterization methods (performed by the author at NJIT and by the collaborators) is given in the first half of the dissertation. The second half is devoted to the experimental results and extensive discussions. Finally, this chapter will serve as a summary of this research's original contribution to the field and provide an outlook for potential device application and future research.

In the Si:B delta-doped multilayer, the optical characterizations revealed low strain and no dopant segregation from the heavily B delta-doped multilayers. It proves that multi-layer delta-doping is an effective way to achieve highly localized dopants without creating significant dopant-induced strain or dopant segregation. Raman-based thermometry showed no significant change in the overall thermal conductivity of the multilayer structures. Temperature dependent optical reflectance, current-voltage (I-V) and capacitance-voltage (C-V) characteristics, as well as pulse-modulated electro-reflectance measurements show that carrier concentration dependent optical reflectivity in these samples is quite significant. These results show that these delta-doped multilayer

nanostructures can achieve nearly the same performance goals as heavily doped bulk materials without significant strain or dopant segregation and that they can be used as electrically controlled mirrors in high speed, sub-micron electro-optical devices and systems.

The structural analysis of the Si/SiGe multilayers reveals that they are defect-free, high Ge content, truly epitaxial Si/SiGe nanostructures. The lattice-mismatch-induced strain is partially relaxed by the 3D clusters morphology and, possibly, slightly graded Ge composition near the Si/SiGe heterointerfaces. Raman-based thermometry measurements, at the first time, finds a correlation between the thermal conductivity and the intensity of the Raman signal associated with the folding of longitudinal acoustic phonons. These results suggest that such Si/SiGe nanostructures can be specifically engineered and used as highly anisotropic "heat sinks." For example, 2D Si/SiGe multilayers can be designed to provide a very low vertical heat conductance and efficient lateral heat dissipation. This particular device design can significantly improve the previously reported anisotropy in cross-plane and in-plane thermal conductivity in Si/Ge multilayers [86, 138]. Their application can be found in CMOS-compatible, highly directional thermal insulators (vertical or cross-plane direction) and heat sinks (lateral or in-plane direction).

In the metal-catalyzed Si NWs, photoluminescence (PL) and Raman spectroscopy reveals substantial strain as the result of the highly non-equilibrium, high growth rate vapor-liquid-solid-based fabrication. Raman-based temperature measurements and thermal conductivity estimates shows that the NW thermal conductivity is reduced by a factor of $\sim 10^{-2}$, and it is limited by the NW surface scattering rather than the reduction of the phonon mean free path due to the small NW diameter.

The characterizations on axial Si/Ge NW HJs show that it is feasible to grow dislocation-free and abrupt interface Si/Ge HJs without traditional limitations of critical thicknesses. Although the lattice-mismatched strain is partially relax by the expansion of the NW diameter at the heterointerface, substantial built-in strain is found. The Raman, PL, and electron dispersive x-ray spectroscopy measurements show the spontaneous formation of several nanometer-thick $Si_{1-x}Ge_x$ transition layers between the Si and Ge parts of the NW HJs and indicate preferential alloy compositions of x~0.15-0.2 (close to the Si NW part) and x~0.5 (close to the Ge NW part). The mismatch in Si and Ge coefficients of thermal expansion is found to be responsible for additional strain and an unusual PL peak shift as a function of temperature. Raman-based thermometry shows that the thermal conductivity in Si/Ge NW HJs is lower than that in Si NWs. With the reduced thermal conductivity, and presumably high carrier mobility, the Si/Ge NW HJs are good candidates for thermoelectric (TE) device applications. Preliminary measurements show that in these undoped Si/Ge NWs, the Zeebeck coefficient is in the order of ~ 40 μV/K; by using doped materials it could be significantly improved.

Lastly, this dissertation places a special emphasis on thermal properties of Si-based nanostructures using the Raman-based thermometry as a fast, non-destructive and contact-free measurement allowing an accurate estimation of thermal conductivity; possible TE device applications are discussed as well [139]. A summary of thermal conductivities of the studied Si-based nanostructures is shown in Figure 5.1. The dotted lines are experimental data taken from Ref. [18, 20, 63, 75, 77]; the red line and the bubbles are thermal conductivity estimates performed in this research. Thermal conductivities of these nanostructures are found to be greatly reduced (up to 10^2-10^3 times less than c-Si),

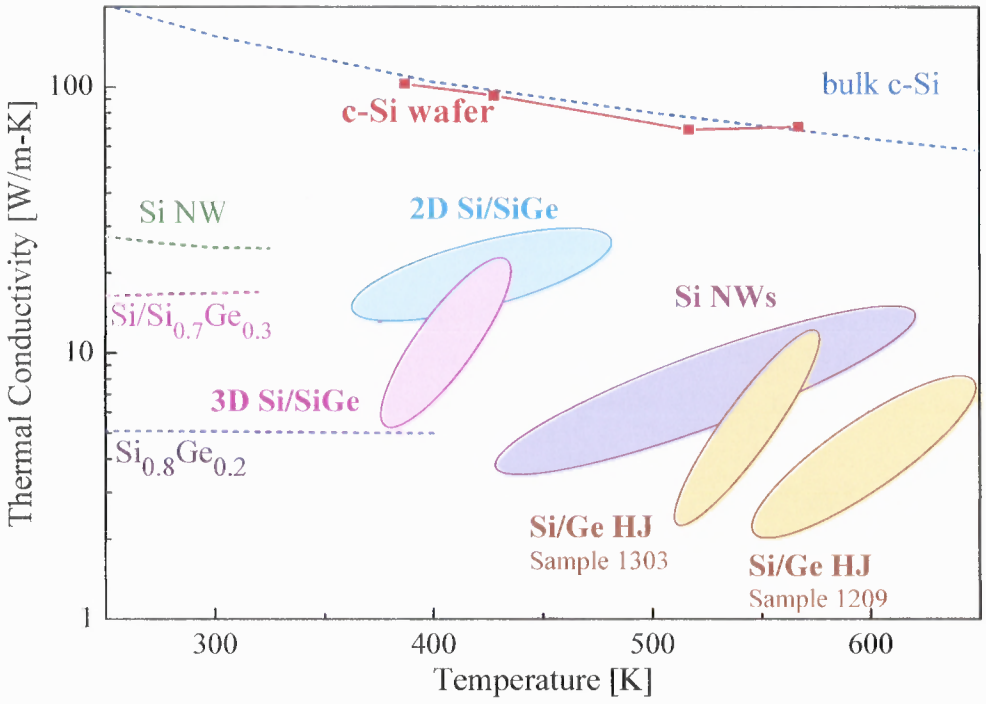

Figure 5.1 Summary of Raman-based-thermometry-derived thermal conductivities of Si (line) and SiGe nanostructures (bubbles, as marked), compare to known bulk c-Si, SiGe alloy, Si/SiGe superlattice and Si nanowires (dotted lines, as marked) [18, 20, 63, 75, 77].

and it is shown to be mainly due to an increased phonon scattering at the nanostructures' boundaries and interfaces, boundary/interface-related structural defects, interface roughness and modification of acoustic phonon dispersion. The found reduced thermal conductivity suggests that in designing nano-scale Si devices, thermal conductivity is the key factor, and it should be addressed properly in all applications where heat dissipation is a potential issue. On the other hand, the found reduced thermal conductivity is a potential advantage for TE device applications, assuming that electrical conductivity is high. However, the same phenomena that are responsible for the reduction in a material's thermal conductivity, in general, are also effective in reducing its electrical conductivity

due to the strong reduction in carrier mobility, diffusion coefficient and lifetime. For example, thermal conductivity in a-Si is reduced by ~100 times compared to that in c-Si, while carrier mobility is reduced by factor of 10^4-10^5 [140, 141]. Therefore, continued theoretical and experimental work in realizing Si- and SiGe-nanostructure-based TE devices should not be entirely focused on the thermal conductivity reduction but rather on an engineering solution utilizing the balance between thermal and electric transport in these truly fascinating systems.

REFERENCES

[1] D. J. Paul, "Si/SiGe Heterostructures: From Material and Physics to Devices and Circuits," *Semicond. Sci. Technol.,* vol. 19, pp. R75-R108, 2004.

[2] J. W. Matthews and A. E. Blakeslee, "Defects in Epitaxial Multilayers : III. Preparation of Almost Perfect Multilayers," *J. Crys. Growth,* vol. 32, pp. 265-273, 1976.

[3] B. V. Kamenev, H. Grebel, L. Tsybeskov, T. I. Kamins, R. S. Williams, J. M. Baribeau, and D. J. Lockwood, "Polarized Raman Scattering and Localized Embedded Strain in Self-Organized Si/Ge Nanostructures," *Appl. Phys. Lett.,* vol. 83, pp. 5035-5037, 2003.

[4] U. Schmid, F. Luke, N. E. Christensen, M. Alouani, M. Cardona, E. Kasper, H. Kibbel, and H. Presting, "Interband Transitions in Strain-symmetrized Ge_4Si_6 Superlattices," *Phys. Rev. Lett.,* vol. 65, p. 1933, 1990.

[5] F. K. LeGoues, B. S. Meyerson, and J. F. Morar, "Anomalous Strain Relaxation in SiGe Thin Films and Superlattices," *Phys. Rev. Lett.,* vol. 66, p. 2903, 1991.

[6] B. E. Weir, L. C. Feldman, D. Monroe, H. J. Grossmann, R. L. Headrick, and T. R. Hart, "Electrical Characterization of an Ultrahigh Concentration Boron Delta-doping Layer," *Appl. Phys. Lett.,* vol. 65, pp. 737-739, 1994.

[7] L. Oberbeck, N. J. Curson, M. Y. Simmons, R. Brenner, A. R. Hamilton, S. R. Schofield, and R. G. Clark, "Encapsulation of Phosphorus Dopants in Silicon for the Fabrication of a Quantum Computer," *Appl. Phys. Lett.,* vol. 81, pp. 3197-3199, 2002.

[8] S. L. Wu, T. K. Carns, S. J. Wang, and K. L. Wang, "Boron Delta-doped Si Metal Semiconductor Field-effect Transistor Grown by Molecular-beam Epitaxy," *Appl. Phys. Lett.,* vol. 63, pp. 1363-1365, 1993.

[9] H. P. Zeindl, B. Bullemer, I. Eisele, and G. Temple, "Delta-Doped MESFET with MBE-Grown Si," *J. Electrochem. Soc.,* vol. 136, pp. 1129-1131, 1989.

[10] E. de Fresart, K. L. Wang, and S. S. Rhee, "Boron Surface Segregation in Silicon Molecular Beam Epitaxy," *Appl. Phys. Lett.,* vol. 53, pp. 48-50, 1988.

[11] M. Milosavljevic, G. Shao, M. A. Lourenco, R. M. Gwilliam, and K. P. Homewood, "Engineering of Boron-induced Dislocation Loops for Efficient Room-temperature Silicon Light-emitting Diodes," *J. Appl. Phys.,* vol. 97, p. 073512, 2005.

[12] K. Brunner, "Si/Ge Nanostructures," *Rep. Prog. Phys.,* vol. 65, pp. 27-72, 2002.

[13] D. J. Eaglesham and M. Cerullo, "Dislocation-free Stranski-Krastanow Growth of Ge on Si(100)," *Phys. Rev. Lett.,* vol. 64, p. 1943, 1990.

[14] J. M. Baribeau, X. Wu, N. L. Rowell, and D. J. Lockwood, "Ge Dots and Nanostructures Grown Epitaxially on Si," *J. Phys.: Cond. Mat.,* vol. 18, pp. R139-R174, 2006.

[15] V. Le Thanh, P. Boucaud, D. D?barre, Y. Zheng, D. Bouchier, and J. M. Lourtioz, "Nucleation and Growth of Self-assembled Ge/Si(001) Quantum Dots," *Phys. Rev. B,* vol. 58, pp. 13115-13120, 1998.

[16] O. G. Schmidt, O. Kienzle, Y. Hao, K. Eberl, and F. Ernst, "Modified Stranski-Krastanov Growth in Stacked Layers of Self-assembled Islands," *Appl. Phys. Lett.,* vol. 74, pp. 1272-1274, 1999.

[17] V. Le Thanh, V. Yam, P. Boucaud, F. Fortuna, C. Ulysse, D. Bouchier, L. Vervoort, and J. M. Lourtioz, "Vertically Self-organized Ge/Si(001) Quantum Dots in Multilayer Structures," *Phys. Rev. B,* vol. 60, pp. 5851-5857, 1999.

[18] S. M. Lee, G. C. David, and V. Rama, "Thermal Conductivity of Si-Ge Superlattices," *Appl. Phys. Lett.,* vol. 70, pp. 2957-2959, 1997.

[19] T. Borca-Tasciuc, W. Liu, J. Liu, T. Zeng, D. W. Song, C. D. Moore, G. Chen, K. L. Wang, M. S. Goorsky, T. Radetic, R. Gronsky, T. Koga, and M. S. Dresselhaus, "Thermal Conductivity of Symmetrically Strained Si/Ge Superlattices," *Superlattices and Microstructures,* vol. 28, pp. 199-206, 2000.

[20] S. T. Huxtable, A. R. Abramson, C.-L. Tien, A. Majumdar, C. LaBounty, X. Fan, G. Zeng, J. E. Bowers, A. Shakouri, and E. T. Croke, "Thermal Conductivity of Si/SiGe and SiGe/SiGe Superlattices," *Appl. Phys. Lett.,* vol. 80, pp. 1737-1739, 2002.

[21] B. Yang, J. L. Liu, K. L. Wang, and G. Chen, "Simultaneous Measurements of Seebeck Coefficient and Thermal Conductivity Across Superlattice," *Appl. Phys. Lett.,* vol. 80, p. 1758, 2002.

[22] C. N. R. Rao, F. L. Deepak, G. Gundiah, and A. Govindaraj, "Inorganic Nanowires," *Progress in Solid State Chemistry,* vol. 31, pp. 5-147, 2003.

[23] R. S. Wagner and W. C. Ellis, "Vapor-liquid-solid Mechanism of Single Crystal Growth " *Appl. Phys. Lett.,* vol. 4, pp. 89-90, 1964.

[24] C. C. Striemer, P. M. Fauchet, and L. Tsybeskov, "Lateral Superlattices Fabricated with Interferometric Lithography for Nanoscale Device Applications," *Mat. Res. Soc. Symp. Proc.,* vol. 638, pp. F5.13.1-F5.13.6, 2001.

[25] C. C. Striemer, R. Krishnan, Q. Xie, L. Tsybeskov, and P. M. Fauchet, "Periodic Two-dimensional Arrays of Silicon Quantum Dots for Nanoscale Device Applications," *Mat. Res. Soc. Symp. Proc.*, vol. 737, pp. F3.27.1-F3.27.6, 2003.

[26] H. H. Solak, C. David, J. Gobrecht, L. Wang, and F. Cerrina, "Four-wave EUV Interference Lithography," *Microelec. Eng.*, vol. 61-62, pp. 77-82, 2002.

[27] A. D. Apostol, V. Damian, F. Garoi, I. Iordache, P. C. Logofatu, V. Nascov, A. Sima, B. D. Cristea, and R. Muller, "2D Multiple Beam Interference Lithography," in *International Semiconductor Conference, 2006*, 2006, pp. 151-154.

[28] J. M. Carter, R. C. Fleming, T. A. Savas, M. E. Walsh, T. B. O'Reilly, M. L. Schattenburg, and H. I. Smith, "Interference Lithography," MIT2003.

[29] M. E. Walsh, "Nanostructuring Magnetic Thin Films Using Interference Lithography," in *Electrical Engineering and Computer Science*. vol. Master of Science in Electrical Engineering Cambridge, MA: Massachusetts Institute of Technology, 2000, p. 85.

[30] D. J. Kang, J.-K. Kim, and B.-S. Bae, "Fabrication of Micro-optical Devices by Holographic Interference of High Photosensitive Inorganic-organic Hybrid Materials (Photo-HYBIRMER)," *Mat. Res. Soc. Symp. Proc.*, vol. 846, p. DD10.3.1, 2005.

[31] B. Predel, "Au-Si (Gold-Silicon)," in *Ac-Au – Au-Zr*, 1991, pp. 1-5.

[32] J. M. Baribeau, N. L. Rowell, and D. J. Lockwood, "Advances in the Growth and Characterization of Ge Quantum Dots and Islands," *J Mat. Res.*, vol. 20, pp. 3278-3293, 2005.

[33] L. Tsybeskov, B. V. Kamenev, J. M. Baribeau, and D. J. Lockwood, "Optical Properties of Composition-controlled Three-dimensional $Si/Si_{1-x}Ge_x$ Nanostructures," *IEEE J. Quantum Electron.*, vol. 12, pp. 1579-1584, 2006.

[34] D. J. Lockwood, J. M. Baribeau, B. V. Kamenev, E. K. Lee, and L. Tsybeskov, "Structural and Optical Properties of Three-Dimensional $Si_{1-x}Ge_x/Si$ Nanostructures," *Semiconductor Science and Technology,* vol. 23, art. no. 064003, 2008.

[35] V. Schmidt, S. Senz, and U. Gösele, "Diameter-dependent Growth Direction of Epitaxial Silicon Nanowires," *Nano Letters,* vol. 5, pp. 931-935, 2005.

[36] Y. Wu, Y. Cui, L. Huynh, C. J. Barrelet, D. C. Bell, and C. M. Lieber, "Controlled Growth and Structures of Molecular-scale Silicon Nanowires," *Nano Letters,* vol. 4, pp. 433-436, 2004.

[37] S. Hofmann, C. Ducati, R. J. Neill, S. Piscanec, A. C. Ferrari, J. Geng, R. E. Dunin-Borkowski, and J. Robertson, "Gold Catalyzed Growth of Silicon Nanowires by Plasma Enhanced Chemical Vapor Eeposition," *J. Appl. Phys.*, vol. 94, pp. 6005-6012, 2003.

[38] R. L. Anderson, "Experiments on Ge-GaAs Heterojunctions," *Solid State Electronics,* vol. 5, 1962.

[39] S. M. Sze, *Physics of Semiconductor Devices*, 2 ed.: John Wiley & Sons, 1981.

[40] F. Schäffler, "High-mobility Si and Ge Structures," *Semicond. Sci. Technol.*, vol. 12, pp. 1515-1549, 1997.

[41] R. People and J. C. Bean, "Band Alignments of Coherently Strained Ge_xSi_{1-x}/Si Heterostructures on <001> Ge_ySi_y substrates," *Appl. Phys. Lett.*, vol. 48, pp. 538-540, 1986.

[42] D. V. Lang, R. People, J. C. Bean, and A. M. Sergent, "Measurement of the Band Gap of Ge_xSi_{1-x}/Si Strained-layer Heterostructures," *Appl. Phys. Lett.*, vol. 47, pp. 1333-1335, 1985.

[43] E.-K. Lee, "Optical Properties and Carrier Transport in $Si/Si_{1-x}Ge_x$ Nanostructures," in *Department of Electrical and Computer Engineering*. vol. Doctor of Philosophy Newark, NJ: New Jersey Institute of Technology, 2008, pp. 1-116.

[44] G. Abstreiter, H. Brugger, T. Wolf, H. Jorke, and H. J. Herzog, "Strain-Induced Two-Dimensional Electron Gas in Selectively Doped Si/Si_xGe_{1-x} Superlattices," *Phys. Rev. Lett.*, vol. 54, p. 2441, 1985.

[45] C. Y. Ho, R. W. Powell, and P. E. Liley, "Thermal Conductivity of the Elements," *J. Phys. Chem. Ref. Data,* vol. 1, pp. 279-421, 1972.

[46] G. P. Srivastava, "Lattice Thermal Conduction Mechanism in Solids," in *High Thermal Conductivity Materials*, S. L. Shindé and J. S. Goela, Eds.: Springer, 2006, pp. 1-35.

[47] C. B. Vining, W. Laskow, J. O. Hanson, R. R. Van der Beck, and P. D. Gorsuch, "Thermoelectric Properties of Pressure-sintered $Si_{0.8}Ge_{0.2}$ Thermoelectric Alloys," *J. Appl. Phys.*, vol. 69, pp. 4333-4340, 1991.

[48] M. Asheghi, M. N. Touzelbaev, K. E. Goodson, Y. K. Leung, and S. S. Wong, "Temperature-Dependent Thermal Conductivity of Single-Crystal Silicon Layers in SOI Substrates," *J Heat Trans.*, vol. 120, pp. 30-36, 1998.

[49] R. Soref, "The Past, Present, and Future of Silicon Photonics," *IEEE J. Quantum Electron.*, vol. 12, pp. 1678-1687, 2006.

[50] S. S. Iyer and Y. H. Xie, "Light Emission from Silicon," *Science,* vol. 260, pp. 40-46, 1993.

[51] H. Rong, A. Liu, R. Jones, O. Cohen, D. Hak, R. Nicolaescu, A. Fang, and M. Paniccla, "An All-silicon Raman Laser," *Nature,* vol. 433, pp. 292-294, 2005.

[52] B. Jalali and S. Fathpour, "Silicon Photonics," *J. Lightwave Tech.,* vol. 24, pp. 4600-4615, 2006.

[53] L. Pavesi, S. Gaponenko, and L. Dal Negro, *Towards the First Silicon Laser*: Springer, 2003.

[54] T. Orii, M. Hirasawa, and T. Seto, "Tunable, Narrow-band Light Emission from Size-selected Si Nanoparticles Produced by Pulsed-laser Ablation," *Appl. Phys. Lett.,* vol. 83, pp. 3395-3397, 2003.

[55] D. J. Lockwood, B. T. Sullivan, and H. J. Labb, "Visible Light Emission from Si/SiO_2 Superlattices in Optical Microcavities," *J. Luminescence,* vol. 80, pp. 75-79, 1998.

[56] L. Pavesi, L. Dal Negro, C. Mazzoleni, G. Franzo, and F. Priolo, "Optical Gain in Silicon Nanocrystals," *Nature,* vol. 408, pp. 440-444, 2000.

[57] L. Dal Negro, M. Cazzanelli, L. Pavesi, S. Ossicini, D. Pacifici, G. Franz, F. Priolo, and F. Iacona, "Dynamics of Stimulated Emission in Silicon Nanocrystals," *Appl. Phys. Lett.,* vol. 82, pp. 4636-4638, 2003.

[58] M. Cazzanelli, D. Navarro-Urriós, F. Riboli, N. Daldosso, L. Pavesi, J. Heitmann, L. X. Yi, R. Scholz, M. Zacharias, and U. Gösele, "Optical Gain in Monodispersed Silicon Nanocrystals," *J. Appl. Phys.,* vol. 96, pp. 3164-3171, 2004.

[59] S. G. Cloutier, P. A. Kossyrev, and J. Xu, "Optical Gain and Stimulated Emission in Periodic Nanopatterned Crystalline Silicon," *Nature Materials,* vol. 4, pp. 887-891, 2005.

[60] P. M. Fauchet, J. Ruan, H. Chen, L. Pavesi, L. Dal Negro, M. Cazzaneli, R. G. Elliman, N. Smith, M. Samoc, and B. Luther-Davies, "Optical Gain in Different Silicon Nanocrystal Systems," *Optical Materials,* vol. 27, pp. 745-749, 2005.

[61] J. D. Holmes, K. P. Johnston, R. C. Doty, and B. A. Korgel, "Control of Thickness and Orientation of Solution-grown Silicon Nanowires," *Science,* vol. 287, pp. 1471-1473, 2000.

[62] J. Hu, T. W. Odom, and C. M. Lieber, "Chemistry and Physics in One Dimension: Synthesis and Properties of Nanowires and Nanotubes," *Acc. Chem. Res.,* vol. 32, pp. 435-445, 1999.

[63] A. I. Hochbaum, R. Chen, R. D. Delgado, W. Liang, E. C. Garnett, M. Najarian, A. Majumdar, and P. Yang, "Enhanced Thermoelectric Performance of Rough Silicon Nanowires," *Nature,* vol. 451, pp. 163-167, 2008.

[64] X. T. Zhou, J. Q. Hu, C. P. Li, D. D. D. Ma, C. S. Lee, and S. T. Lee, "Silicon Nanowires as Chemical Sensors," *Chem. Phys. Lett.,* vol. 369, pp. 220-224, 2003.

[65] G. Zheng, F. Patolsky, Y. Cui, W. U. Wang, and C. M. Lieber, "Multiplexed Electrical Detection of Cancer Markers with Nanowire Sensor Arrays," *Nature Biotechnology,* vol. 23, pp. 1294 - 1301, 2005.

[66] F. Patolsky and C. M. Lieber, "Nanowire Nanosensors," *Mat. Today,* vol. 8, pp. 20-28, 2005.

[67] R. Gupta, W. J. Yoo, Y. Wang, Z. Tan, G. Samudra, S. Lee, D. S. H. Chan, K. P. Loh, L. K. Bera, N. Balasubramanian, and D. L. Kwong, "Formation of SiGe Nanocrystals in HfO_2 Using in Situ Chemical Vapor Deposition for Memory Applications," *Appl. Phys. Lett.,* vol. 84, pp. 4331-4333, 2004.

[68] Y. Liu, S. Tang, and S. K. Banerjee, "Tunnel Oxide Thickness Dependence of Activation Energy for Retention Time in SiGe Quantum Dot Flash Memory," *Appl. Phys. Lett.,* vol. 88, art. no. 213504, 2006.

[69] Y. Liu, S. Dey, S. Tang, D. Q. Kelly, J. Sarkar, and S. K. Banerjee, "Improved Performance of SiGe Nanocrystal Memory with VARIOT Tunnel Barrier," *IEEE Trans. on Electron Devices,* vol. 53, pp. 2598-2602, 2006.

[70] Y. S. Tang, W. X. Ni, C. M. Sotomayor Torres, and G. V. Hansson, "Fabrication and Characterisation of Si-$Si_{0.7}Ge_{0.3}$ Quantum Dot Light Emitting Diodes," *Elec. Lett.,* vol. 31, pp. 1385-1386, 1995.

[71] K. Eberl, O. G. Schmidt, R. Duschl, O. Kienzle, E. Ernst, and Y. Rau, "Self-assembling SiGe and SiGeC Nanostructures for Light Emitters and Tunneling Diodes," *Thin Solid Films,* vol. 369, pp. 33-38, 2000.

[72] N. D. Zakharov, V. G. Talalaev, P. Werner, A. A. Tonkikh, and G. E. Cirlin, "Room-temperature Light Emission from a Highly Strained Si/Ge Superlattice," *Appl. Phys. Lett.,* vol. 83, pp. 3084-3086, 2003.

[73] W. H. Chang, A. T. Chou, W. Y. Chen, H. S. Chang, T. M. Hsu, Z. Pei, P. S. Chen, S. W. Lee, L. S. Lai, S. C. Lu, and M. J. Tsai, "Room-temperature Electroluminescence at 1.3 and 1.5 μm from Ge/Si Self-assembled Quantum Dots," *Appl. Phys. Lett.,* vol. 83, pp. 2958-2960, 2003.

[74] L. Tsybeskov, E.-K. Lee, H.-Y. Chang, B. V. Kamenev, D. J. Lockwood, J.-M. Baribeau, and T. I. Kamins, "Three-dimensional Silicon-Germanium Nanostructures for CMOS Compatible Light Emitters and Optical Interconnects," *Adv. Opt. Tech.,* vol. 2008, art. no. 218032, 2008.

[75] C. J. Glassbrenner and G. A. Slack, "Thermal Conductivity of Silicon and Germanium from 3°K to the Melting Point," *Phys. Rev.,* vol. 134, p. A1058, 1964.

[76] D. G. Cahill, M. Katiyar, and J. R. Abelson, "Thermal Conductivity of a-Si:H Thin Films," *Phys. Rev. B,* vol. 50, p. 6077, 1994.

[77] J. P. Dismukes, L. Ekstrom, E. F. Steigmeier, I. Kudman, and D. S. Beers, "Thermal and Electrical Properties of Heavily Doped Ge-Si Alloys up to 1300°K," *J. Appl. Phys.,* vol. 35, pp. 2899-2907, 1964.

[78] L. Shi, D. Li, C. Yu, W. Jang, D. Kim, Z. Yao, P. Kim, and A. Majumdar, "Measuring Thermal and Thermoelectric Properties of One-dimensional Nanostructures Using a Microfabricated Device," *J Heat Trans.,* vol. 125, pp. 881-888, 2003.

[79] D. G. Cahill, K. Goodson, and A. Majumdar, "Thermometry and Thermal Transport in Micro/nanoscale Solid-state Devices and Structures," *J Heat Trans.,* vol. 124, pp. 223-241, 2002.

[80] D. Li, Y. Wu, P. Kim, L. Shi, P. Yang, and A. Majumdar, "Thermal Conductivity of Individual Silicon Nanowires," *Appl. Phys. Lett.,* vol. 83, pp. 2934-2936, 2003.

[81] D. M. Rowe and V. S. Shukla, "The Effect of Phonon-grain Boundary Scattering on the Lattice Thermal Conductivity and Thermoelectric Conversion Efficiency of Heavily Doped Fine-grained, Hot-pressed Silicon Germanium Alloy," *J. Appl. Phys.,* vol. 52, pp. 7421-7426, 1981.

[82] N. Scoville, C. Bajgar, J. Rolfe, J. P. Fleurial, and J. Vandersande, "Thermal Conductivity Reduction in SiGe Alloys by the Addition of Nanophase Particles," *Nanostructured Materials,* vol. 5, pp. 207-223, 1995.

[83] W. L. Liu, T. Borca-Tasciuc, G. Chen, J. L. Liu, and K. L. Wang, "Anisotropic Thermal Conductivity of Ge Quantum-dot and Symmetrically Strained Si/Ge Superlattices," *Journal of Nanoscience and Nanotechnology,* vol. 1, pp. 39-42, 2001.

[84] X. Fan, G. Zeng, C. LaBounty, J. E. Bowers, E. Croke, C. C. Ahn, S. Huxtable, A. Majumdar, and A. Shakouri, "SiGeC/Si Superlattice Microcoolers," *Appl. Phys. Lett.,* vol. 78, pp. 1580-1582, 2001.

[85] T. Borca-Tasciuc, A. R. Kumar, and G. Chen, "Data Reduction in 3ω Method for Thin-film Thermal Conductivity Determination," *Rev. Sci. Inst.,* vol. 72, pp. 2139-2147, 2001.

[86] B. Yang, W. L. Liu, J. L. Liu, K. L. Wang, and G. Chen, "Measurements of Anisotropic Thermoelectric Properties in Superlattices," *Appl. Phys. Lett.,* vol. 81, p. 3588, 2002.

[87] S. Chakraborty, C. A. Kleint, A. Heinrich, C. M. Schneider, J. Schumann, M. Falke, and S. Teichert, "Thermal Conductivity in Strain Symmetrized Si/Ge Superlattices on Si(111)," *Appl. Phys. Lett.,* vol. 83, pp. 4184-4186, 2003.

[88] Y. Ezzahri, S. Grauby, S. Dilhaire, J.-M. Rampnoux, W. Claeys, Y. Zhang, and A. Shakouri, "Determination of Thermophysical Properties of Si/SiGe Superlattices with a Pump-Probe Technique," *2005 - International Workshop on Thermal Investigation of ICs and Systems,* pp. 235-243, 2006.

[89] J. Christofferson, K. Maize, Y. Ezzahri, J. Shabani, X. Wang, and A. Shakouri, "Microscale and Nanoscale Thermal Characterization Techniques," in *1st International Conference on Thermal Issues in Emerging Technologies, Theory and Applications; Proceedings - ThETA1*, 2007, pp. 3-9.

[90] Y. Ezzahri, S. Grauby, S. Dilhaire, J. M. Rampnoux, and W. Claeys, "Cross-plan Si/SiGe Superlattice Acoustic and Thermal Properties Measurement by Picosecond Ultrasonics," *J. Appl. Phys.,* vol. 101, art. no. 013705, 2007.

[91] A. Khitun, A. Balandin, J. L. Liu, and K. L. Wang, "In-plane Lattice Thermal Conductivity of a Quantum-dot Superlattice," *J. Appl. Phys.,* vol. 88, pp. 696-699, 2000.

[92] H.-Y. Chang, L. Tsybeskov, A. A. Sirenko, D. J. Lockwood, J.-M. Baribeau, X. Wu, and M. W. C. Dharma-Wardana, "Raman Measurements of Surface Temperature in Three- and Two-dimensional SiGe Nanostructures with a High Ge Concentration.," *Unpublished.*

[93] B. G. Streetman and S. Banerjee, *Solid State Electronic Devices*, 5 ed. Upper Saddle River, NJ: Prentice Hall, 2000.

[94] J. Weber and M. I. Alonso, "Near-band-gap Photoluminescence of Si-Ge Alloys," *Phys. Rev. B,* vol. 40, p. 5683, 1989.

[95] P. Yu and M. Cardona, *Fundamentals of Semiconductors Physics and Material Properties*, 3 ed. New York: Springer 2005.

[96] G. F. Grom, P. M. Fauchet, L. Tsybeskov, J. P. McCaffrey, H. J. Labbé, D. J. Lockwood, and B. E. White, "Raman Spectroscopy of Si Nanocrystals in Nanocrystalline Si Superlattices: Size, Shape and Crystallographic Orientation," *Mat. Res. Soc. Symp. Proc.,* vol. 638, pp. F6.1.1-F6.1.6, 2001.

[97] P. X. Zhang, D. J. Lockwood, H. J. Labb, and J. M. Baribeau, "Precise Measurements of the Gap Energy of Folded Acoustic Phonons in $Si/Si_{1-x}Ge_x$ Superlattices," *Phys. Rev. B,* vol. 46, p. 9881, 1992.

[98] D. J. Lockwood, M. W. C. Dharma-wardana, J. M. Baribeau, and D. C. Houghton, "Folded Acoustic Phonons in Si/Ge_xSi_{1-x} Strained-layer Superlattices," *Phys. Rev. B,* vol. 35, p. 2243, 1987.

[99] A. Mlayah and J. Groenen, *Resonant Raman Scattering by Acoustic Phonons in Quantum Dots* vol. 108. New York: Springer, 2007.

[100] M. Chandrasekhar, H. R. Chandrasekhar, M. Grimsditch, and M. Cardona, "Study of the Localized Vibrations of Boron in Heavily Doped Si," *Phys. Rev. B,* vol. 22, p. 4825, 1980.

[101] S. C. Jain, H. E. Maes, K. Pinardi, and I. De Wolf, "Stresses and Strains in Lattice-mismatched Stripes, Quantum Wires, Quantum Dots, and Substrates in Si Technology," *J. Appl. Phys.,* vol. 79, pp. 8145-8165, 1996.

[102] H. Okabe, *Photochemistry of Small Molecules*. New York: Wiley, 1978.

[103] L. Holz, A. Semjonow, K. Lenz, A. Lau, W. Richter, and H. Wilhelm, "Raman Spectroscopic Characterization of KrF-laser-irradiated Silicon," *J. Appl. Phys.,* vol. 72, pp. 2472-2477, 1992.

[104] M. F. Cerqueira and J. A. Ferreira, "Temperature Dependence of the First Order Raman Scattering in Thin Flms of μc-Si:H," *J. Mat. Proc. Tech.,* vol. 92-93, pp. 235-238, 1999.

[105] T. R. Hart, R. L. Aggarwal, and B. Lax, "Temperature Dependence of Raman Scattering in Silicon," *Phys. Rev. B,* vol. 1, p. 638, 1970.

[106] P. A. Temple and C. E. Hathaway, "Multiphonon Raman Spectrum of Silicon," *Phys. Rev. B,* vol. 7, p. 3685, 1973.

[107] M. I. Alonso and K. Winer, "Raman Spectra of $c\text{-}Si_{1-x}Ge_x$ Alloys," *Phys. Rev. B,* vol. 39, p. 10056, 1989.

[108] F. Cerdeira, A. Pinczuk, J. C. Bean, B. Batlogg, and B. A. Wilson, "Raman Scattering from Ge_xSi_{1-x}/Si Strained-layer Superlattices," *Appl. Phys. Lett.,* vol. 45, pp. 1138-1140, 1984.

[109] "HORIBA Jobin Yvon Spectrometers and Spectrographs Guide," 2007, http://www.analytical-online.com/Products/Analytical_instru/jobinyvonguide.html

[110] "Hamamatsu Product Datasheet: Photomultiplier Tube R943-02," 2003, http://sales.hamamatsu.com/assets/pdf/parts_R/R943-02.pdf

[111] "Ioffe Institute Semiconductor Database - n, k Database," 1998, http://www.ioffe.rssi.ru/SVA/NSM/nk/index.html

[112] H. R. Philipp and E. A. Taft, "Optical Constants of Germanium in the Region 1 to 10 eV," *Phys. Rev.*, vol. 113, p. 1002, 1959.

[113] D. Halliday, R. Resnick, and J. Walker, *Fundamentals of Physics*, 5th ed. New York: John Wiley and Sons, Inc., 1997.

[114] S. M. Lee and D. G. Cahill, "Heat Transport in Thin Dielectric Films," *J. Appl. Phys.*, vol. 81, pp. 2590-2595, 1997.

[115] N. Fukata, J. Chen, T. Sekiguchi, N. Okada, K. Murakami, T. Tsurui, and S. Ito, "Doping and Hydrogen Passivation of Boron in Silicon Nanowires Synthesized by Laser Ablation," *Appl. Phys. Lett.*, vol. 89, pp. 203109-3, 2006.

[116] N. Fukata, N. Okada, S. Matsushita, T. Tsurui, S. Ito, J. Chen, T. Sekiguchi, N. Uchida, and K. Murakami, "Carrier Doping of Silicon Nanowires Synthesized by Laser Ablation," *Mat. Res. Soc. Symp. Proc.*, vol. 963, pp. 0963-Q10-37, 2007.

[117] C. P. Herrero and M. Stutzmann, "Microscopic Structure of Boron-hydrogen Complexes in Crystalline Silicon," *Phys. Rev. B,* vol. 38, p. 12668, 1988.

[118] H. Tanino, A. Kuprin, H. Deai, and N. Koshida, "Raman Study of Free-standing Porous Silicon," *Phys. Rev. B,* vol. 53, p. 1937, 1996.

[119] P. J. Dean, J. R. Haynes, and W. F. Flood, "New Radiative Recombination Processes Involving Neutral Donors and Acceptors in Silicon and Germanium," *Phys. Rev.*, vol. 161, p. 711, 1967.

[120] T. Sekiguchi and K. Sumino, "Cathodoluminescence Study on Dislocations in Silicon," *J. Appl. Phys.*, vol. 79, pp. 3253-3260, 1996.

[121] L. Tsybeskov, E. K. Lee, H. Y. Chang, D. Lockwood, J. M. Baribeau, X. Wu, and T. Kamins, "Silicon-Germanium Nanostructures for On-chip Optical Interconnects," *Appl. Phys. A,* vol. 95, pp. 1015-1027, 2009.

[122] J.-M. Baribeau, X. Wu, and D. J. Lockwood, "Probing the Composition of Ge Dots and $Si/Si_{1-x}Ge_x$ Island Superlattices," *J. Vac. Sci. Technol. A,* vol. 24, pp. 663-667, 2006.

[123] M. W. C. Dharma-Wardana, A. H. MacDonald, D. J. Lockwood, J. M. Baribeau, and A. D. C. Houghton, "Raman Scattering in Fibonacci Superlattices," *Phys. Rev. Lett.*, vol. 58, pp. 1761-1764, 1987.

[124] J. L. Liu, G. Jin, Y. S. Tang, Y. H. Luo, K. L. Wang, and D. P. Yu, "Optical and Acoustic Phonon Modes in Self-organized Ge Quantum Dot Superlattices," *Appl. Phys. Lett.,* vol. 76, pp. 586-588, 2000.

[125] P. H. Tan, D. Bougeard, G. Abstreiter, and K. Brunner, "Raman Scattering of Folded Acoustic Phonons in Self-assembled Si/Ge Dot Superlattices," *Appl. Phys. Lett.,* vol. 84, pp. 2632-2634, 2004.

[126] G. F. Grom, D. J. Lockwood, J. P. McCaffrey, H. J. Labb, P. M. Fauchet, B. White Jr, J. Diener, D. Kovalev, F. Koch, and L. Tsybeskov, "Ordering and Self-organization in Nanocrystalline Silicon," *Nature,* vol. 407, pp. 358-361, 2000.

[127] A. Balandin, "Thermoelectric Applications of Low-Dimensional Structures with Acoustically Mismatched Boundaries," *Phys. Low-Dim. Struct. 5,* vol. 5/6, pp. 73-91, 2000.

[128] R. J. Nemanich, R. W. Fiordalice, and H. Jeon, "Raman Scattering Characterization of Titanium Silicide Formation," *IEEE Journal of Quantum Electronics,* vol. 25, pp. 997-1002, 1989.

[129] A. Šatka, J. Liday, R. Srnánek, A. Vincze, D. Donoval, J. Kováč, M. Veselý, and M. Michalka, "Characterisation of Titanium Disilicide Thin Films," *Microelectronics Journal,* vol. 37, pp. 1389-1395, 2006.

[130] H. Jeon, C. A. Sukow, J. W. Honeycutt, G. A. Rozgonyi, and R. J. Nemanich, "Morphology and Phase Stability of $TiSi_2$ on Si," *J. Appl. Phys.,* vol. 71, pp. 4269-4276, 1992.

[131] L. Tsybeskov, K. L. Moore, D. G. Hall, and P. M. Fauchet, "Intrinsic Band-edge Photoluminescence from Silicon Clusters at Room Temperature," *Phys. Rev. B,* vol. 54, p. R8361, 1996.

[132] E. Ertekin, P. A. Greaney, D. C. Chrzan, and T. D. Sands, "Equilibrium Limits of Coherency in Strained Nanowire Heterostructures," *J. Appl. Phys.,* vol. 97, pp. 114325-10, 2005.

[133] B. V. Kamenev, L. Tsybeskov, J. M. Baribeau, and D. J. Lockwood, "Photoluminescence and Raman Scattering in Three-dimensional $Si/Si_{1-x}Ge_x$ Nanostructures," *Appl. Phys. Lett.,* vol. 84, pp. 1293-1295, 2004.

[134] H.-Y. Chang, L. Tsybeskov, S. Sharma, T. I. Kamins, X. Wu, and D. J. Lockwood, "Photoluminescence and Raman Scattering in Axial Si/Ge Nanowire Heterojunctions," *Appl. Phys. Lett.,* vol. 95, art. no.: 133120, 2009.

[135] R. R. Reeber and K. Wang, "Thermal Expansion and Lattice Parameters of Group IV Semiconductors," *Materials Chemistry and Physics,* vol. 46, pp. 259-264, 1996.

[136] S. Nakashima, T. Mitani, M. Ninomiya, and K. Matsumoto, "Raman Investigation of Strain in Si/SiGe Heterostructures: Precise Determination of the Strain-shift Coefficient of Si Bands," *J. Appl. Phys.,* vol. 99, p. 053512, 2006.

[137] G. J. Snyder and E. S. Toberer, "Complex Thermoelectric Materials," *Nature Materials,* vol. 7, pp. 105-114, 2008.

[138] T. Borca-Tasciuc, W. Liu, J. Liu, K. L. Wang, and G. Chen, "Anisotropic Thermal Conductivity of a Si/Ge Quantum Dot Superlattice," *ASME Div. Heat Transfer,* vol. 366, pp. 381-384, 2000.

[139] G. Chen and A. Shakouri, "Heat transfer in Nanostructures for Solid-state Energy Conversion," *J Heat Trans.,* vol. 124, pp. 242-252, 2002.

[140] T. Tiedje, J. M. Cebulka, D. L. Morel, and B. Abeles, "Evidence for Exponential Band Tails in Amorphous Silicon Hydride," *Phys. Rev. Lett.,* vol. 46, pp. 1425-1428, 1981.

[141] R. A. Street, *Hydrogenated Amorphous Silicon*, illustrated ed.: Cambridge University Press, 1991.